Optimised high voltage spinels for Li-ion batteries

Optimised high voltage spinel for Li-ion batteries

Proefschrift

ter verkrijging van de graad van doctor
aan de Technische Universiteit Delft,
op gezag van de Rector Magnificus
Rector Magnificus, Prof. ir. K.C.A.M. Luyben,
voorzitter van het College voor Promoties,
in het openbaar te verdedigen op

donderdag 12 November 2015 om 10.00 uur

door
Raphael FREDON

Master of Materials for Energy Storage and Conversion

geboren te Poitiers, Frankrijk

Dit proefschrift is goedgekeurd door de

Promotor: Prof. Dr. E.H. Bruck

Copromotor: Dr. E.M.Kelder

Samenstelling promotiecommissie:

Rector Magnificus	Technische Universiteit Delft, voorzitter
Prof. Dr. E.H. Bruck	Technische Universiteit Delft, promotor
Dr. E.M. Kelder	Technische Universiteit Delft, copromotor

Onafhankelijke leden:

Prof. Dr. S.J. Picken	Technische Universiteit Delft
Prof. A. Chadwick	University of Kent
Prof. Dr. P.H.L Notten	Technische Universiteit Eindhoven
Prof. Dr. F.M Mulder	Technische Universiteit Delft

« Hé, Dame nature. Que vous en est nenni grâce à vos yeux. »

-Point. Point petit insecte subtil. La vie est comme l’onde. Fraîche et liquide comme l’ondée.

« Mais que vous en est nenni. Opterez vous pour un printemps gracieux et fraîche comme l’ondée ? »

-Point, petit insecte subtil. Viens picorer les mets de Dame nature.

« Grâce à vos yeux. »

Table of contents

Chapter 1: Introduction

Chapter 2: Review on LNMO

Chapter 3: In-situ X-Ray Absorption spectroscopy of Cr-doped and Cr-coated LNMO

Chapter 4: AFM/SECM Study

Chapter 5: Structural measurements (SEM, EDS, XRD, XAS, XPS)

Chapter 1 : Introduction

1.1 Introduction

Population growth and vast technological development result in huge energy consumption. Over the last twenty years, the global energy consumption increased by 52% and it is expected to increase further by 1.5 % per year until 2040 [1]. Fossil fuels, such as oil, coal and natural gas, account for 88% of the total worldwide energy consumption [1]. It takes nature a lot of time to produce those and human race is depleting the reserves at a much faster rate than what it takes to form them. The production and use of fossil fuels raise environmental problems: emission of carbon dioxide, nitrogen oxides, sulphur dioxide, volatile organic compounds and heavy metals. The increased greenhouse effect, acid rain and smog are some of the results. To support changes, we must promote the use of energy conversion and storage technologies, e.g batteries. Energy sources such as wind or solar energy, produce non continuous power that needs to be stored, in order to be used when the demand is higher. Regarding the transport system, we need to reduce the emission of carbon dioxide, for example by promoting the development of energy efficient vehicles, that are also less polluting. Several technologies are being developed and upgraded, such as hybrid vehicles, fuel cells vehicles, and of course, all-electric vehicles. Further focus on such a technology is however required, in order to implement batteries in their new applications and provide a low cost, safe and long lasting system.

1.2 Generalities

Batteries are electrochemical devices that convert chemical energy into electrical energy. The first battery, also referred to as ‘pila ', was invented in 1800 by the Italian physicist Alessandro Volta. Since then, a large variety of electrochemical cells with different features were developed. In every case, the different technologies share a similar principle: they exploit chemical reactions between different materials to store and deliver electrical energy. Batteries represent a particular sort of electrochemical cells. As it happens, an electrochemical cell is a system that will convert power into chemical energy and the other way around (i.e. chemical energy into electrical energy) by redox reactions. Electrochemical cells can be divided in two categories: *i) galvanic cells* and *ii) electrolytic cells.* A galvanic cell can directly produce electricity via spontaneous redox reactions. These cells are also known as ‘primary batteries' and constitute a source of energy which can be used to power electrical devices just as soon as discharged is not re-utilized (i.e. recharged). Conversely, electrolytic cells transform electrical energy into chemical energy via forced redox reactions, such as electrolysis. Electrolysis has various technological applications, like gas production (i.e. H_2, Cl_2, etc.) and metal plating (i.e. electrodeposition). The electrolytic process is further exploited in the so-called ‘secondary batteries ', also known as rechargeable batteries, which can store and convert reversibly electrical and chemical energy, depending on both galvanic and electrolytic processes. For example, a rechargeable battery works as being an electrolytic cell during its charge and like a galvanic cell upon discharge. Hence in secondary batteries, their underlying chemical reaction is reversible. In this way they restore their charge by reversing the direction of the current flow that developed during discharging. Consequently, they might be re-used easily many times. Four types of rechargeable batteries currently dominate the market, each of which possesses its own pros and cons with regards to practical issues like application, durability, cost, safety and performance.

The four systems are :

- Lead-acid (Pb-acid) batteries
- Nickel-Cadmium (Ni-Cd) batteries
- Nickel-metal-hydride (Ni-MH) batteries
- Lithium-ion (Li-ion) batteries

The first rechargeable battery, the lead-acid battery was invented in 1859 by the French physicist Gaston Planté. Nowadays lead-acid batteries hold about 50 % of the worldwide rechargeable-battery market. They are certainly cost-effective power sources which might be found in pretty much all cars and are also employed in large back-up systems. Yet, they won't store much energy for a given weight or volume, as compared to newer technologies. Nickel-Cadmium batteries were first introduced in 1899 by Waldemar Jungner from Sweden. These systems were adopted to applications where more power was needed. After the 1960s, Ni-Cd batteries become popular power sources for portable electronics, electric shavers, toys and, more generally speaking, for devices where large operating currents are required. Ni-metal-hydride batteries appeared in the marketplace in 1989 as being an evolution on the 1970s' Nickel-hydrogen batteries, which were only employed in space applications (e.g. in satellites). Ni-MH technology was finally established by an American inventor, Stanford Ovshinsky, who created suitable metal-hydride alloys with disordered structures and specific compositions to satisfy the commercial requirements. Nevertheless, their early prototypes were actually manufactured by Percheron and van Vecht, in France and the Netherlands respectively. Ni-MH technology represents the initial quantum leap in terms of energy stored per unit weight, with figures doubling the ones from lead-acid batteries. In the ‘90s, Ni-MH batteries became the favourite option for powering portable electronics, displacing Ni-Cd technology in several applications, as well as providing a source of energy for hybrid-electric vehicles (HEV). Li-ion batteries started out as primary (i.e. non-rechargeable) lithium batteries in the ‘70s, mainly for low-current applications, like watches, hearing aids and pace-makers. Electrochemical reactions involving lithium became more and more attractive, because Li is the lightest solid element on earth ($Mm = 6.941\ gmol^{-1}$; $\rho = 0.534\ gcm^{-3}$) and it is essentially the most reducing metal in nature ($E° = -3.04\ V$), making it an excellent candidate for batteries with an increased energy density. The first lithium batteries typically employed metallic Li in combination with MnO_2, along with a non-aqueous electrolyte. In 1975 other pioneering studies by Whittingham were performed on rechargeable lithium batteries [2], where metallic lithium as negative electrode was placed against layered $LixTiS_2$ as the positive electrode and using a non-aqueous electrolyte. The critical issue these batteries concerned is their stability. Repeated charge and discharge resulted in the formation of dendrites of lithium, which caused shorts through the separator. This intrinsic drawback, along with the reactivity of metallic lithium posed severe limitations to widespread and safe use of these cells. The potential risk of explosions and bursting into flames, accompanied by release of toxic fumes, was too high for these batteries to penetrate the market. The final breakthrough in Li technology happened in the ‘80s. The metallic lithium was replaced by intercalation compounds containing lithium [3-6], such as graphite [7], and more in general carbonaceous materials [8, 9], these were found to accept and electrochemically release Li in a reversible fashion. These systems then became well known as “Li-ion batteries”, as the lithium was merely found in its ionic form. The first commercial Li-ion battery was released by Sony in 1991. It was made of layered lithium cobalt oxide as the positive electrode, graphite as the negative electrode and a polymer electrolyte. In the following years several improvements were introduced in the technology particularly in the materials, hence Li-ion started dominating the market of power sources for portable electronics. Obviously, the actual reason for the widespread introduction and implementation of Li-ion batteries is the increased capacity and energy density, as shown in Fig. 1.1, which compares the various rechargeable battery technologies in the case of gravimetric and volumetric energy densities.

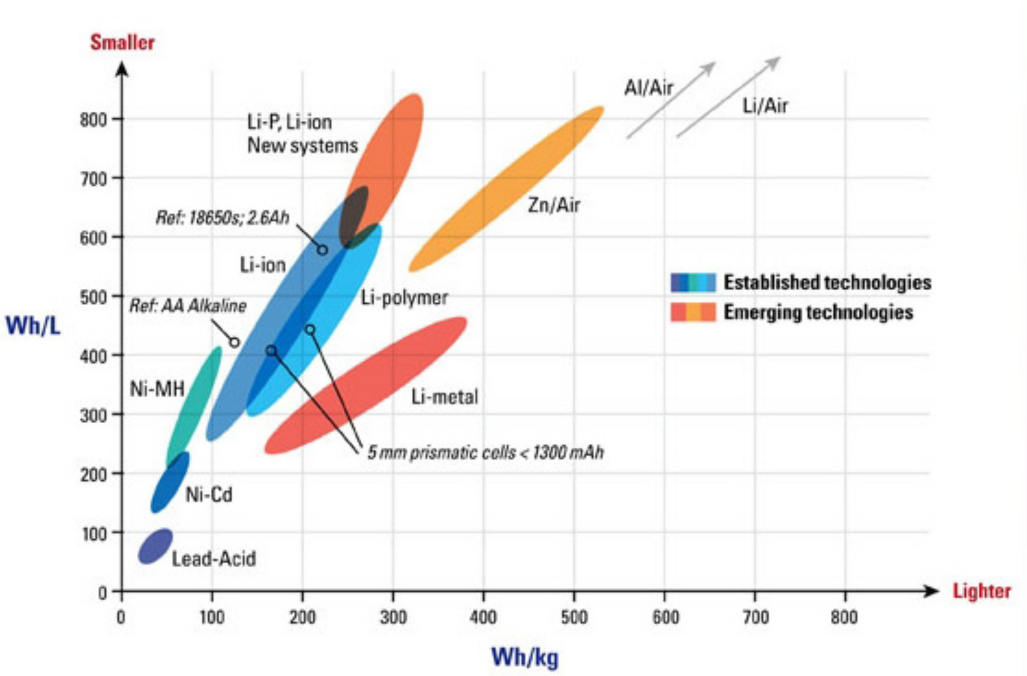

Fig. 1.1. *Battery scenario comparing different technologies for rechargeable cells in terms of volumetric and gravimetric energy densities.*

Li-ion batteries outperform the other technologies, providing scaled-down and lighter power sources. Another important feature that contributed to their widespread use is that, unlike other rechargeable cells, they don't have any memory effect (i.e. losing capacity when a battery is recharged before it was fully discharged. These factors then made the mobile-phone revolution possible. However, Li-ion batteries now need to face the main ‘mobility challenge :

powering electric vehicles (EV)'. Electrification of cars is soon expected, especially considering the world global climate change together with the shortage found on earth oil reserves. When thinking of this, the prospects of the current Li-ion battery technologies doesn't match the final requirements. Indeed, as shown in Fig. 1.2 Li-ion batteries are still sometimes quite far from the needs for EVs. However, Li-ion batteries take over more and more the use of NiMH batteries in the last years, which is reflected by the introduction of the new efficient EVs, such as Tesla, Nissan Leaf, etc. Unfortunately we cannot expect a similar growth in energy density as found for the evolution of semiconductors following Moore's law.

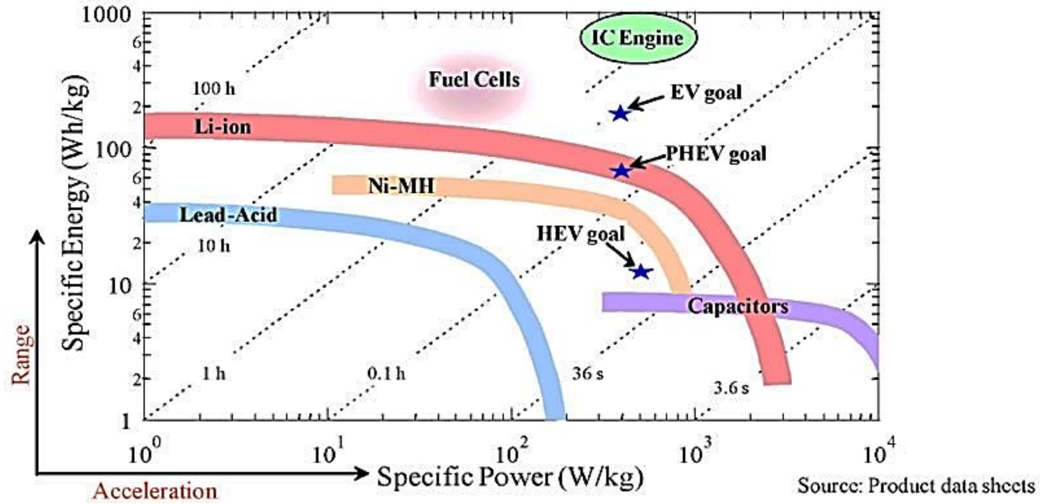

Fig. 1.2. Ragone plot comparing different types of rechargeable batteries, but also plug-in hybrid vehicles (PHEV) and internal combustion (IC) engine. The two bubbles refer to the requirements needed for powering electric vehicles (EV) and hybrid electric vehicles (HEV), respectively. Note also that the various time intervals, in which the energy is being delivered, are indicated by the dotted lines.

1.3 Basic principles of a rechargeable (li-ion) battery

A Li-ion battery is composed of three main parts. A positive electrode, a negative electrode, which are kept separated by a separator soaked in an ionic conductive electrolyte that will serve as a bridge for the lithium ions between the two electrodes, blocking the electrons. The electrolyte can possess 3 main types : a solid-state compound, an ion-conductive polymer or a non-aqueous liquid. During the discharge of the battery, positively charged ions travel from the negative to the positive electrode while an equal number of electrons go the opposite way through an external circuit, producing a current that will be used. In Fig 1.3, the charging and discharging of a battery is shown. Recharging a (Li-ion) battery involves external work which forces the electrochemical reaction to occur in the opposite direction and this is achieved by reversing the direction of the current flow through the external circuit.

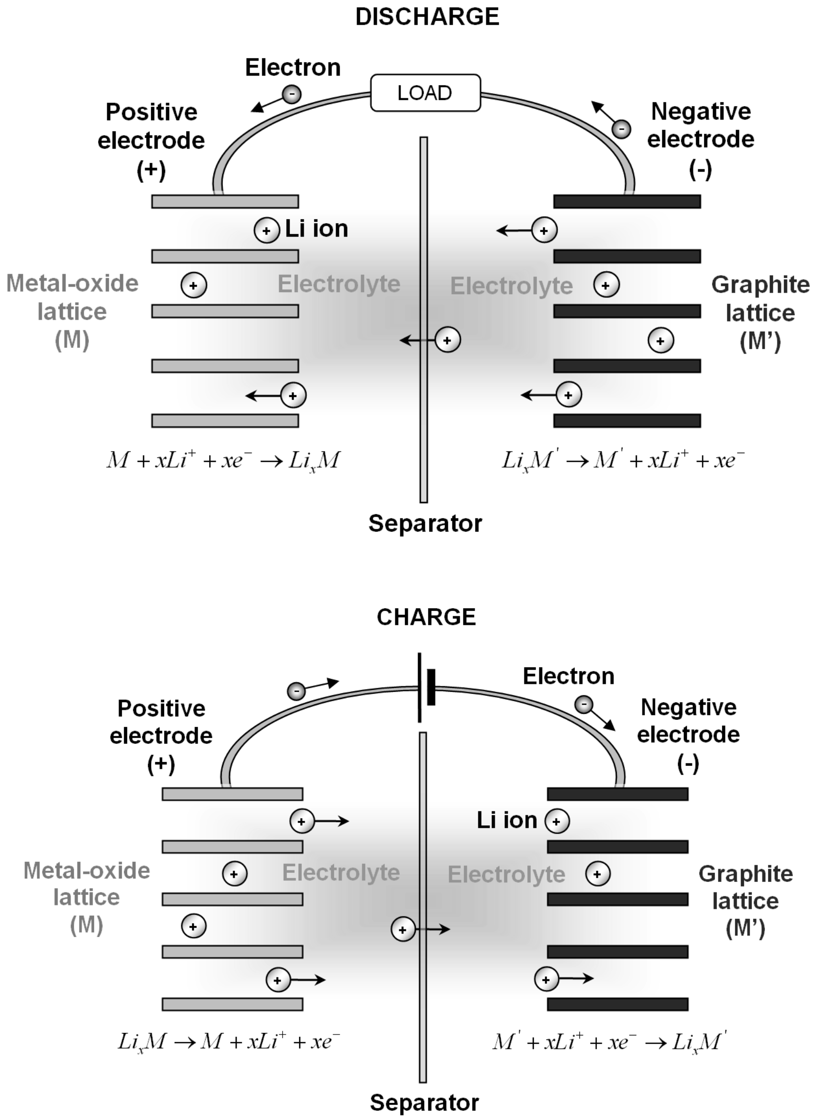

Fig. 1.3. Schematic drawing of the working principle of a Li-ion battery. M and M' represent the active materials. In a charged Li-ion battery the graphite lattice is packed with Li ions in a high-energy state. Connecting a load causes its discharge, with Li ions transferred through the electrolyte and taking up residence in the metal-oxide lattice, while releasing energy in the process. Note that for each Li ion an electron must make the same journey through the external circuit, producing a current. Recharging the battery requires a forced reaction, by which the electrons are pushed in the opposite direction through the circuit and the lithium ions are driven back through the electrolyte into the graphite lattice.

1.4 Scope of the thesis – EuroLiion project

The research described in this thesis is a part of the EuroLiion project (http://www.euroliion.eu). It aims to develop a new Li-ion cell for traction purposes with the following characteristics: 'High energy density of at least 200 Wh/kg 'Low costs i. e. , a maximum of 150 Euro/kWh 'Improved safety Although the Li-ion cell appears to be the most appropriate technology to meet these goals, considerable research and development is required. For example, the much-used $LiFePO_4$ cells cannot reach the energy density criterion, and in addition, $LiFePO_4$ is patented, which hampers worldwide commercialisation. Many other materials are either too expensive or do not meet current safety, environmental standards (e. g. , cobalt in $LiCoO_2$). Thus, we propose a shift from carbon to the much higher capacity silicon-based anodes, and from cobalt-based to iron and/or manganese/nickel-based positive electrodes, and to use novel electrolyte salts.
To successfully develop a European Li-ion technology, the R&D started at the anode side, i. e. Si, with a $LiFePO_4$-C material at the positive electrode side. This requires a new electrode formulation with respect to binder, electrolyte salt, solvent, and composition. The change in formulation at the anode and electrolyte allows for a change in the positive electrode materials and a series of both novel (e. g. , fluorosulfates, $LiFeSO_4F$) and more established systems, were investigated. New synthetic routes are employed, along with an extensive characterization program. Scale-up, testing and benchmarking of optimum formulations were performed. The outcome is a newly developed cell, manufactured and tested by end-users. The new cell consists of i) a newly formulated Si-negative electrode, ii) newly designed low cost salts, and iii) Modified LNMO positive electrodes. To achieve these goals, the consortium included renowned universities and knowledge institutes, a battery producer, and the car industry as end-users. Thus, the composition of the consortium covers the whole spectrum of R&D, manufacturing and testing, e.g Renault, GAIA gmbh, Austrian Institute of Technology, Spijkstaal Elektro BV, Volvo Technology AB, Uppsala Universiteit, CNRS, ZSW,University of Cambridge, Kemijski Institut, CEA.
The work described in this thesis involved the synthesis, testing, characterisation and optimisation of the positive electrode material based on $LiNi_{0.5}Mn_{1.5}O_4$. In the second chapter, a review of the work that has been done regarding LNMO will be presented. Then, in chapter 3, a description of the research on the chosen (chromium) doping/coating element is shown. Chapter 4 describes the progress made in order to try to characterize and monitor the ionic and electronic conductivity at the interface between the electrolyte and the positive electrode. An accurate characterization of the surface of the electrode will be presented in Chapter 5.
Finally, the last chapter of this thesis will be composed of a summary of this work, as well as the EuroLiion project and a summary of the work done to make it successful.

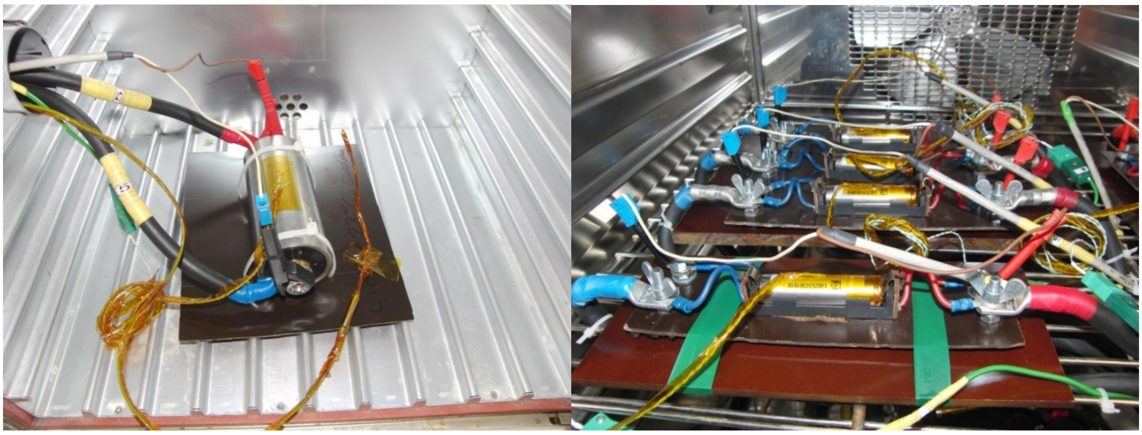

References

1. BP. *BP Statistical Review of world Energy 2014*. 2015; Available from: http://www.bp.com/content/dam/bp/pdf/Energy-economics/statistical-review-2014/BP-statistical-review-of-world-energy-2014-full-report.pdf.
2. Whittingham, M.S. and F.R. Gamble, *Lithium Intercalates of Transition-Metal Dichalcogenides.* Materials Research Bulletin, 1975. **10**(5): p. 363-371.
3. Thackeray, M.M., et al., *Lithium Insertion into Manganese Spinels.* Materials Research Bulletin, 1983. **18**(4): p. 461-472.
4. Thackeray, M.M., et al., *Electrochemical Extraction of Lithium from Limn2o4.* Materials Research Bulletin, 1984. **19**(2): p. 179-187.
5. Thackeray, M.M., W.I.F. David, and J.B. Goodenough, *Structural Characterization of the Lithiated Iron-Oxides Lixfe3o4 and Lixfe2o3 (0-Less-Than-X-Less-Than-2).* Materials Research Bulletin, 1982. **17**(6): p. 785-793.
6. Thomas, M.G.S.R., P.G. Bruce, and J.B. Goodenough, *Lithium Mobility in the Layered Oxide Li1-Xcoo2.* Solid State Ionics, 1985. **17**(1): p. 13-19.
7. Yazami, R. and P. Touzain, *A Reversible Graphite Lithium Negative Electrode for Electrochemical Generators.* Journal of Power Sources, 1983. **9**(3-4): p. 365-371.
8. Kanno, R., et al., *Carbon as Negative Electrodes in Lithium Secondary Cells.* Journal of Power Sources, 1989. **26**(3-4): p. 535-543.
9. Mohri, M., et al., *Rechargeable Lithium Battery Based on Pyrolytic Carbon as a Negative Electrode.* Journal of Power Sources, 1989. **26**(3-4): p. 545-551.

Chapter 2 : Review on $LiNi_{0.5}Mn_{1.5}O_4$

2.1 Introduction

Spinel-type lithium manganese oxide ($LiMn_2O_4$) as a positive electrode material for lithium-ion batteries has been paid much attention due to its low cost, low toxicity, and relatively high energy density [1-3]. However, $LiMn_2O_4$ in the 4-V region suffers from a poor cycling behaviour [4]. It is well known that the electrochemical performance of $LiMn_2O_4$ can be improved by doping. This property opened the way for new perspectives for lithium batteries, such as an increase in energy density with respect to $LiCoO_2$ and other “4V” materials, and the possibility to use negative electrodes working significantly above 0V. The high-voltage plateau is mainly present in spinels where the B-site (often conventionally indicated by square brackets) contains a combination of Mn and another transition metal M, as in formula $Li\{M_xMn_{2-x}\}O_4$ (M= Cr, Fe, Co, Ni, Cu), where x is close to the maximum value x = 0.5 [5, 6]. Among them, LNMO has been extensively studied as a positive electrode material for lithium ion batteries during the past decade on account of their improved cycling behaviour relative to the undoped spinel . K. Amine et al. [7, 8] first reported LNMO prepared with a low-temperature sol–gel method, which can be operated at a 4.7 V plateau in contrast to the 4.1 V plateau of $LiMn_2O_4$. This high operating potential and three dimensional lithium-ion diffusion paths in the spinel lattice has led to even more attentions. Lithium ion batteries with $LiNi_{0.5}Mn_{1.5}O_4$-based positive electrodes are expected to provide high power/energy density for electric vehicles (EVs), hybrid electric vehicles (HEVs) and large energy storage systems. LNMO is a FCC lattice that has two different space groups : $P4_332$ and Fd-3m, depending on the oxygen content in the lattice and/or the degree of ordering of the Ni/Mn ions [9, 10], as seen in Fig 2.1.

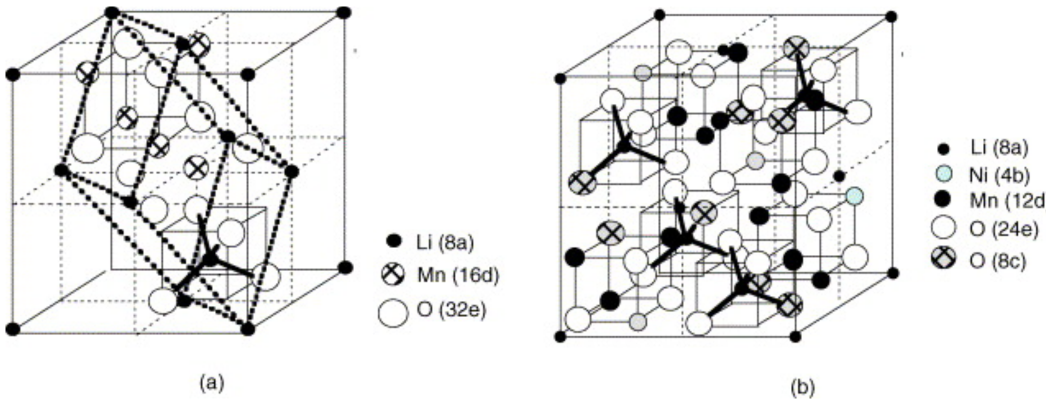

Fig.2.1. Crystal structure of LNMO with Fd-3m space group (left), and crystal structure of LNMO with $P4_332$ space group (right) [11].

Besides the 4.7V plateau, the spinel is also able to accept lithium ions at the 3V plateau similar as the $LiMn_2O_4$ spinel. This part will however not be used in the current systems, and will only briefly addressed at the electrochemical part. According to Ariyoshi et al [9], the LNMO with the Fd-3m structure exhibits better electrochemical performances than that with the $P4_332$ structure. On the other hand, it is difficult to synthesize a pure stoichiometric LNMO because an impurity phase $Li_yNi_{1-y}O$ tends to be formed during the high temperature synthesis [12, 13]. Besides, the fast capacity fading of a LNMO electrode at elevated temperatures is another disadvantage of this material for applications [14, 15]. To improve the electrochemical performance, various modification methods such as lattice doping and surface coating have been adopted. Partial substitutions of Mn and (or) Ni in LNMO with other cations have been investigated. In this chapter, an overview has been given on the recent developments of LNMO. Since the performance of the material is one of the main issue of this review, the chapter is structured so as to discuss the key parameters that are involved, these are:

Structural aspects

-Electrochemistry aspects:

-Modification of LNMO :

-Cation doping

-Anion doping

· Morphology

· Interfaces/interphases

-Coatings

In the following work $LiNi_{0.5}Mn_{1.5}O_4$ will be referred to as LNMO.

2.2 Structural aspects

2.2.2 Crystallographic aspects

As mentioned earlier, LNMO has two different space groups of $P4_332$ and Fd-3m, depending on the oxygen content in the lattice and/or the degree of ordering of the Ni/Mn ions [9, 10, 16]. A high-temperature (>700 °C) synthesis usually leads to produce a LNMO powder with the Fd-3m structure. In this structure, Ni and Mn ions are randomly distributed in the octahedral (16d) sites, Li+ ions occupy the tetrahedral (8a) sites, while some of the oxygen, residing on the 32e sites, may be released from its lattice structure, thereby reducing a small amount of Mn^{4+} to Mn^{3+} in order to balance the charge. An annealing of the spinel powder at 700 °C in air can transform its crystal structure from Fd-3m to $P4_332$, in which the Ni and Mn ions occupy orderly on the 4b and 12d sites, respectively. The oxygen ions are in the 8c and 24e sites. It is stressed that LNMO powder has been indexed by the cubic $P4_332$ symmetry due to the appearances of the weak peaks located at 2Θ = 15.30, 39.70, 45.70, and 57.50, while these peaks are absent from the pattern of Fd-3m structure. Typically, a weak peak attributed to the impurity NiO or LiyNi1-yO is observed in the patterns of LNMO. It has been found that the cationic substitutions can eliminate the formation of the LiyNi1-yO impurity phase and stabilize the spinel structure with a disordering of the Mn^{4+} and Ni^{2+} ions in the 16d octahedral sites. Such a cationic doping also results in a smaller difference in lattice parameter among the three cubic phases formed during the cycling process so that the cycle life is prolonged. Although the space difference is difficult to determine with XRD technique owing to a similar scattering behaviour of Ni and Mn, small differences can be assigned (Fig 2.1) [17]. Similarly, these differences can be found in neutron diffraction spectra (Fig 2.2). Fournier transform infrared (FT-IR) spectroscopy has been proved to be an effective technique in qualitatively resolving the cation ordering [18, 19]. A disordered structure of space group of Fd-3m showed two bands at about 619 cm^{-1} which are more intensive than those at 588 cm−1. A band occurs at 650 cm^{-1} for $P4_332$ phase in the FT-IR spectrum

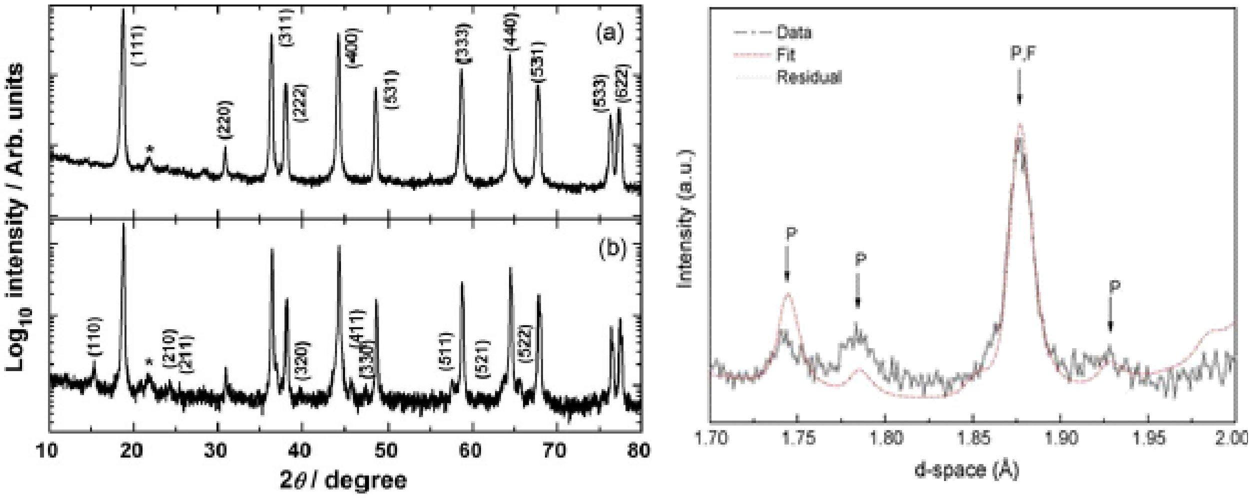

Fig. 2.2. Left: X-ray diffraction patterns of $LiNi_{0.5}Mn_{1.5}O_{4-d}$ having two different crystallographic structures: (a) face-centered spinel (Fd-3m) and (b) primitive simple cubic ($P4_332$)[20]. Right: Neutron diffraction of $LiMg_{0.05}Ni_{0.45}Mn_{1.5}O_4$. The reflections belonging to the $P4_332$ and Fd-3m space groups are labelled as P and F, respectively

Similarly, Raman spectroscopy is adopted to distinguish the $P4_332$ from the Fd-3m space group (Fig 2.3). According to Oh et al.[21] and Julien and coworkers [22], the strong band around 635 cm^{-1} is assigned to the symmetric Mn–O stretching mode of MnO_6 octahedra (A1g). Both peaks around 402 and 491 cm^{-1} are associated with the Ni^{2+}–O stretching mode in the structure, and the peak near 580–606 cm^{-1} is considered as T_{2g} (3) of the spinel compound. In addition, the peak splitting between the bands at 606 and 589 cm^{-1} is clearly observed for LNMO, while only a broad hump is observed for the doped samples. Also, the bands around 400, 239, 218 and 160 cm^{-1} are much stronger for the LNMO than for the doped samples. Note that the splitting of T_{2g} (3) band is often considered as the obvious evidence of the ordered structure ($P4_332$) of the spinel. Meanwhile, the strong bands around 400, 239, 218 and 161 cm^{-1} are also the features of $P4_332$ structure.

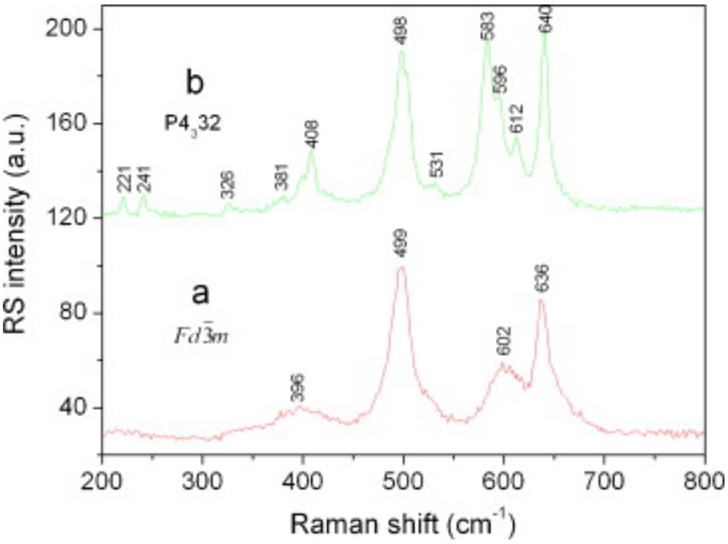

Fig.2.3. Raman spectra of the LNMO samples prepared by two-step (a) and one-step (b) solid-state reactions [23]

Studies indicated that rapid cooling of LNMO spinel after a heat treatment at the high temperature would tend to preserve some amount of Mn^{3+} left in the compound, created due to the insufficient oxygen take-up by Mn^{3+} [12, 24]. In addition, previous studies by other workers indicated that the rapid cooling of LNMO spinel after a heat treatment at the high temperature would tend to preserve some amount of Mn^{3+} left in the compound, created due to the insufficient oxygen take-up by Mn^{3+} [12, 24]. Besides, it has been reported that the generation of Mn^{3+} in LNMO is inevitably related with $Li_zNi_{1-z}O$ impurity phase [25], and which is regarded harmful in the light of structural stability due to the Jahn–Teller distortion of Mn^{3+}. On the other hand, when the cooling rate after the calcination from the high temperature is slow or when the compound is exposed to an annealing process, Mn^{3+} cations in the compound can be reportedly reversibly transformed into Mn^{4+} cations without any impurity phase formation because the following disproportionation reaction is considered plausible in a certain critical temperature range [23, 26]:

$$LNMO(@\ low T) \leftrightarrow a\ Li_zNi_{1-z}O + b\ LiNi_{0.5-d}Mn_{1.5}+dO_4 + c\ O_2\ (@\ high\ T)$$

This loss of oxygen can be measured via thermogravimetric analysis as shown in [21].

Several reports infer that the critical temperature range for the elimination of Mn^{3+} is about 600–650 °C [23, 26], i.e. LNMO samples calcined at 600 °C for 8 h, and annealed at 650 °C, are regarded to contain less Mn^{3+}, while quenching leaves a non-negligible amount of Mn^{3+} and thereby the corresponding 4V electrochemical capacity. However, currently, the change in the phases has been reported to occur at higher temperatures (800–900 °C) [21]. In a more recent paper [27] the temperature was found to be at 730 °C.

Only a few papers report on the existence of a lithium excess in the structure [28] eventually with oxygen vacancies. Also, very recently, Cabana et al [29] showed that the second phase often referred to as LixNi1-xO with the rock salt structure also contains manganese, and that oxygen vacancies do not exist. This was characterized in-depth of samples formally formulated as LNMO and revealed the subtle crystal-chemical intricacies of this compound. Under the conditions chosen for the synthesis, the spinel samples systematically showed deviations from the theoretical stoichiometry, which involved an excess of Mn. The Mn excess resulted in the formation of some Mn^{3+} and was compensated (or driven) by the formation of a secondary phase with a rock-salt structure, not by the creation of oxygen vacancies. For the first time, it was reported that this rock-salt phase contains both Mn and Ni in a lower ratio than in the spinel phase (ca. 2 to 1 vs 3 to 1). Its formation occurs through the preferential extrusion of Ni out of the spinel particles, its content in the sample being correlated with the amount of Mn over-stoichiometry in the spinel phase. Detailed insight into the ordering schemes possible in “LNMO” was also provided. It was shown that samples showing superstructure reflections do not necessarily have perfect Ni and Mn ordering in a $P4_332$ superlattice. Local deviations from the ideal picture, as well as different disordered schemes, are possible. Indeed, some samples were shown to have some degree of preference for certain Ni/Mn distributions even if they crystallized in a disordered framework. The off-stoichiometry in 700 °C, a sample crystallizing in a $P4_332$ unit cell, demonstrated that the presence of Mn^{3+} in the spinel structure does not completely preclude Ni/Mn ordering. Generally speaking, this work highlights the importance of careful characterization of “LNMO” samples if the goal is to establish composition− structure−properties correlations. Electrode testing confirmed that composition and structure affect the response of the material. However, although worse cycling performance was obtained for the most ordered sample, no difference in the position of the high voltage plateaus was found between samples with different Ni/Mn arrangements. Given the notable entanglement between and crystal-chemical parameters, more work is needed to completely correlate them to electrochemical properties. However, the detailed picture obtained from this study provides a necessary initial underpinning to the task of achieving control of these parameters through the synthesis conditions. Such control is required to design LNMO electrodes that are closer to the performance limit that the material can offer.

2.2.3 Electronic structure

Theoretical calculations computational studies based on DFT methods are performed to give quantitative understanding of the electronic properties and structural stability for spinels [30]. The calculated results of lattice constant for spinel phase and Mn(Ni)–O average bond length is well consistent with the experiment results. The shortening of Mn(Ni)–O bond strengthens the structural stability of spinel. The LDOS calculations show that the bonding between O and metal is also strengthened due to the Ni doping, and then it improves the structural stability of LNMO. The filling of electrons in the metal orbitals affects the LDOS of all elements, but the bonding way of the system is not changed. The formation enthalpies and overlap populations of Mn–O in both spinels indicate that Ni doping greatly improves the structural stability of spinel.

Voltage profile calculations via first-principles calculations

A model has developed to unravel the intricate cationic ordering in LNMO by combining first principles calculations with the cluster expansion method. The findings explain the different features in the voltage profile for $P4_332$ as compared to Fd-3m as a result of coupled Ni/Mn and Li/VA orderings. It has been quantitatively demonstrated that there exist incommensurateness between the preferred Li/VA configuration and the Ni/Mn configuration in $P4_332$, which explains the observed negligible voltage step at x ¼ 0.5 in $P4_332$ compared with Fd-3m. Furthermore, the predicted formation energy and the voltage as a function of Li content show that perfectly ordered $P4_332$ exhibits only one two-phase region in entire range of $0<x<1$, while uniformly disordered Fd-3m exhibits two pronounced two-phase regions of $0<x<0.5$ and $0.5<x<1$ with the possibility of more ground states at high lithiation depending on the existence of local deviations from the overall Ni/Mn ordering. In conclusion, we have studied the influence of cation order on the Li/VA configuration and resulting phase transformations during Li intercalation which provides the necessary relationship between the materials chemistry and its performance and in turn, enables rational design of the electrode material. The results are summarized in Fig.4 .

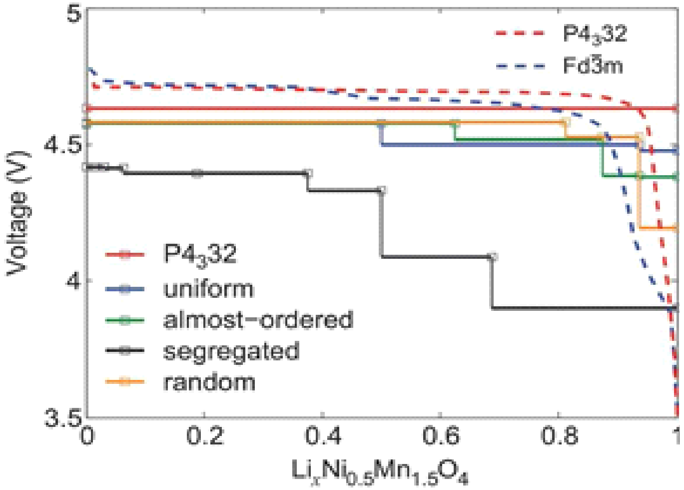

Fig.2.4. Voltage as a function of Li content x. Dashed lines are experimental observations reproduced from [31].

2.3 Electrochemical aspects

LNMO can donate as well as accept lithium ions (see Fig 2.4). Donation typically occurs at voltages above 3.5V, whereas accepting lithium ions occurs at voltages below 3.5V. Although the low voltage plateaus contribute significantly to the overall capacity, only the high voltage part is typically utilized in the current systems. It is therefore, that we will mainly concentrate on that part. Nevertheless, the low voltage part is briefly addressed below [17, 20, 32]. Two plateaus at ~2.7 and ~2.1 V during discharge and at ~2.9 and ~3.82 V during charge appear when lithium ions are reversibly inserted/extracted into/from the 16c octahedral sites. From structural studies, it is understood that the larger empty octahedral sites available in the cation-ordered spinel phase explain why longer ~2.7 V plateau during discharge and ~2.9 V plateau during charge are displayed by the more ordered spinel. Ex situ XRD analysis confirms that the evolution of two tetragonal phases (T1 and T2) is linked with the two distinct ~2.7 and ~2.1 V plateaus corresponding to the insertion of lithium ions into the 16c octahedral sites [20, 25]. The evolution of the first tetragonal phase (T1) is attributed to the

Jahn−Teller distortion of Mn^{3+} ions. The evolution of the second tetragonal phase (T2) originates from the additional lattice distortion caused by the insertion of larger lithium ions into smaller 16c octahedral sites in the disordered phase. The gradual increase in OCV from 2.0 to 2.8 V over time when the load is removed is attributed to the spontaneous transformation of the unstable T2 phase to the T1 phase [25]

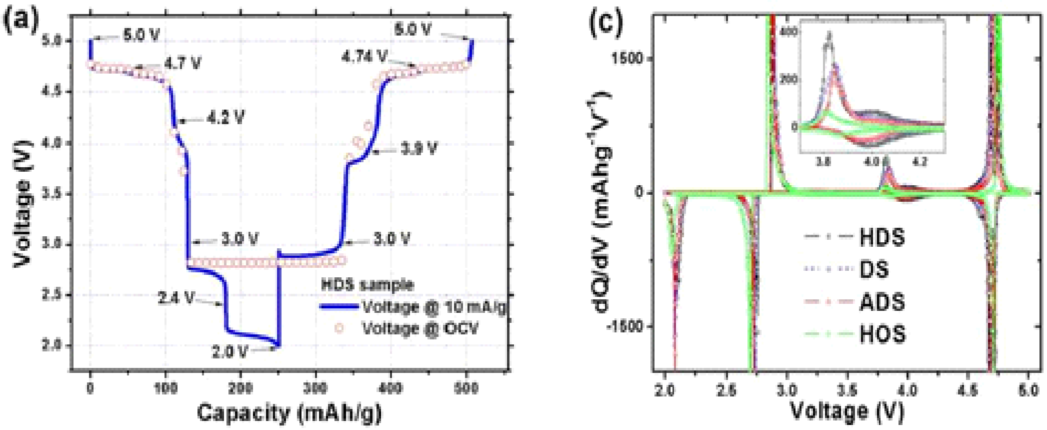

Fig.2.5. (a) OCVs with a constant current voltage profile as a function of cumulative capacity. (c) differential capacity (dQ/dV) plots of the four LNMO samples when cycled between 5 and 2 V at 10 mA/g [32]

During the charging/discharging processes, LNMO demonstrates two plateaus at around 4.7 V, corresponding to the redox reactions of Ni^{2+}/Ni^{3+} and Ni^{3+}/Ni4+ couples. Kim et al. [10] studied the phase transition of LNMO during Li^{+} extraction by measuring the ex situ XRD patterns. They have found that the LNMO with a space group of Fd-3m undergoes a topotactic two-phase transition during electrochemical cycling, while the LNMO with a space group of P4$_3$32 shows topotactic phase transitions among three different cubic phases. Recently, Wang et al. [33] studied the phase evolution during Li insertion/extraction process using in situ XRD. They have observed three cubic phases for the LNMO samples with either P4$_3$32 or Fd-3m structure. For the LNMO with a Fd-3m structure, an additional 4.0 V plateau may be observed that is corresponding to the Mn^{3+}/Mn^{4+} redox couple (Fig 2.6). According to Ariyoshi et al. [9], the LNMO with the Fd-3m structure exhibits better electrochemical performances than that with the P4$_3$32 structure [34, 35]. Furthermore, it is stressed that Mn is electrochemically inactive and stays mainly in its 4+ state, therefore it is assumed that the electrochemical inactivity of manganese could be a factor of stability of the structure on cycling [36].

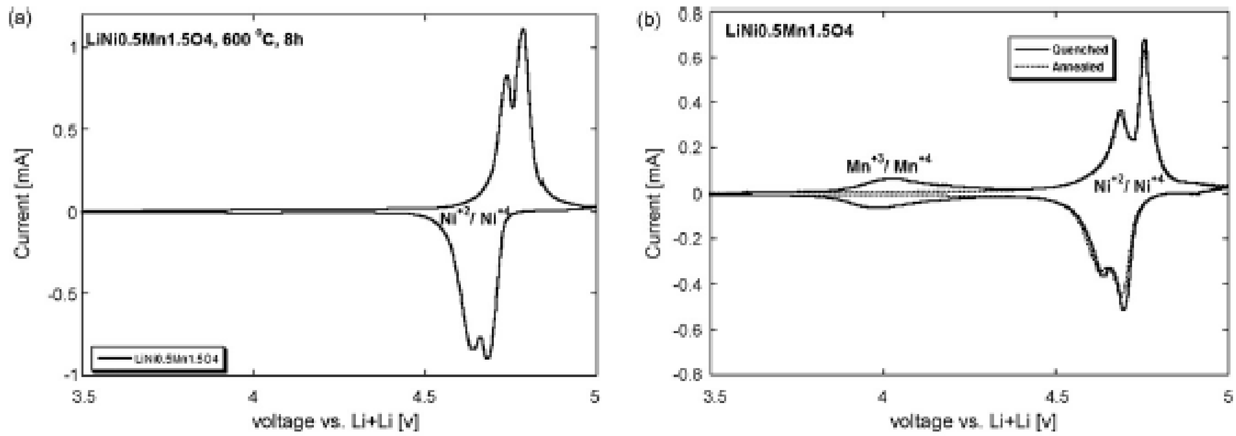

Fig.2.6: Cyclic voltammograms of LNMO with the $P4_332$ (a) and Fd-3m (b) space group [21].

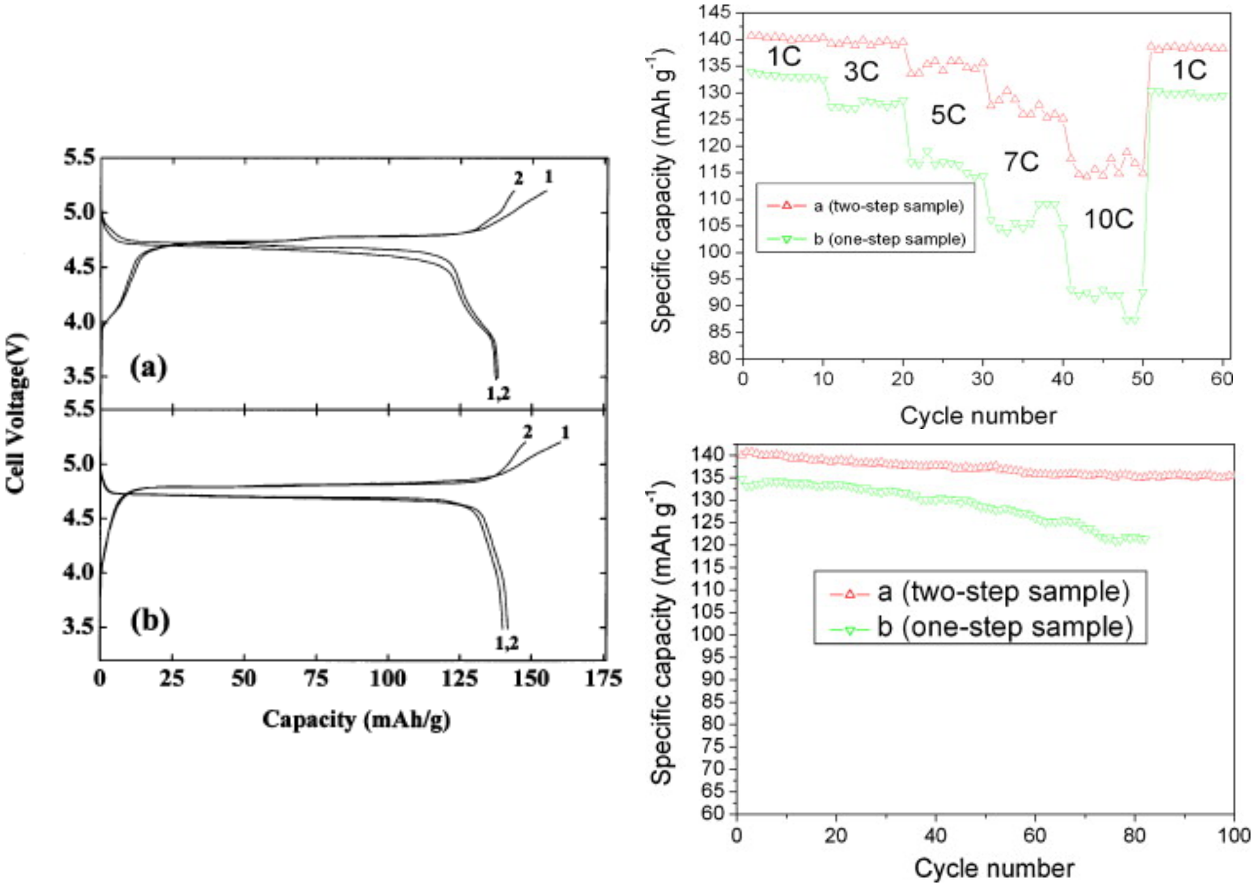

Fig.2.7. Left: The charge/discharge curves for the Li/1 M LiPF6-EC/DMC/LNMO obtained by the (a)sol–gel method 750°C, and (b) composite carbonate process at 700°C, with a current density of 0.4mA/cm2 between 5.2 and 3.5 V at room temperature [37]. Right: Cycling and rate performance ofLNMO (a) one-step step solid state reaction – LNMO with

space group $P4_332$ (b) two-step solid-state reactions (green triangles) – LNMO with space group Fd-3m (red triangles).

Ordered LNMO spinel (space group $P4_332$) was prepared by a solid-state reaction. Though the particle size is several microns, this material shows high rate capability and excellent cyclability [38]. The capacity was as high as 78 mAh/g at a 167C.The high rate capability observed agrees with our first-principles calculations, which show a low migration barrier for Li, and thus a high diffusion coefficient of around 10^{-9} – 10^{-8} cm^2/s. Both experiment and calculation suggest that micron-sized ordered LNMO can be a high rate electrode material with an excellent density.

2.4 Modification of LNMO

2.4.1 Cation doping and performance

2.4.1.1 M^+ ions

There are no reports found for doping LNMO by M+ ions like in the case of Li1+dMn2-dO4, where M=Li.

2.4.1.2 M^{2+} ions

Chen et al. have reported that Mg substitution lowers the polarization and enhances the overall insertion kinetics of spinel $Li_4Ti_5O_{12}$ by increasing electronic conductivity [19]. Hence, Mg-substituted Li–Mn–Ni–O spinel is expected to be a positive electrode material with high-specific energy and electronic conductivity than some transition metals substituted LNMO. Ooms et al. [39] have reported that Mg doping not only changes the voltage profile (4.70–4.75 V vs. Li/Li^+) of the LNMO materials but also stabilizes the host structure against repeated (de)intercalation of the Li^+ ions, demonstrating the reversibility of the system. The experimentally obtained discharge capacities at 0.1 C charge– discharge rate of $LiMg_{\delta}Ni_{0.5-\delta}Mn_{1.5}O_4$ ($\delta<0.10$) are close to the theoretical values (over 120 mAh/g). Locati et al. [40] synthesized nanoparticles $LiMg_{\delta}Ni_{0.5-\delta}Mn_{1.5}O_4$ with $\delta=0.07$. The electrochemical tests showed improvement of the material's cyclability, by reducing the particle size. Locati et al. [41] also reported that the nanosized spinel type material $LiMg_{0.05}Ni_{0.45}Mn_{1.5}O_4$ presents an ordered cubic spinel structure, good capacity retention upon cycling (131 $mAh.g^{-1}$ at C/10 and 117 $mAh.g^{-1}$ at 1 C), and good electronic conductivity (improved from 10^{-7} S/cm reported by N. Zhang et al. [42] to 10^{-6} S/cm at room temperature). It was concluded that the nanosize Mg-doped LNMO material exhibit a good Li-ion conductivity at room temperature and good stability upon cycling even at high C rate (Fig 2.8).

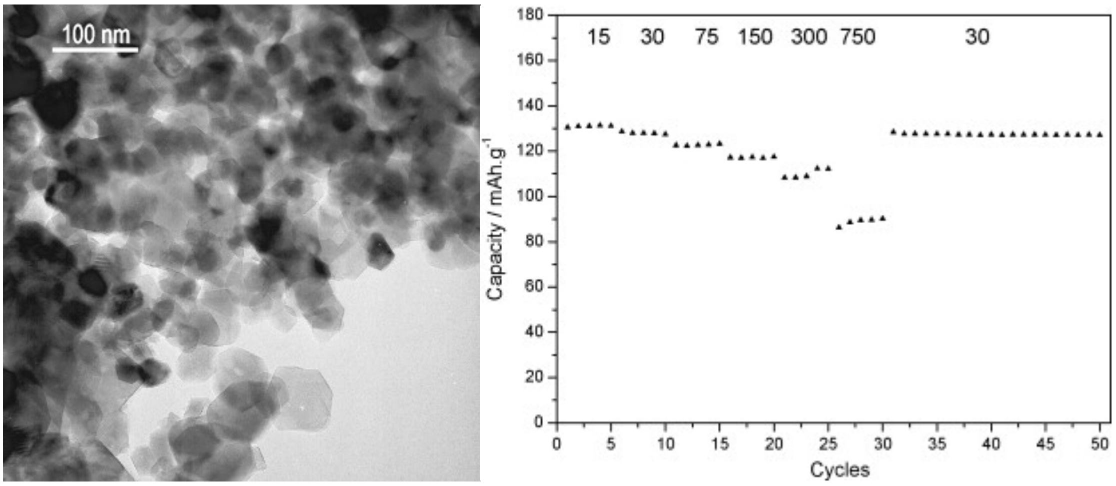

Fig 2.8. TEM image and cycling performance of $LiMg_{0.05}Ni_{0.45}Mn_{1.5}O_4$ at different discharge rates (0.1C, 0.2C, 0.5C, 1C, 2C,5C,back to 0.2C) from ref. [41]. Charge rate is equal to discharge rate, and 1 C=150 mA/g.

2.4.1.3 M^{2+} / M^{3+} ions

Iron: Fe^{2+} / Fe^{3+}

It has been reported that the charge–discharge curves of $LiNi_{0.5-x}Fe_xMn_{1.5}O_4$ compounds have three main plateaus, ascribed to the removal or filling of d electrons corresponding to the different redox pairs present: Fe^{4+}/Fe^{3+}, Ni^{4+}/Ni^{2+}, and Mn^{4+}/Mn^{3+} [43]. Liu et al. [44] reported that Fe doping can facilitate specific surface enrichments that could suppress the formation of thick SEI layers, can offer important benefits to improve the electrochemical performances of the 5 V spinel positive electrodes. The modelisation gives a good reproducibility of the experimental electrochemical curves, and then has proven to be of great interest as active positive electrode material for high voltage lithium-ion cells. This has been confirmed by Shin et al. who reported that segregation of Fe to the surface in doped $LiNi_{0.5-x}Fe_xMn_{1.5}O_4$ alleviates the unwanted reaction of the positive electrode surface with the electrolyte and thereby suppresses formation of the SEI layer and improves the cycle life at elevated temperatures regardless of the degree of cation ordering. [45]. Alcantara et al. [46] the $LiNi_{0.5-x}Fe_xMn_{1.5}O_4$ compounds prepared by the precipitation procedure, shows the best capacity retention, but $LiNi_{0.2}Fe_{0.3}Mn_{1.5}O_4$ exhibits the worst cycling performance among all samples. Fey et al. [47] reported $LiNi_{0.5-y}M_yMn_{1.5}O_4$ (M = Fe, Cu, Al, Mg; y=0.0–0.4) materials, and $LiNi_{0.4}Fe_{0.1}Mn_{1.5}O_4$ registered the best performance with a first-cycle capacity of 117 mAh/g and capacity retention of 78% over 60 cycles among all the compositions studied above. Ti and Fe double-doped LNMO reported by Léon et al. [48] also shows a good electrochemical performance, and the material containing 0.05 Fe + 0.05 Ti shows a two phase mechanism of lithium extraction and in contrast, the material containing 0.10Fe + 0.10Ti shows only one phase.

2.4.1.4 M^{3+} ions

Aluminium: Al^{3+}

It was reported that Raman spectra of Al-doped LNMO, $LiNi_{0.45}Al_{0.05}Mn_{1.5}O_4$ and $LiNi_{0.475}Al_{0.05}Mn_{1.475}O_4$ indicate that the structure is the ordered spinel with the space group $P4_332$ [21], see also Figs 2.9 and 2.10. Besides,$LiNi_{0.45}Al_{0.05}Mn_{1.5}O_4$, $LiNi_{0.475}Al_{0.05}Mn_{1.475}O_4$ and $Li_{1.05}Ni_{0.5}Al_{0.05}Mn_{1.45}O_4$ spinels have been synthesized by a thermo-polymerization method [49]. The Al-doping changes the space group of LNMO from ordered $P4_332$ to disordered Fd-3m under the same heat treatment conditions. It can significantly improve the cycling stability of LNMO. The capacity retentions of Al-doped spinels are over 99% after 100 cycles at room temperature. Even at 55 °C, the capacity retention of $Li_{1.05}Ni_{0.5}Al_{0.05}Mn_{1.45}O_4$ can reach 98% after 100 cycles. In addition, the rate performance of LNMO is also greatly improved by the Al-doping. The effects of Al substitutions for Ni and (or) Mn ions in the LNMO are somewhat different in that the $Li_{0.95}Ni_{0.45}Al_{0.05}Mn_{1.5}O_4$ shows faster capacity fading at elevated temperature than the $Li_{1.05}Ni_{0.5}Al_{0.05}Mn_{1.45}O_4$ sample. The latter one gives higher capacity retention at 55 °C and displays better rate capability. As a compromise, the Ni/Mn co-substituted sample $LiNi_{0.475}Al_{0.05}Mn_{1.475}O_4$ shows the best electrochemical performance with a high specific capacity during cycling at room and elevated temperatures, and excellent rate capability. The cyclic stability and rate property are significantly improved by Al doping without obvious capacity reduction in the optimized Al concentration of 0.05<2x<0.10. The $LiNi_{0.45}Mn_{1.45}Al_{0.1}O_4$ gives the best capacity retention

(95.4% after 500 cycles at 1C rate) and the best rate capability (119 mAh/g at 10C, about 93.7% of its capacity at 0.5C) at room temperature. The Al-doping can also dramatically suppress the exothermic reaction below 220 °C, thus improve the safety of the high voltage positive electrode material.

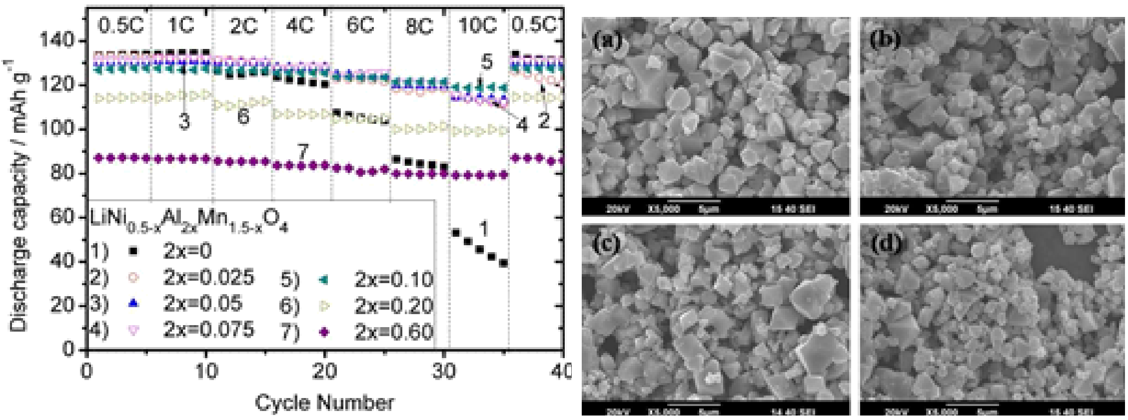

Fig.2.9. Left: Rate performance of the LNMO and the Al-doped spinels at various C rates. Right [49]: SEM images of electrodes: (a) LNMO, (b) $Li_{0.95}Ni_{0.45}Al_{0.05}Mn_{1.5}O_4$, (c) $LiNi_{0.475}Al_{0.05}Mn_{1.475}O_4$ and (d) $Li_{1.05}Ni_{0.5}Al_{0.05}Mn_{1.45}O_4$.

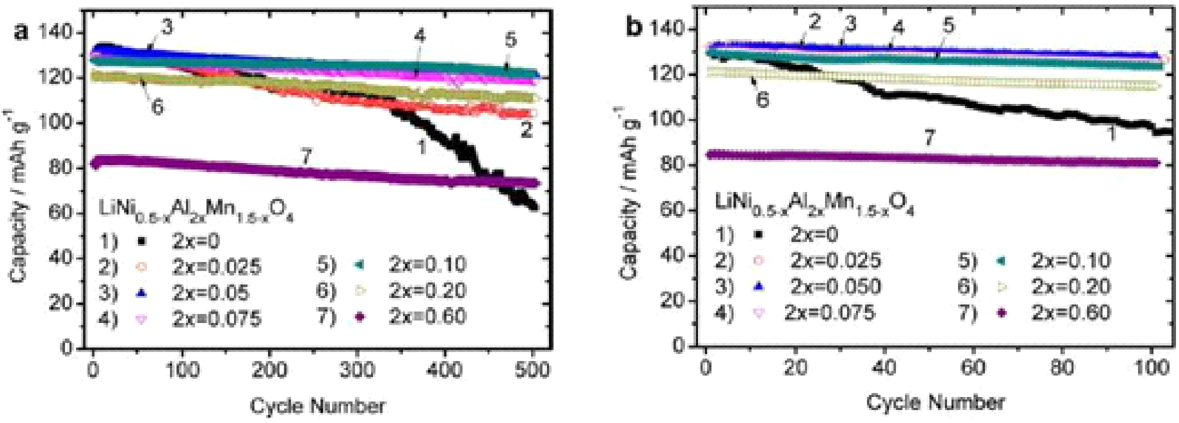

Fig.2.10. Cyclic performance of Li/$LiNi_{0.5-x}Al_{2x}Mn_{1.5-x}O_4$ ($0 < 2x < 0.6$) cells at (a) room temperature and (b) 55 °C. The cells were charged/discharged at 1C rate [49]

Chromium: Cr^{3+}

It has been reported that Cr^{3+} ions have high oxygen affinity, providing structural stability during cycling [50, 51]. In addition, the bonding energy of Cr–O is stronger than that of Mn–O and Ni–O. The stronger Cr–O bond is in favor of maintaining the spinel structure during cycling, and then prevents the structural disintegration of the material [52]. Liu et al. [52]

reported $LiNi_{0.4}Cr_{0.1}Mn_{1.5}O_4$ material prepared by a sol–gel method. The first discharge capacity of $LiNi_{0.4}Cr_{0.1}Mn_{1.5}O_4$ at the range of 3.5–5.0 V was 143, 118, and 111 mAh/g corresponding to current densities of 1.0, 4.0, and 5.0 mA/cm^2, respectively, and the capacity retention remained well after 50 cycles, see Fig.11. Liu et al. [53] also reported $LiNi_{0.4}Cr_{0.1}Mn_{1.5}O_4$ showing a good rate capacity and good capacity retention. Arunkumar et al. [24] reported $LiNi_{0.5-0.5x}Cr_xMn_{1.5-0.5x}O_4$ where $LiNi_{0.45}Cr_{0.1}Mn_{1.45}O_4$ exhibits the best combination of high 5 V capacity (128 mAh/g at 5–4.2 V) and excellent capacity retention (98% in 50 cycles) compared to 118 mAh/g and 92% for LNMO [54]. Aklalouch et al. [55] synthesized single phase $LiNi_{0.4}Cr_{0.2}Mn_{1.4}O_4$ spinel synthesized by a simple sucrose assisted combustion method, and it shows the highest rate capability with capacity retention of 92% at 60 C (1 C=147.5 mA/g or 0.260 mA/cm^2) discharge rate among LNMO-type positive electrodes and retains huge rate capability and large cycleability at high temperature (55 °C). In an earlier study they showed the role of the particle size on the electrochemical properties at 25 and at 55 °C. In spite of the great differences in particle size, the discharge capacity at 25 and at 55 °C for all samples is similar (Qdch ≈135mAh/g), and it is close to the theoretical one (Qtheo = 147.5 mAh/g). As a high discharge intensity was used (1C rate), these results show that Cr doped LNMO have high rate capability. The cycling performances at 25 and at 55 °C strongly change with the particle size; in fact, the improvement of the cycling stability on increasing the particle size all over the range explored has been demonstrated. The samples synthesized with nanometric particle size show scarce cycling stability, especially at high temperature. The large oxidation of the electrolyte on the surface of these samples explains their bad cycling performances. However, Cr-doped LNMO with particle sizes > 500nm exhibit a remarkable capacity retention. Finally, among the samples synthesized, those heated at 1000 and 1100 °C, showing high potential (E≈4.7 V), elevate capacity (Q≈135mAh/g), and remarkable cycling performances (capacity retention after 250 cycles >96%, normalized capacity loss by cycle <0.02%). Park et al. [26] reported that the spinel structure of $LiNi_{0.5-x}Cr_xMn_{1.5}O_4$ was maintained up to x = 0.05 and Cr doping accelerated chemical reaction kinetics, producing well-facetted $LiNi_{0.5-x}Cr_xMn_{1.5}O_4$ (x = 0.05) particles faster than others. Besides, they found that the amount of weight loss during TG analysis was decreased as the Cr content was increased. This suggested that the structure of the $LiNi_{0.5-x}Cr_xMn_{1.5}O_4$ was stabilized by Cr doping due to high oxygen affinity of Cr. Also, the Cr doping provided a wider plateau during charge–discharge tests by suppressing the Mn^{3+} oxidation, which was related to the change of the charge–discharge curves from a two step profile to a one step profile. The initial discharge capacity $LiNi_{0.5-x}Cr_xMn_{1.5}O_4$ positive electrode was increased and capacity retention was improved with Cr content, indicating improvement of structural stability the positive electrode [26]. Furthermore, it was concluded that the excellent electrochemical property of Cr-doped material results from the better chemical and structural stability with less Jahn–Teller distortion for the Cr-doped spinel [56].

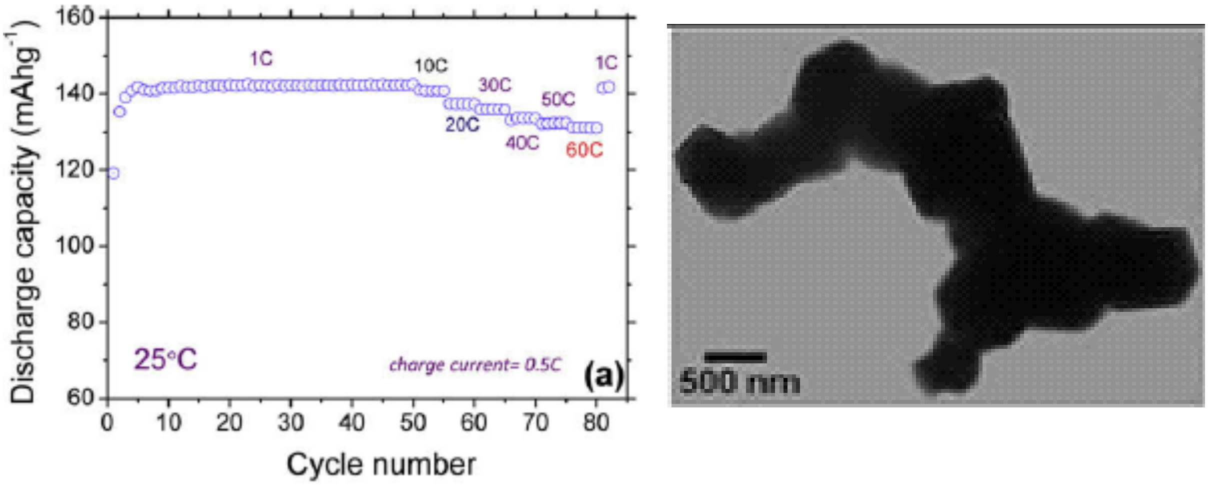

Fig.2.11. TEM image and cycling performance of $LiNi_{0.4}Cr_{0.2}Mn_{1.4}O_4$ *spinel at different discharge rates from ref. [55]. Charge current is 0.5 C, and 1 C is 147.5 mA/g or 0.260 mA/cm*^{2}*.*

Also, segregation of Cr to the surface in doped $LiNi_{0.5-x}Cr_xMn_{1.5}O_4$ alleviates the unwanted reaction of the positive electrode surface with the electrolyte and thereby suppresses formation of the SEI layer and improves the cycle life at elevated temperatures regardless of the degree of cation ordering. [45]. These overall results have been further confirmed by Xiao et al. [57].

Cobalt: Co^{3+}

It has been reported that Co^{3+} in the oxide matrix improves electronic conductivity of LNMO [58], and the bonding strength of transition metal element and oxygen can be strengthened by the incorporation of trivalent Co in the structure. Li et al. [59] reported $LiNi_{0.5-x}Co_{2x}Mn_{1.5-x}O_4$ ($0 \le x \le 0.1$) prepared by a spray-dry process re-annealed in O_2 exhibit good cyclic performances when they were operated at a rate of 0.15 C (0.2 mA/cm^2. The reversible capacities after 50 cycles are 113, 110, and 104 mAh/g for the samples with x=0.05, 0.075 and 0.1, respectively, which are about 96% of their initial discharge capacities. Oh et al. [58] reported the compound $LiNi_{0.5}Co_xMn_{1.5-x}O_4$ showing at 5C (700 mA/g) and 10C rates (1.400 mA/g), capacities of around 100 and 10 mAh.g^{-1}, capacities of $LiNi_{0.45}Co_{0.05}Mn_{1.5}O_4$ were 118 and 103 mAh/g at 5C and 10C rates, respectively. There are some reports that Co-doped LNMO has a better electrochemical property than that of LNMO due to a smaller lattice parameter [60] and higher lithium diffusion coefficient [61] during the charge–discharge process.

Gallium: Ga^{3+}

Ga-doped spinels suggest a high degree of cation disordering, as shown by FTIR analysis [45]. However, neutron diffraction results suggest that it rather reflect the domain size of the cation ordering and the presence of antiphase boundaries between domains (disorder between domains) rather than simply reflecting the degree of cation disorder on the transition metal site. Therefore, the term “degree of cation ordering” should be taken with care, and includes merely short-range-ordered domains as developed from the neutron diffraction results. For a further understanding of the effects of cation ordering and surface segregation on the cyclability and rate capability, the doped $LiNi_{0.5-x}Ga_xMn_{1.5}O_4$ (x = 0.05, 0.08) spinels, prepared with the same method as the other spinel samples, have also been compared to each other before and after post-annealing at 700 °C (Fig 2.12). The lower gallium content sample (x = 0.05) exhibits a greater degree of cation ordering (larger cation-ordered domain size) compared to the x = 0.08 sample after post-annealing at 700 °C, as suggested by FTIR. Despite the difference in cation ordering, the x = 0.05 and 0.08 samples before and after post-annealing at 700 °C show similar, superior cyclability at room temperature and 55 °C compared to the undoped spinel when they are cycled at a low current density of C/6 rate. The cycle degradation due to a high degree of cation ordering in the post-annealed x = 0.05 sample is thought to be somewhat compensated for by stabilization of the surface with gallium segregation, resulting in only a slightly higher capacity fade and lower Coulombic efficiency than the x = 0.08 sample. As the charge transfer resistance increases with increasing Ga^{3+} segregation to the surface (increasing gallium doping level), the charge-transfer resistance becomes a rate-limiting factor at higher C rates for the rate capability of the $LiNi_{0.5-x}Ga_xMn_{1.5}O_4$ spinels. Therefore, the 900°C x = 0.05 sample shows higher rate capability than the 900 °C x = 0.08 sample. On the other hand, the 700 °C post-annealed x=0.05 sample displays a lower rate capability than the 700 °C post-annealed x = 0.08 sample because of higher charge-transfer resistance resulting from a higher degree of cation ordering. The undoped LNMO spinels before and after post-annealing at 700 °C exhibit lower rate capabilities than the $LiNi_{0.5-x}Ga_xMn_{1.5}O_4$ (x = 0.05 and 0.08) spinels before and after post-annealing. The poor or varying performances of the undoped LNMO spinel could now be readily explained from the results of this study to be due to the high reactivity of the positive electrode surface with the electrolyte at the high operating voltages of 4.7 V that is accompanied by the formation of thick SEI layers and a higher degree of cation ordering (or larger cation-ordered domain size).

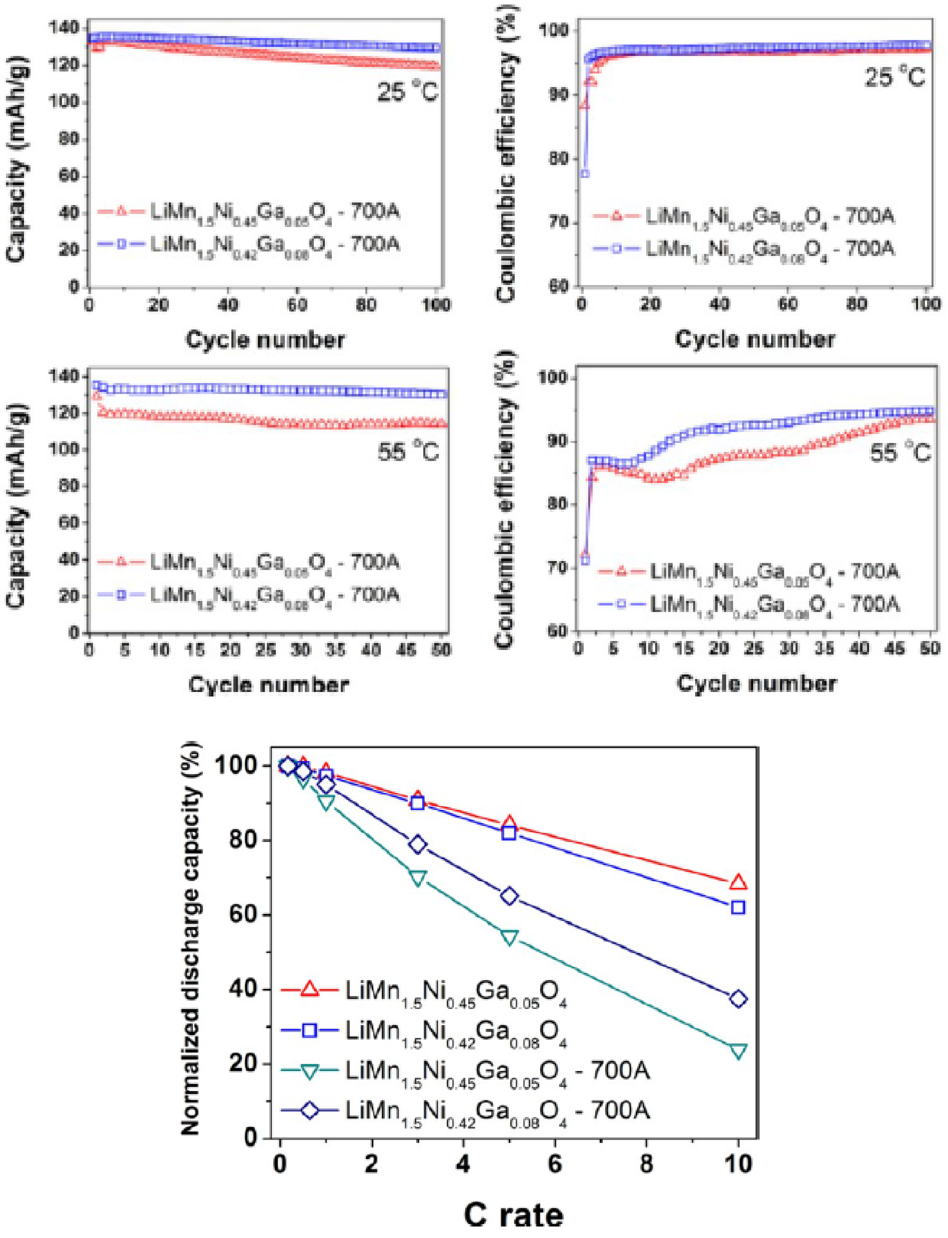

Fig.2.12. Up: Cyclability and Coulombic efficiency of the $LiNi_{0.5-x}Ga_xMn_{1.5}O_4$ (x = 0.05, 0.08) samples after postannealing at 700 °C [45]. Down: Normalized discharge capacity values at various C rates of the $LiNi_{0.5-x}Ga_xMn_{1.5}O_4$ (x = 0.05, 0.08) samples before (no suffix) and after (suffix of 700A) postannealing at 700 °C.

2.4.1.5 M^{3+} / M^{4+} ions

Manganese: Mn^{3+} / Mn^{4+}

It is stressed that for this dopant concentrations are taken small so as to avoid a discussion on $LiMn_2O_4$ doped with nickel. The most recent paper was published by Song et al. [25]. A Mn-rich $LiNi_{0.5-d}Mn_{1.5+d}O_4$ (d=0.05 and 0.08) slowly cooled from 900 °C showed elimination of the rock-salt phase, but not the Mn^{3+} associated with a disordered spinel fraction separating domains of short-range order, gives the best electrochemical performance consistent with an enhancement by greater electronic conductivity while eliminating an obstructing rock-salt phase [25]. These Mn-doped LNMO retained Mn^{3+} in a single spinel phase prepared by annealing at 700 °C in air. However, they contained two spinel phases, one with long-range ordering of Ni^{2+} and Mn^{4+} and another Mn-rich spinel. The Mn-rich volume fraction exhibited two distinguishable Mn^{4+}/ Mn^{3+} redox energies: one at 4.0 V and the other at 4.3 V, versus Li^+/Li^0. The 4.3V redox energy is clearly identified with the existence of the long-range-ordered phase, which should not contain any Mn^{3+} ions. Therefore, it is speculated that this couple is associated with an oxygen-poor interface phase between long-range ordered domains or at the interface between the disordered, Mn-rich spinel and the long-range ordered domains. The long-range ordered spinel phase gives a single voltage plateau at 4.75 V versus Li^+/Li^0; the state of charge of a small voltage step from 4.7 V to 4.75 V signals the degree of short-range ordering in the sample. The Mn-rich samples have a reduced Ni concentration at the surface and exhibit a better charge/discharge cycling at 55 °C, which signals that the Ni $^{4+}/Ni^{2+}$ couple oxidizes the electrolyte. On the other hand, a larger Mn^{3+} concentration at the surface means a higher rate of disproportionation into Mn^{2+} and Mn^{4+} with Mn^{2+} dissolution; however, reduction of the surface Ni stabilizes the spinel against oxidation of the electrolyte at elevated temperatures (such as 55 °C).

Titanium: Ti^{3+} / Ti^{4+}

Ti substituted LNMO led to the disordering of the transition metals and consequently lowered the symmetry from primitive simple cubic structure ($P4_332$) to face centered spinel (Fd-3m). Kim et al. [36] reported that $LiNi_{0.5}Ti_xMn_{1.5-x}O_4$ exhibited higher operating voltages, faster lithium-ion diffusion, and better rate capability than Ti-free LNMO confirmed by electrochemical tests. In order to improve further the electrochemical performance of $LiNi_{0.5}Ti_xMn_{1.5-x}O_4$, the effect of the Bi surface treatment on $LiNi_{0.5}Ti_xMn_{1.5-x}O_4$ was examined. The cycle behaviour was found to be improved by bismuth treatment. A retention capacity of around 85% was achieved after 500 cycles at 20 °C, while a retention capacity as high as 70% was obtained after 500 cycles, even at 45 °C [62]. In addition, Liu et al. [63] reported that the capacities of $LiNi_{0.5}Ti_{0.3}Mn_{1.2}O_4$ with good cycle performance were 134, 127 and 76 mAh/g at the current rates of 0.1C, 0.5C, and 1C, respectively. Alcántara et al. [64] reported the structure and electrochemical performance of $LiNi_{0.5}Ti_xMn_{1.5-x}O_4$ ($0.05 \leq x \leq 0.6$) spinel oxide materials. It shows that titanium is incorporated into the LNMO to form solid solutions, and the cubic unit cell parameter increases with the substitution of manganese by titanium, and the substitution of small amounts of manganese by titanium in LNMO leads to a net improvement of the reversible capacity and capacity retention. In the Li–Ni–Mn–Ti–O system, which is the most studied to date, an abrupt capacity decrease with increasing Ti content at high potential was already noted [65], in spite of chemical diffusion determinations (from GITT measurements) giving an increase in the lithium chemical diffusion coefficient with Ti substitution [66]. This confirms that the blocking effect of the d0 Ti^{4+} cations is the major factor limiting the redox intercalation–deintercalation mechanism [65]. Highly Ti-doped $LiNi_{0.5}Ti_{0.3}Mn_{1.2}O_4$ materials was used to fabricate an all spinel cell with an negative electrode of $Li_4Ti_5O_{12}$. The results are shown in Fig 2.13 [67] and Fig 2.14

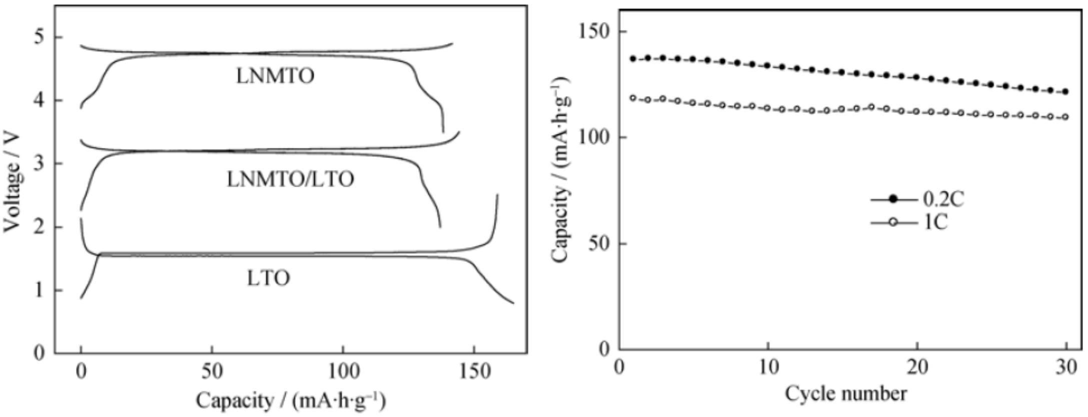

Fig 2.13. Left: Charge/discharge curves for $Li_4Ti_5O_{12}$, $LiNi_{0.5}Ti_xMn_{1.5-x}O_4$, and $LiNi_{0.5}Ti_xMn_{1.5-x}O4/Li_4Ti_5O_{12}$ cells at 0.2C, and (right) cycle performances of the LNMTO /LTO cell at 0.2C and 1C [67]

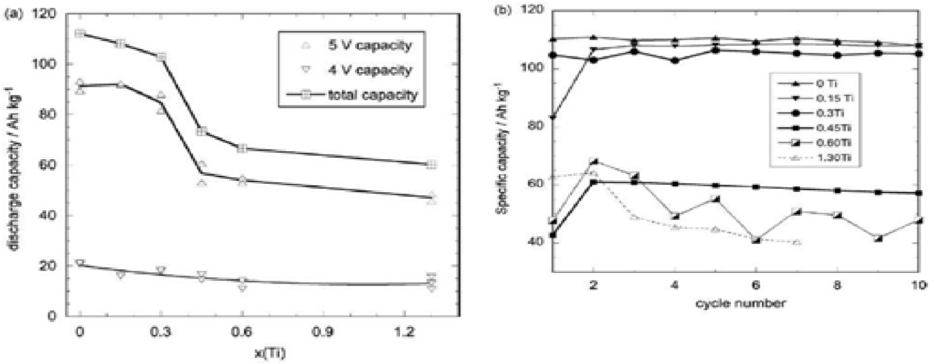

Fig 2.14. (a) 4V and 5V capacity of $LiNi_{0.5}Ti_xMn_{1.5-x}O_4$ spinels as a function of x 3rd cycle data, galvanostatic cycling at C/20 between 3.75 and 4.85 V, and (b) Evolution of the capacity with cycle number for different titanium contents [65].

2.4.1.6 M^{4+} ions

Ruthenium: Ru^{4+}

Wang et al. [68] synthesized the Ru-doped LNMO (Fig.15). The rate capability and cycling performance were significantly improved by Ru doping as shown in [68]. The spinel $Li_{1.1}Ni_{0.35}Ru_{0.05}Mn_{1.5}O_4$ and $LiNi_{0.4}Ru_{0.05}Mn_{1.5}O_4$ show excellent rate capability and cyclic performance under 10C charge–discharge rate (Fig 2.16). The capacity retention after 500 cycles at 10 C discharge rate are 91% and 84% due to minimized polarization and improved electronic conductivity, respectively. The electronic conductivity conductivities of the LNMO, $Li_{1.1}Ni_{0.35}Ru_{0.05}Mn_{1.5}O_4$, and $LiNi_{0.4}Ru_{0.05}Mn_{1.5}O_4$ measured with EIS at RT are 1.18×10^{-4}, 5.32×10^{-4}, and 4.73×10^{-4} S/cm, respectively. Hence, they believe that Ru-doped LNMO are promising positive electrode materials for future high-power applications.

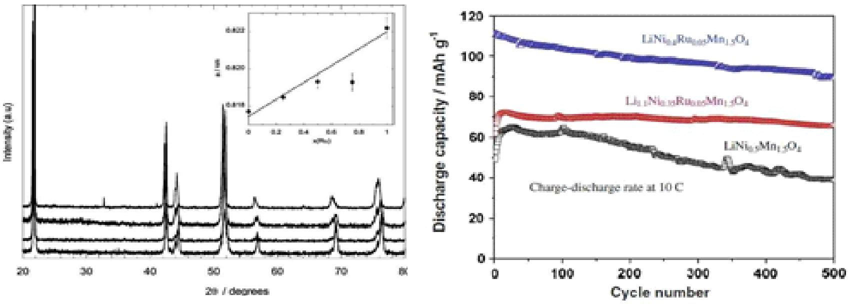

Fig 2.15. Left: XRD patterns in the $LiNi_{0.4}Ru_{0.05}Mn_{1.5}O_4$ *series as a function of nominal ruthenium content x (from bottom to top: x = 0.25, 0.50, 0.75, 1.0). Inset: variation of the spinel cell parameter with x [65]. Right: Rate capability and cycling performance of Ru-doped LNMO from ref. [68], where 1C corresponds to 147 mA/g.*

Zirkonium: Zr^{4+}

Raman spectra of Zr-doped LNMO, $LiNi_{0.5}Zr_{0.05}Mn_{1.45}O_4$ indicate that the structure is the ordered spinel with the space group $P4_332$ [69]. Hence, Zr doped spinel, $LiNi_{0.5}Zr_{0.05}Mn_{1.45}O_4$, showed a trivial amount of 4V peaks in their CVs. Thus it implies that the Zr dopant could not suppress the structural transformation during the required annealing process.

2.4.1.7 M^{5+} ions

Niobium: Nb^{5+}

The structure and electrochemical performance were studied by TG/DTA, XRD, SEM, CV, EIS and galvanostatic charge/discharge tests [70]. The result shows that Nb doping achieves some encouraging results. Both crystal domain size and electronic conductivity are influenced by this kind of doping. This high voltage $LiNi_{0.525}Nb_{0.05}Mn_{1.425}O_4$ material presents good capacity retention of 110.5mAh/g at 1C and 102.7mAh/g at 5C discharge rate (0.1C charge rates). Nb-doped LNMO displays remarkable cyclability without much fade at various high C rates compared to the drastic fade seen with the LNMO. Nb-doped LNMO exhibits a good Li-ion diffusion coefficient at room temperature and good stability upon cycling even at 1C charge/discharge rate (Fig 2.16). The discharge capacity of the $LiNi_{0.525}Nb_{0.05}Mn_{1.425}O_4$ still remains near 100% of original values even after 100 cycles. The obtained results demonstrate that a small amount of Nb substitution in LNMO can improve the rate cycling performance of this positive-electrode material, making it more attractive for future practical application.

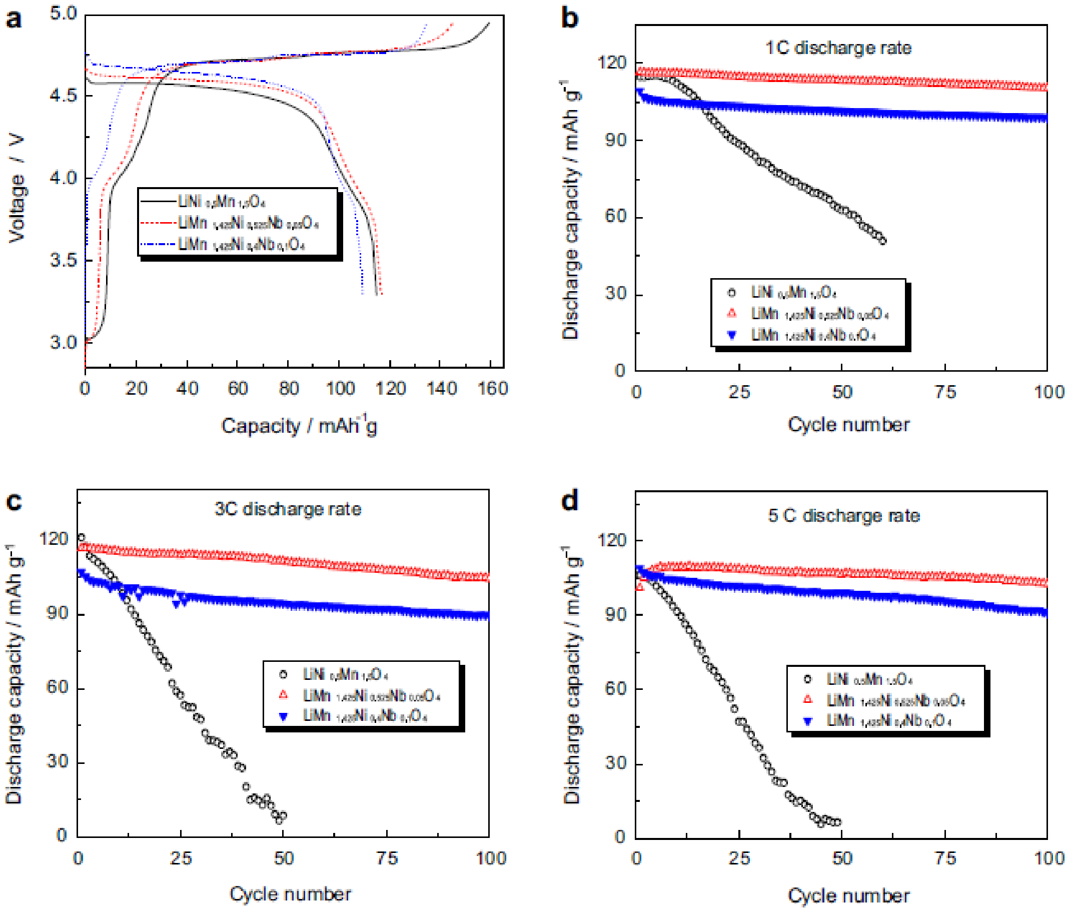

Fig 2.16 (a) Initial charge/discharge curves (0.1C charge rate and 1C discharge rate) and cycling performance at (b) 1C discharge rate, (c) 3C discharge rate, and (d) 5C discharge rate of LNMO with and without Nb doping [70].

2.4.1.8 Multiple doping: Cr^{3+}, Al^{3+}, Zr^{4+}

Oh et al. [21] reported the structure of $LiNi_{0.5-x}M_{x+y}Mn_{1.5-y}O_4$ (M = Cr, Al, Zr) compound, but the charge–discharge performance was not reported. Al and Zr-doped materials was ordered spinel, but Cr-doped material was normal spinel. Cr doped material has the higher electronic conductivity and structural stability with less Jahn–Teller distortion may result in the excellent electrochemical property of spinel [21].

2.4.2 Anion doping and performance

X- ions

2.4.2.1 Fluorine: F^-

Fluorine-substituted samples display better resistance against HF attack than fluorine-free samples. Hence, the concentrations of Ni and Mn in the electrolyte of the former are lower than those of the latter [69]. It is proposed that a fluorine coating effectively reduces dissolution of particles into the electrolyte [71]. Fluorine doping can suppress the formation of NiO impurity and simultaneously reduces the voltage polarization [72]. Kim et al. [71] reported that $LNMO_{1-x}F_x$ ($0 \leq x \leq 0.1$) positive electrodes synthesized by ultrasonic spray pyrolysis method exhibit superior structural properties and rate capability, especially at high C rates. In addition, a small amount of fluorine substitution for oxygen enhances the electrochemical properties and thermal stability. Yang et al. [72] reported $LiNi_{0.5}Mn_{1.5}O_{3.975}F_{0.025}$ prepared by sol–gel technique re-annealing in oxygen. Stoichiometric amounts of acetate was dissolved in distilled water by stirring, and LiF was used as fluorine source, and then evaporated at 70–80 °C until a transparent gel. The gel precursors w ere decomposed at 450 °C in air for 5 h and then calcined at 850 °C in air for 12 h. For the re-annealing process, the powder sample was heated again at 600 °C under oxygen flow for 15 h. The result shows that fluorine doping enhances the initial capacity from about 130 mAh/g to over 140 mAh/g between 3.5 and 5.2 V comparing with LNMO (Fig.20). Yang et al. [73] further reported fluorine-doped 5 V positive electrode materials $LiNi_{0.5}Mn_{1.5}O_{4-x}F_x$ ($0.05 \leq x \leq 0.2$) prepared by sol–gel and post-annealing treatment method. The cycling results and SEM images shown in Fig. 17 indicate that the particles become larger and the distribution more uniform with the increase of the fluorine amount, and discharge capacity decreases with enhanced fluorine content. The strong Li–F bonding may hinder Li^+ extraction, leading to a lower reversible capacity. In view of the balance between the capacity and cyclic stability, $LiNi_{0.5}Mn_{1.5}O_{3.9}F_{0.1}$ gives the best performance.

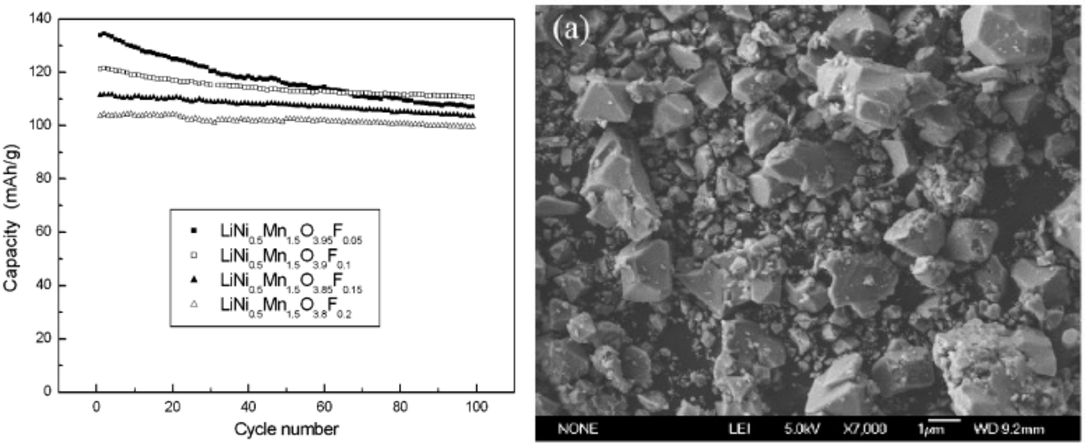

Fig 2.17 : Left :Cyclic performances of $LiNi_{0.5}Mn_{1.5}O_{4-x}F_x$ (x = 0.05, 0.1, 0.15, 0.2). Right : SEM of $LiNi_{0.5}Mn_{1.5}O_{3.9}F_{0.1}$ with a particle size ca 0.1-0.2 um)

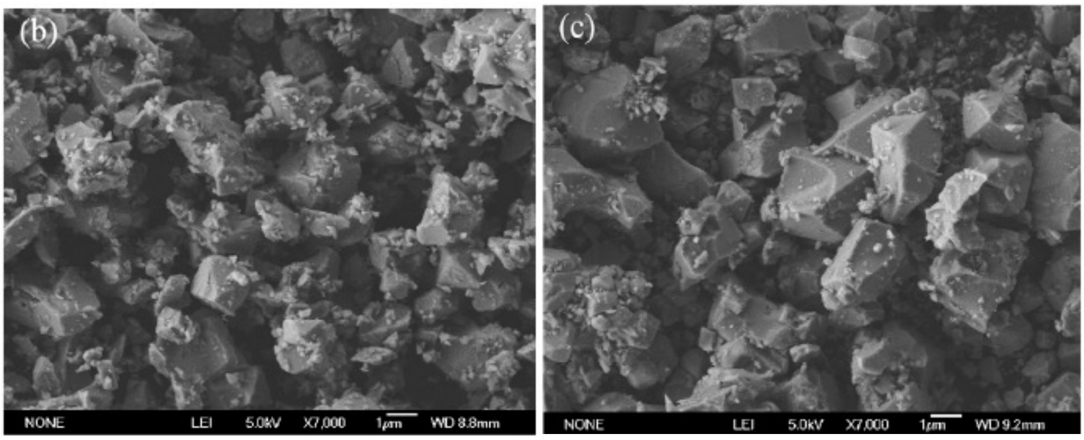

Fig 2.18. Cycling performance and SEM images of fluorine-doped 5 V positive electrode materials $LiNi_{0.5}Mn_{1.5}O_{4-x}F_x$ ($0.05 \leq x \leq 0.2$. Charge and discharge measurements of the coin cells were carried out at a current density of 29.4 mA/g (0.2C)[73].

2.4.2.2 X^{2-} ions

Sulfur: S^{2-}

Sun et al. [74] reported the $LiNi_{0.5}Mn_{1.5}O_{4-x}S_x$ (x=0 and 0.05) compounds synthesized by co-precipitation using the metal carbonate $(Ni_{0.5}Mn_{1.5})CO_3$ as a precursor. The $(Ni_{0.5}Mn_{1.5})CO_3$ powder was mixed with $LiOH{\cdot}H_2O$ and sulfur powder for doping, followed by final calcination at 500 and 800 °C in a box furnace. The sulfur-doped spinel LNMO displays excellent capacity retention and rate capability in the 3-V region, compared with LNMO spinel material. The enhanced electrochemical behaviour of the sulfur-doped spinel is attributed to the rough morphology of the primary particles with smaller particle size.

Multiple doping:Cr^{3+},Al^{3+},F^-

Multi-substituted material $LiNi_{0.475}Al_{0.01}Cr_{0.04}Mn_{1.475}O_{3.95}F_{0.05}$ was synthesized with a citric acid assisted sol–gel method [75]. It delivers satisfactory cycle performance at 1C, achieving 128.6 mAh/g (at 20 °C) and 129.5 mAh/g (at 55 °C), with the capacity retention of 98% and 99.7% after 100 cycles, respectively. Besides, when cycled at 10C at 20C and 55C, it still can reach to 97.8 mAh/g (at 20 °C) and 102.7 mAh/g (at 55 °C) with a capacity retention of 99.1% and 95.6% after 100 cycles, respectively (see Fig 2.19).

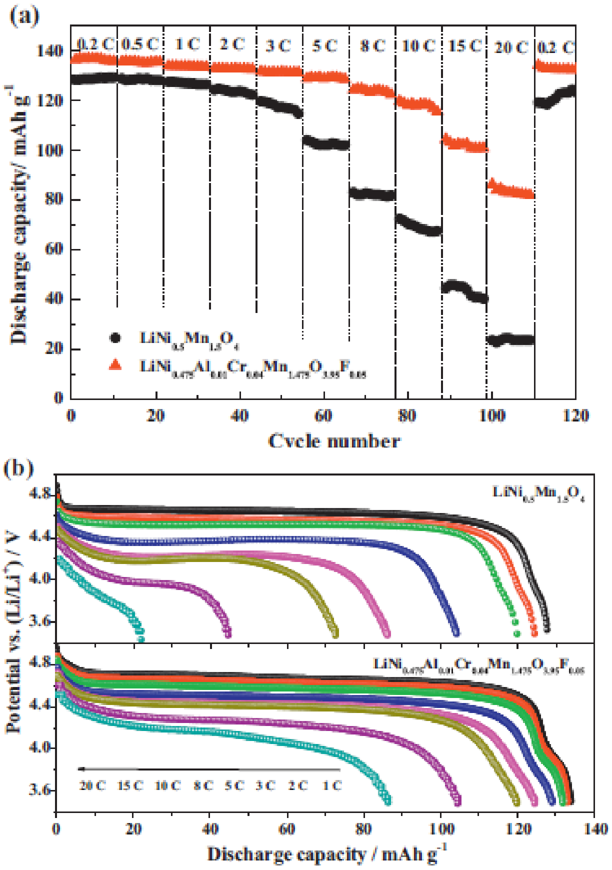

Fig 2.19 (a) Rate capability of LNMO and $LiNi_{0.475}Al_{0.01}Cr_{0.04}Mn_{1.475}O_{3.95}F_{0.05}$ *and (b) discharge profiles at rates (1–3C, 5C, 8C, 10C, 15C and 20C) of LNMO and* $LiNi_{0.475}Al_{0.01}Cr_{0.04}Mn_{1.475}O_{3.95}F_{0.05}$ *[75].*

2.5 MORPHOLOGIES

The morphology was said to play a crucial role in the performance of LNMO. At the one hand, small particles may have improved power performance due to short lithium and electron migration lengths. However, small particle also have a high surface to volume ratio and thereby showing increased degradation once exposed to the electrolyte. Clearly, the morphology of LNMO is strongly dependent on the synthesis method employed. Nevertheless a general trend in the behaviour with respect to the morphology can be obtained. The main findings are gathered here. Nano- and micro-sized LNMO particles are prepared via the thermal decomposition of a ternary eutectic Li–Ni–Mn acetate [76]. Lithium acetate, nickel acetate and manganese acetate can form a ternary eutectic Li–Ni–Mn acetate below 80 °C. After further calcination, nano-sized LNMO particles can be obtained at an extremely low temperature (500 °C). When the sintering temperature goes above 700 °C, the particle size increases, and at 900 °C micro-sized LNMO particles (about 4μm) are obtained. Electrochemical tests show that the micro-sized LNMO powders (sintered at 900 °C) exhibit the best capacity retention at 25 °C, and after 100 cycles, 97% of initial discharge capacity can still be reached. Nano-sized LNMO powders (sintered at 700 °C) perform the best at low temperatures; when cycled at −10 °C and charged and discharged at a 1C rate, nano-sized LNMO powders can deliver a capacity as high as 110mAh/g (see Fig 2.20). It is stressed that here not only morphology is involved, but also the structures Fd-3m and P$4_3$32, due to the various temperatures applied.

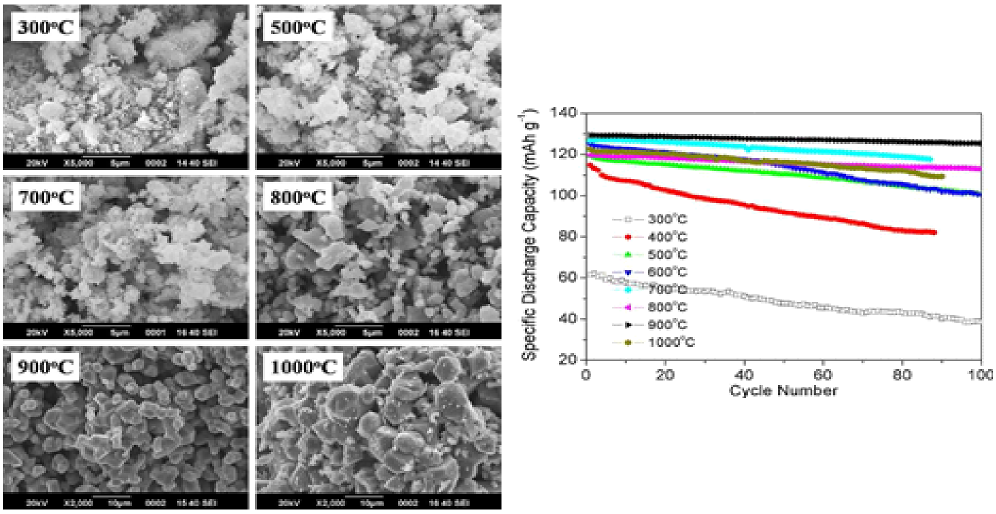

Fig 2.20. Left: SEM images of the as-synthesized samples. Right: Cycling performance of LNMO samples as shown on the left. [76].

In Ref. [77], the high temperature part has been studied in more detail, so as to maintain the Fd-3m structure. There, six spinel LNMO (LNMS) samples with different morphologies were synthesized via a PVP (polyvinylpyrrolidone)-assisted gel combustion method by varying the calcination temperature from 800 °C to 1050 °C [77]. XRD tests were used to characterize the crystal structure and phase purity. SEM images clearly revealed the evolution of the particle size (from sub-micrometer to micrometer), shape and degree of agglomeration with increasing calcination temperature. Charge/discharge tests indicated that the LNMO samples composed of larger primary particles had better cyclic performance than those composed of smaller primary particles. Among the six samples, LNMO calcined at 1050 °C and LNMO calcined at 1000 °C showed excellent capacity retentions of 97.6% and 97.3%, respectively, after 200 cycles with a 1C rate at RT. The cyclic performance of of these samples at 55 °C was also remarkable, showing capacity retentions of 97.1% and 96.0%, respectively, after 50 cycles at a 1C rate. Rate capability tests indicated that the single crystal- like LNMO calcined at 1000 °C with a moderate particle size (1–3 mm) showed the best rate capability. It delivered 132.9 mAh/g, 130.2 mAh/g, 128.1 mAh/g and 124.5 mAh/g at rates of 1C, 5C, 10C and 15C, respectively. Electrochemical impedance spectroscopy (EIS) measurements showed that larger primary particles exhibited slower interface impedance increases upon cycling than smaller particles – see Fig 2.21 and Fig 2.22.

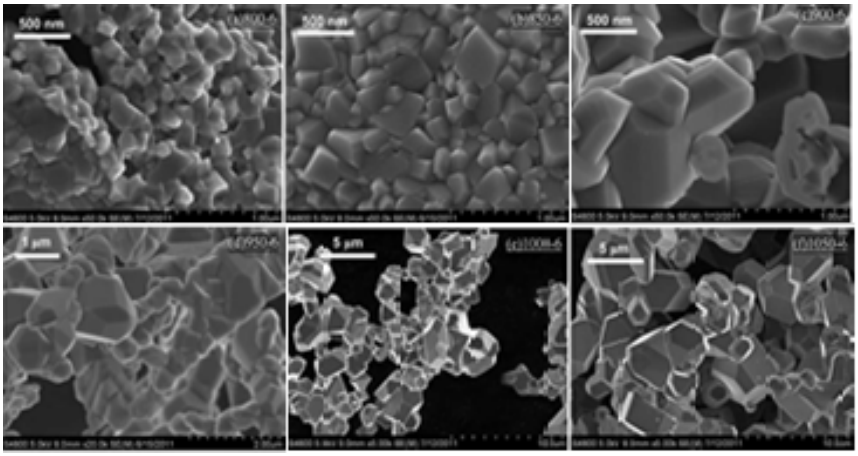

Fig 2.21. High-magnification SEM images of the LNMO samples [77].

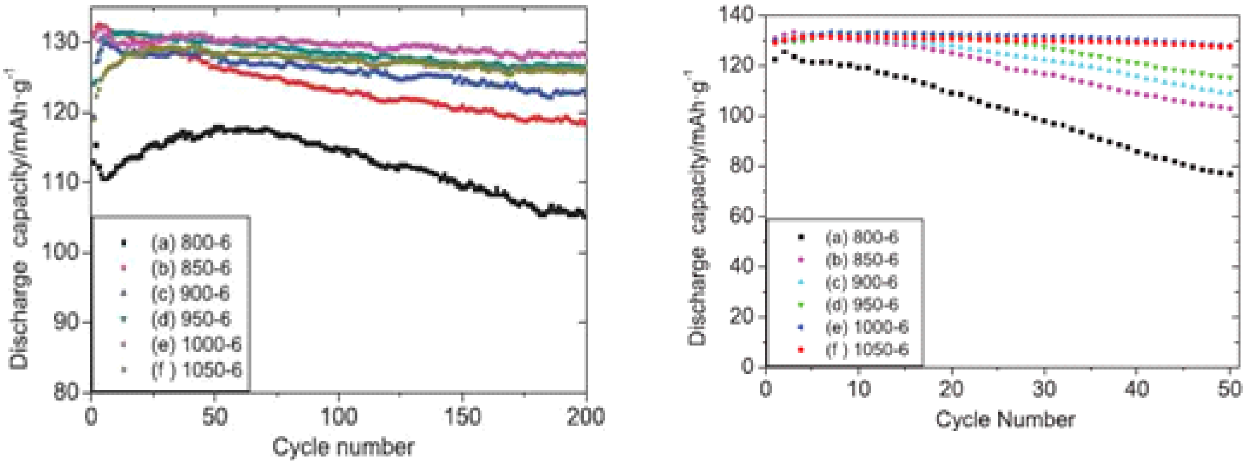

Fig 2.22. Cyclic performance of the LNMO samples cycled at RT (on the left) and at 55 °C (on the right). The charge/discharge rate was 0.5 C/1 C, and the voltage range was 3.5–5.0 V [77].

2.6 INTERFACE/INTERPHASE BEHAVIOUR

2.6.1 General aspects

Surface films on LNMO are formed once exposed to an electrolyte, which then determines the electrochemical kinetics during the prolonged cycling, particularly at elevated temperatures (40–60 °C), which then leads to an increase in their impedance, and not to a pronounced degradation of the active mass [78]. The surface chemistry developed is important for the cycling performance and storage behaviour of the electrodes. XPS measurements prove the precipitation of LiF, C–F and P–Fx species as well as organic compounds (probably, polyethers) on the electrodes. The surface chemistry of LNMO electrodes depends strongly on the temperature [78]. This is clear from impedance measurements performed first at low temperature (30 °C), then at high temperature (60 °C), and finally at 30 °C. It was demonstrated that when the initial electrode's surface chemistry is developed at the high temperature (60 °C), it is nearly invariant at a lower temperature as well, and thereby, the impedance remains steady. Besides, from micro-Raman measurements, it was shown that the LNMO active mass is stable in its structure upon prolonged cycling/storage at 30 °C [78]. At high temperatures (60–70 °C), there are changes in the surface/bulk of the active mass correlated with dissolution of Mn and Ni and the formation of λ-MnO_2. However, these changes are not uniform, but rather localized, occurring in selected domains of the active mass. Impedance spectroscopy indicated that there was a spontaneous formation of a layer on the surface of LNMO in contact with an electrolyte [79]. The equivalent circuit was described by Aurbach et al. [78] and are usually described by four major features: high frequency and medium frequency flat semicircles, which can be attributed to surface films and interfacial charge-transfer, respectively (coupled with film and/or interfacial capacitances), a low frequency Warburg-type element that reflects the solid state diffusion of Li-ions, and finally, at the very low frequencies, the Z′ versus Z″ plot becomes a steep, nearly vertical line, which reflects the capacitive behaviour of the electrode (Li-ion insertion and corresponding charge-transfer). In many cases, the separation among the above major processes and time constants is not clear, and hence, the high-to-medium frequency spectra may appear as a single flat semicircle, which reflects both Li-ion migration through surface films and interfacial charge-transfer. Hence, it consists of the resistance of the solution, Rs, in series with a block consisting of the resistance of the electrode's surface, Rf, in parallel with its capacity, Cf, which in turn is in series with another block consisting of the charge-transfer resistance, Rct in parallel with the double-layer capacitance, Cdl. A Warburg impedance at a lower frequency that is related to solid-state Li^+ ion diffusion can also be seen at a lower frequency. The impedance spectrum taken during the first 7 h before cycling fresh cell shows two semicircles at high to medium frequency followed by a capacitive line, as shown in Fig.6. Both semicircles are attributed to the surface layer, while the charge-transfer resistance is too high to be measured. During the 7 h, the impedance spectra showed no change in their characteristics. The presence of high frequency semicircles at rest potential before charging suggests the spontaneous formation of a surface layer consisting of lithium-conducting species, namely, $Li_xPO_yF_z$, polyethers –R–O–R–, and metal alkoxides ROM when the positive electrode is put in contact with the electrolyte [79]. The FTIR and XPS measurements on the positive electrode–electrolyte interface of cycled and uncycled electrodes revealed the spontaneous formation of $Li_xPO_yF_z$ species and polyethers on the surface. The thickness of the layer increased with cycling, but not upon storage, as a 2 month storage did not affect the performance of the material nor lead to a continuous growth of the surface layer other than the spontaneously formed one. Upon prolonged cycling, there exist ROCO2M species on the surface, possibly polycarbonates, and the capacity fade seems to be linked to the increasing thickness of these layers as well as the formation of LiF. There is some evidence, although not conclusive of dissolution of Mn cations from the surface, as XPS suggests that the Mn:Ni ratio decreases from 3:1 for a pristine electrode to less than 1:3 after cycling for 100 cycles. Clearly, the impedance depends strongly on the electrolyte chosen. Thermal and electrochemical stability of the conventional carbonate-based and ionic liquid solvents [80], and surface film formation are studied in a highly oxidizing condition; in the potential range of 3.5–4.9 V (vs. Li/Li+) at an elevated temperature (55 °C). The following points are summarized. (i) The high-voltage positive electrode (LNMO) is successfully cycled in the ionic liquid solvent at 55 °C. But this positive electrode shows a failure within a few cycles in the carbonate-based electrolyte ($LiPF_6$/EC/DEC). The decisive factor leading to this difference seems to be the composition of surface film that is deposited in the earlier period of cycling. The inorganic fluorinated species are dominant in the film derived from the carbonate electrolyte, whereas organic carbon species from the ionic liquid. () As demonstrated in this work, the surface film enriched by organic species seems to be more desirable than inorganic ones. It is likely that organic films give an effective passivation behaviour, even if they are thin, indebted to a compact and uniform coverage on electrode surface. The impedance data

(Fig 2.23), however, can be explained with the same equivalent circuit as shown below (see Fig.25) [81].

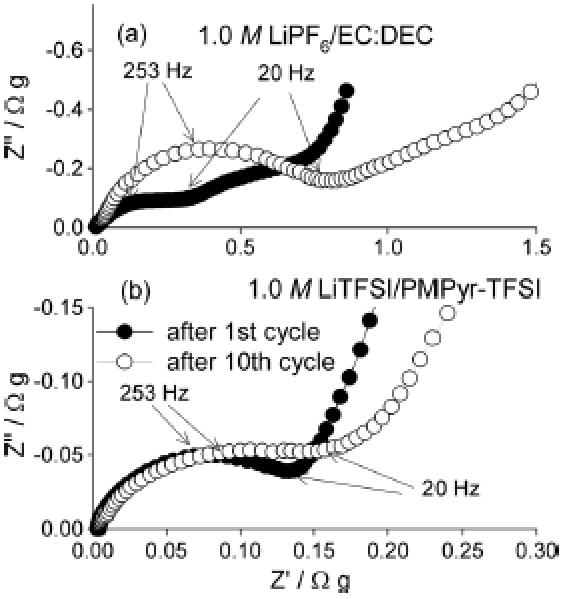

Fig 2.23. Evolution of ac impedance spectra with cycling in two electrolytes [80].

Cation-ordering and surface characteristics in the high-voltage $LiMn_{1.5}Ni_{0.5}O_4$-based spinels greatly influence both the cyclability and rate capability. In-depth neutron diffraction studies reveal that the cation-ordered domain size is strongly dependent on the synthesis conditions, with the domain size increasing with annealing at lower temperatures, e.g., 700 °C. The segregation of M = Cr, Fe, and Ga to the surface in doped $LiNi_{0.5-x}M_xMn_{1.5}O_4$ alleviates the unwanted reaction of the positive electrode surface with the electrolyte and thereby suppresses formation of the SEI layer and improves the cycle life at elevated temperatures regardless of the degree of cation ordering (see Fig 2.24). Furthermore, it is believed that the suppression of cation ordering with doping enhances the rate capability because of an increase in the electronic and lithium-ion conductivities. However, too much segregation of the dopant ions to the surface leads to a growth of larger cation-ordered domains in the bulk, resulting in a decrease in the rate capability. Although not mentioned explicitly, in the report of Sha et al. [75] a similar behaviour may expected for Al-Cr-F multiple doped LNMO as measured by impedance spectroscopy.

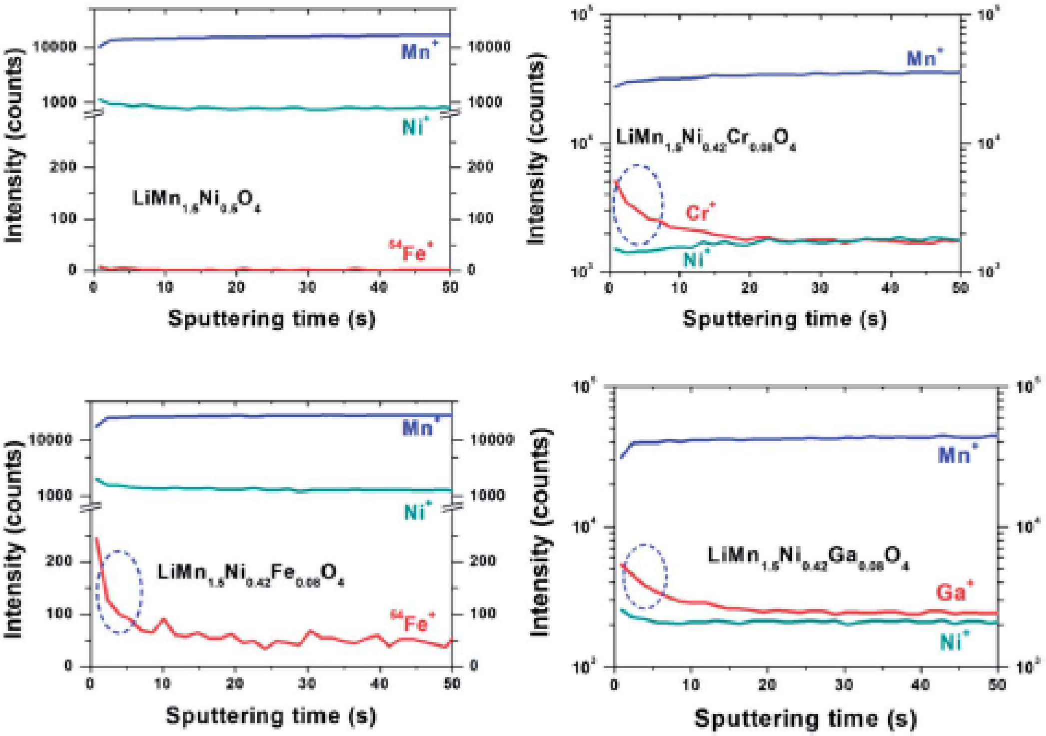

Fig 2.24. TOF-SIMS depth profiles of the $LiNi_{0.5-x}M_xMn_{1.5}O_4$ (M =Cr, Fe, and Ga; x = 0, 0.08) samples after annealing at 700 °C [82]

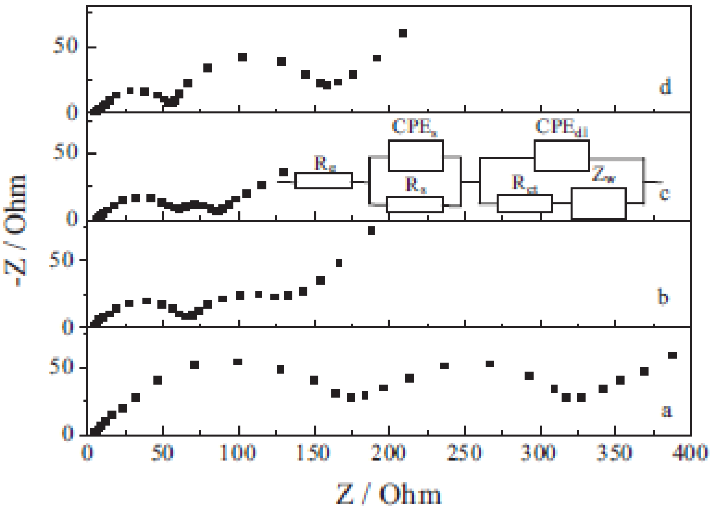

Fig 2.25.EIS spectra of the bare and carbon-coated LNMO spinels after 50 cycles. Figures (a)–

(d) for samples a, b, c and d, respectively. The insert represents the equivalent circuit [81].

A poor columbic efficiency of $LiNi_{0.5}Mn_{1.5}O_{4-d}$ is explained by the electrolyte decomposition at high voltage and/or the formation of solid electrolyte interphase (SEI) [83]. The existence of an SEI is observed using TEM (Fig 2.28). It was observed that LNMO underwent aging in the electrolyte: the pristine sample was soaked in $LiBF_4$ EC-DEC (volume 1:1) electrolyte for 5 days at room temperature. Then it was washed in DEC solvent and dried for the observation. Fig.26 indicates that the surface structure of LNMO is stable during aging and no SEI film is formed. This result is different with $LiCoO_2$ nanosized particle, on which a 2–5 nm SEI film is formed after soaking in solvent and electrolyte. According to recent investigation on the SEI film formation on bare $LiMn_2O_4$ thin film, the SEI formation is absent on (110) surface but formed on (111) surface during soaking. The absence of the SEI film on (−110) face of LNMO is consistent with the results with $LiMn_2O_4$. Fig 2.28 shows the TEM images of de-lithiated $LiNi_{0.5}Mn_{1.5}O_{4-d}$. After charging to 4.9 V at a rate of 0.05 C followed by keeping at this voltage for 24 h, a non-uniform amorphous SEI film with a thickness ranging from 2 to 10 nm is observed. The SEI is well spread on the positive electrode surface without any cracks. It indicates clearly that SEI is formed on LNMO during electrochemical reactions. It is known that the SEI film on the surface of $LiMn_2O_4$ is dynamically changed and does not prevent dissolution of Mn^{2+} completely. Therefore, the formation of a non-uniform SEI film could lead to the low columbic efficiency. Typically an SEI layer is an ionic conductor and an electronic insulator. Although the formation of SEI prevents the further degradation of electrolyte, thick layer may hinder the Li^+ transportation and lower the rate performance. Fourier transform infrared spectroscopy and Raman Spectroscopy, etc. It is mainly composed of inorganic species such as MF, LiF, Li_2CO_3 and $Li_xPO_yF_z$ or $Li_xO_yBF_z$ as well as organic species such as polyethers and carbonates. And the portion of these species varies based on the type of electrodes, electrolytes and temperatures. While some of them are not stable at high voltage. Therefore coating LNMO with e.g. Al_2O_3, ZnO, Bi_2O_3, and $AlPO_4$, will then can modify the formation of SEI thus improving the electrochemical performances significantly [83].

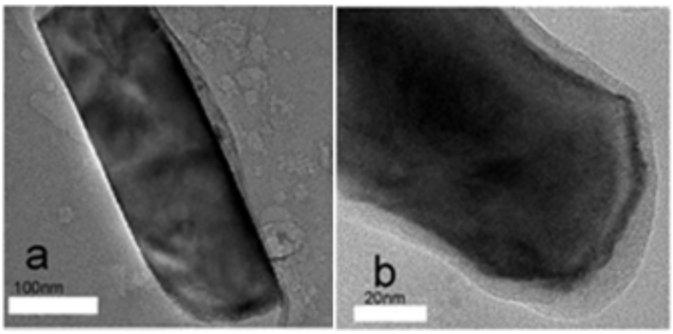

Fig 2.26. SEI film on LNMO [83].

2.6.2 Metal oxides

Zinc oxide: ZnO

It was shown that the surface coating of the LNMO positive electrode with ZnO drastically improves the electrochemical cycling behaviour of the material in the 5 V range at 55 °C [84]. TEM analysis of the cycled positive electrode suggested that the rapid degradation of the LNMO positive electrode at 55 °C may be related to the formation of the graphitic surface phase, blocking the Li migration. The suggestion is further supported by the ZnO-coated positive electrode with no surface phase, which exhibited excellent capacity retention at 55 °C (Fig 2.27). A compact and continuous ZnO coating was precipitated on the surface of the positive electrode material, whereas the formulation of the anode electrode was optimized by adding nanolithium powder as pre-lithiating agent [85]. The resulting Li-ion cell combines the intrinsic superior safety and inherent overcharge protection of TiO_2 compared to graphite, with mitigated liquid electrolyte decomposition on the positive electrode side provided by the ZnO coating. The protective effect of ZnO was demonstrated by analysing the spinel solubility in aqueous HF. The presence of ZnO clearly reduced the spinel solubility in this medium, as reflected in the decreased amounts of Ni and Mn dissolved [86]. The rate capability of these LMNO thin films is very high. Moreover, coating the electrode surface decreases the irreversible capacity but at the cost of some rate performance [87], due to changes in surface kinetics. Instead of a transfer from solvated Li ions from the liquid electrolyte onto the electrode surface and subsequent reaction, the transfer now takes onto ZnO or LiPON. Ionic conduction through the coating is necessary for Li ions to reach the LMNO electrode surface. There is also an additional transfer resistance at the coating/electrode interface. Coating with a thick layer (here LiPON) may also reduce the electrode surface area, thus decreasing the contact area with the electrolyte solution.

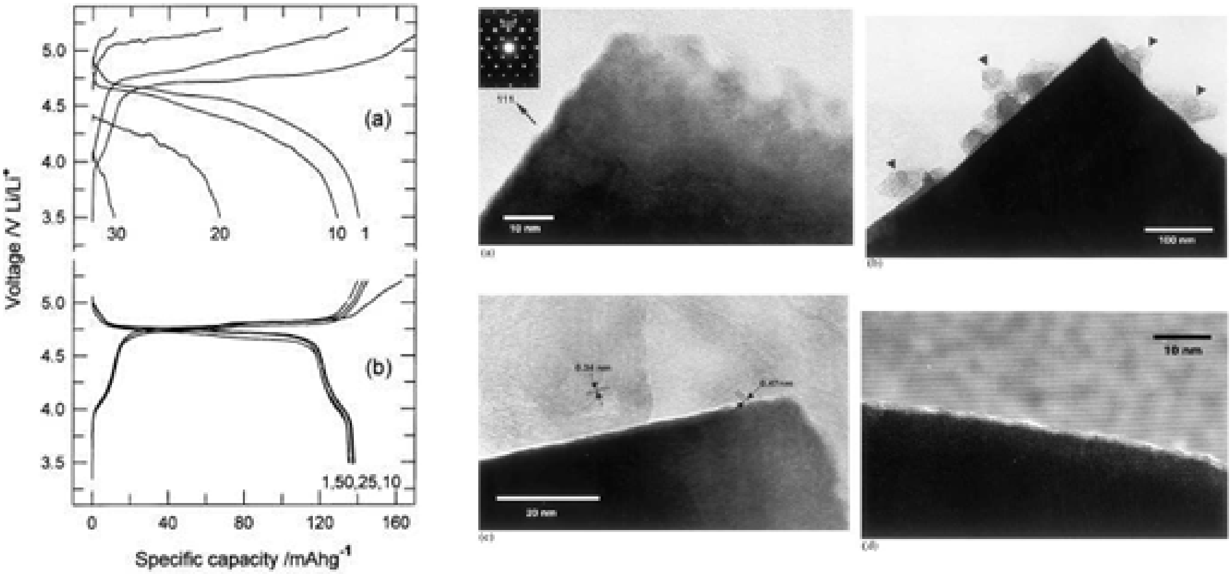

Fig 2.27. Left: Charge/discharge curves for (a) uncoated LNMO, (b) ZnO-coated LNMO at 55 °C [84]. Right: TEM images of (a) ZnO-coated LNMO particle; (b) uncoated LNMO particle after cycling at 55 °C (arrows indicate the carbonaceous phases); (c) uncoated LNMO particle after cycling at 55 °C at a higher magnification (002 graphitic and 111 spinel spacings are shown for comparison); (d) ZnOcoated LNMO particle after cycling showing no carbonaceous phases on the particle surface [84].

Bismuth oxide: Bi_2O_3

Among the coating materials, it is worth noting that Manthiram modified the surface of the 5V positive electrode material by Bi_2O_3 coating (Fig 2.28), which rendered both excellent rate capability and improved cycling performance [60, 62]. Further investigation was found that Bi_2O_3 was reduced on the positive electrode surface during electrochemical cycling to metallic Bi, which is an electronic conductor. Thus, this achievement was ascribed to the suppressed corrosion reaction and the fast electron transfer. Unfortunately, the microstructural breakage of the Bi_2O_3 protection layer caused by the reduction process hindered its commercial application. The effect of the Bi surface treatment was investigated. Bi surface film was confirmed to be fabricated on the surface of 5V spinel $LiNi_{0.5}Ti_xMn_{1.5-x}O_4$ by TEM and EDX analysis. The thickness of the Bi film was around 20 nm, while the Bi compound was confirmed to be Bi_2O_3 by XRD analysis. The cycle behaviour was found to be improved by Bi treatment. A retention capacity of around 85% was achieved after 500 cycles at 20 °C, while a retention capacity as high as 70% was obtained after 500 cycles, even at 45 °C. The improvement effect was higher at an elevated temperature, while the storage performance also improved with Bi treatment. The capacity fading after storage at 60 °C was suppressed. More than 90% of the recovery capacity after storage for 1 week at 60 °C was obtained with Bi treatment. The increase in the resistance in storage was also suppressed with Bi treatment, which would be attributable to the suppression of electrolyte decomposition by Bi film. It was found that the Bi treatment had the effect of decreasing the dissolution of Mn, Ni and Ti of the elements of positive electrode active material by ICP. The content of the positive electrode active material elements on the anode after storage for 1 week at 60 °C, decreased by about 40% in comparison with non Bi-treated. Based on the above results, the Bi surface coating was found to have a remarkable effect on the improvement of the cells with 5V spinel.

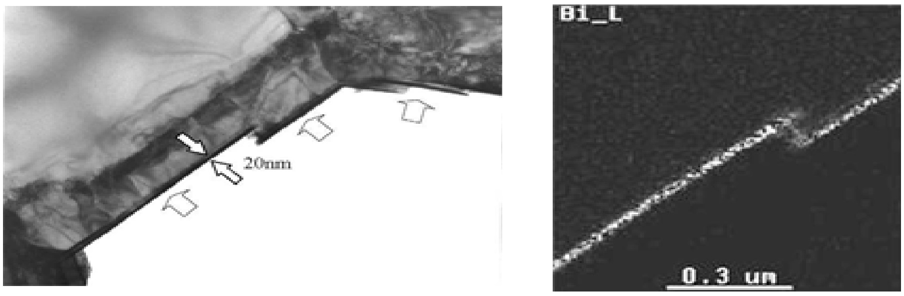

Fig 2.28. Left: TEM image of the cross-section of Bi 1 wt% treated 5V spinel [62].

Right: Atomic mapping image of Bi of Bi-treated $LiNi_{0.5}Ti_xMn_{1.5-x}O_4$ *by EDX analysis [62].*

The electrochemical performances and discharge kinetics of the bare and nanosize Al_2O_3- and Bi_2O_3-modified 5 V spinel positive electrode LNMO have been systematically investigated [88]. The surface modification is found to improve both the cycling performance especially at elevated temperature and rate capability. EIS study indicates that the improved cycling performance and enhanced rate capability of the surface-modified samples is due to the suppression of the formation of thick SEI layers and the consequent enhanced charge transfer kinetics. Large potential step chronoamperometry study shows that the whole discharge process is controlled by both the phase transformation and lithium ion diffusion in the bulk material besides the charge-transfer reaction. While the surface modification does not influence the phase transformation and lithium ion diffusion kinetics significantly, it enhances the charge-transfer reaction kinetics occurring at the positive electrode/electrolyte interface, resulting in an enhancement in rate capability.

Silicon dioxide: SiO_2

A relatively easy and efficient procedure to produce LNMO coated by fumed silica was shown [89]. Thereto, a weighted amount of fumed silica was dispersed in ethanol by 1 h sonication treatment followed by vigorous stirring for half an hour, thus a colloid with silica was obtained. Then, the as-prepared LNMO powders were added to the above colloid so that the amount of the fumed silica corresponded to 0.5, 1.0 and 3.0 wt% of LNMO powders, respectively. These mixtures were treated with sonication for 30 min, and stirred by a magnetic stirrer for 2 h. A subsequent slow evaporation of the solvent at 50 °C resulted in the LNMO powders with silica coating. The coated powders were then calcined at 500 °C for 5 h in order to ensure complete adhesion of the silica particles with the core material LNMO. The LNMO spinels remain their structure with distinct boundaries after surface modification, and the surfaces of the coated samples are covered with a porous, nanostructured, amorphous SiO2 layer. The coated LNMO samples display obviously improved capacity retention rate as high-voltage positive electrode materials in 1M LiPF6 in a mixture of EC/DMC at an elevated temperature (55 °C), and the improvement effect enhances with the increase of SiO2 content in their surfaces. The lower HF content in electrolyte resulting from the reaction between SiO_2 and HF and the mechanical separation effect of the SiO_2 coating result in relatively lower content of LiF in the surfaces of the coated samples, and this may be responsible for better electrochemical cycling stability of the SiO_2-coated LNMO positive electrode materials.

Lanthanum strontium manganese oxide: $La_{0.7}Sr_{0.3}MnO_3$

Pristine and $La_{0.7}Sr_{0.7}MnO_3$- coated LNMO positive electrode materials were prepared by a sol-gel method [90]. Compared to the pristine LNMO, $La_{0.7}Sr_{0.7}MnO_3$-coated LNMO has a better cycle stability and rate performance, especially at elevated temperature (Fig 2.29). The presence of $La_{0.7}Sr_{0.7}MnO_3$- coated-layer on LNMO surface is considered to play a positive role in suppressing the dissolution of Mn from the spinel material and improving electronic conductivity, resulting in reducing capacity fading and enhancing high C rate performances.

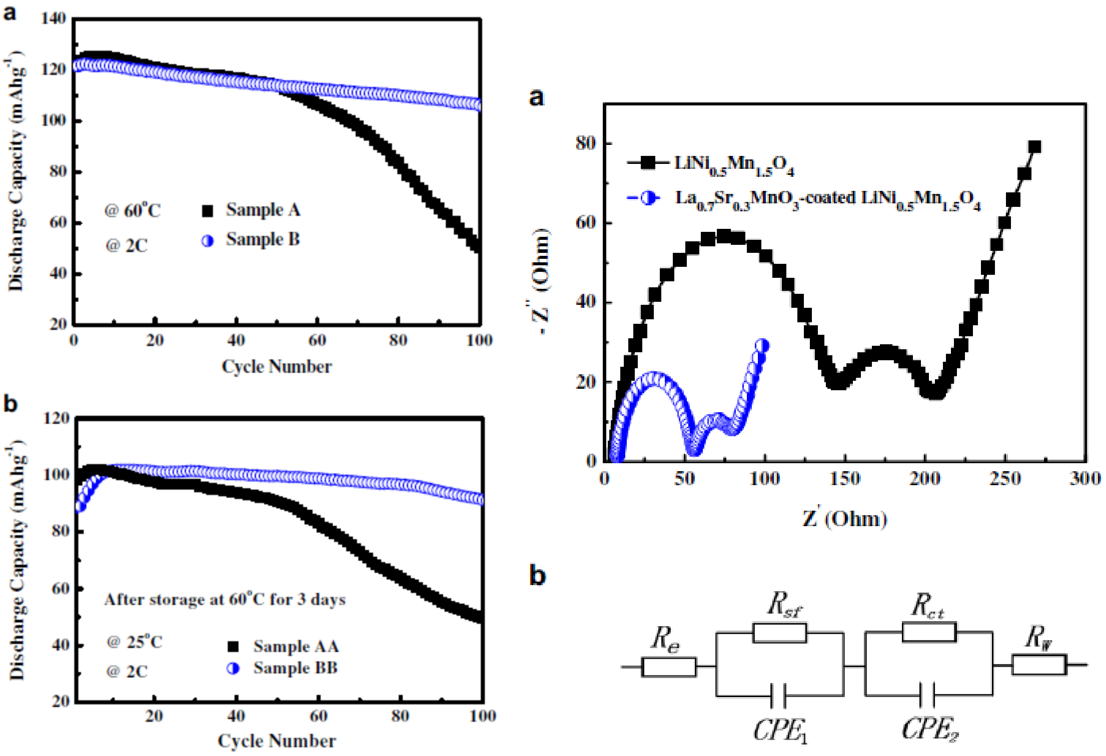

Fig 2.30. Left: (a) The discharge capacity versus cycle number for LNMO (denoted as Sample A) and $La_{0.7}Sr_{0.7}MnO_3$-coated LNMO (denoted as Sample B) at 2C and 60 °C; (b) Room temperature cycling performances of LNMO and $La_{0.7}Sr_{0.7}MnO_3$-coated LNMO thermal-annealed at 60 °C for 3 days at 2C, denoted as Sample AA and Sample BB respectively [90]. Right: (a) The EIS profiles of LNMO (denoted as Sample A) $La_{0.7}Sr_{0.7}MnO_3$-coated LNMO (denoted as Sample B) after 50 cycles at a 2C rate in 60 °C at the fully discharge state; (b) the equivalent circuit for EIS results fitting [90]

2.6.3 Comparison of Al_2O_3, $AlPO_4$, ZnO and Bi_2O_3 coatings

An electrostatic self-assembly method has been employed to modify the surface of the 5 V spinel positive electrode $LiNi_{0.42}Co_{0.16}Mn_{1.42}O_4$ with 2 wt % nanosize Al_2O_3, ZnO, Bi_2O_3, and $AlPO_4$ (Fig 2.31) [60]. The surface modified samples with a much more stable surface chemistry suppress the development of SEI layer and thereby improve the electrochemical performances significantly compared to the bare $LiNi_{0.42}Co_{0.16}Mn_{1.42}O_4$. However, the surface modified samples also differ among themselves in their electrochemical performances due to the different functions of the four surface modification materials investigated. Specifically, although both the ZnO and $AlPO_4$ modification layers act only as a protection shell between the active positive electrode material surface and the electrolyte, the Al_2O_3 and Bi_2O_3 modification layers offer, respectively, fast lithium-ion diffusion channel and fast electron-transfer channel, in addition to acting as a protection shell. The study demonstrates that surface modifications may prove to be a viable approach to utilize the high-voltage positive electrodes in lithium-ion cells. The data presented here illustrate the criteria for choosing appropriate surface modification materials that can maximize the overall electrochemical performance. Although surface modification with materials like the ones investigated here may generally be perceived to impede the electron and lithium-ion transport and thereby degrade the rate capability, the suppression of undesired SEI layer formation along with favorable lithiumion and electron-diffusion pathways results in enhanced rate capability and cyclability (Fig 2.32).

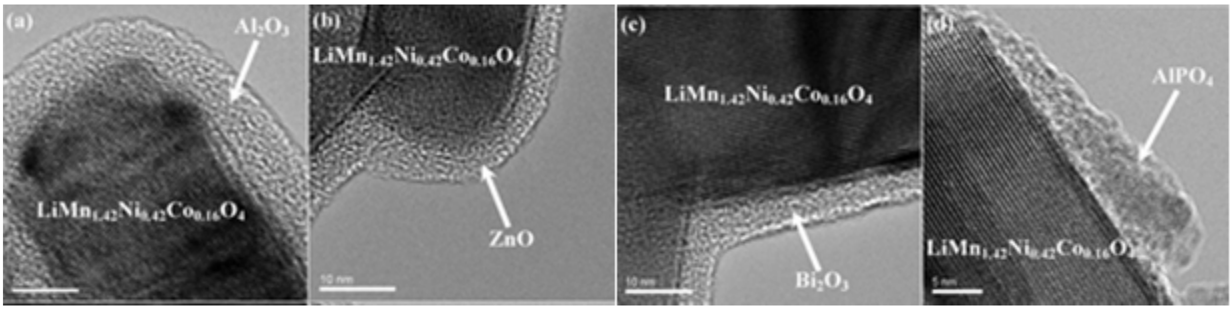

Fig 2.31. High-resolution TEM images of 2 wt % (a) Al_2O_3, (b) ZnO, (c) Bi_2O_3, and (d) $AlPO_4$-coated $LiNi_{0.42}Co_{0.16}Mn_{1.42}O_4$ [60].

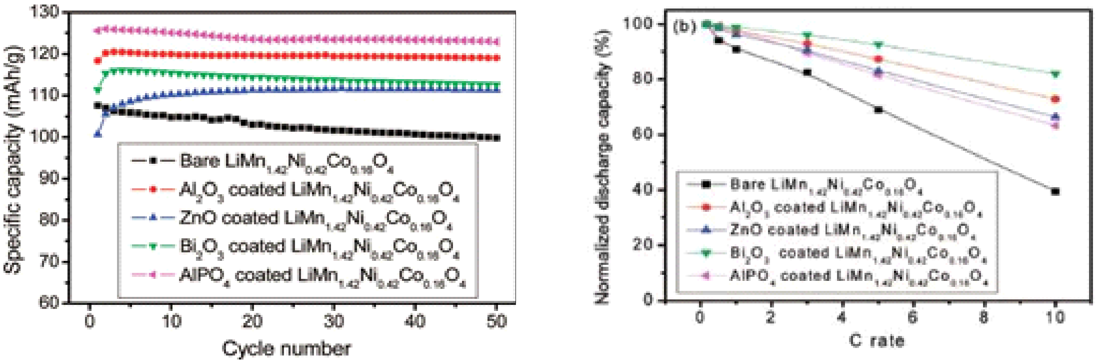

Fig 2.32. Left: Cycling performances of the bare and 2 wt % Al_2O_3, ZnO,) Bi_2O_3, and $AlPO_4$-coated $LiNi_{0.42}Co_{0.16}Mn_{1.42}O_4$, and (b) normalized discharge capacity at 50th cycle [60].

Zirconium oxide zirconium pyrophosphates: ZrO_2 or ZrP_2O_7

Spinel LNMO particles were modified by coating their surface with ZrO_2 or ZrP_2O_7 [91]. Coin cells with the ZrO_2- coated LNMO positive electrode showed remarkable improvement in cycling stability, with capacity retention of 96% after 150 cycles at 55 °C, whereas the pristine and ZrP_2O_7-coated LNMO positive electrodes exhibited a capacity retention of only 73% and 80%, respectively, after the same cycling period (Fig 2.33). The DSC analysis indicated that the coating also improved the thermal stability significantly. These excellent properties might have originated from the suppression of the interfacial resistance increase between positive electrode and electrolyte by protecting the positive electrode against surface electrolyte reactivity with formation of homogeneous and dense nano-particles of ZrO_2.

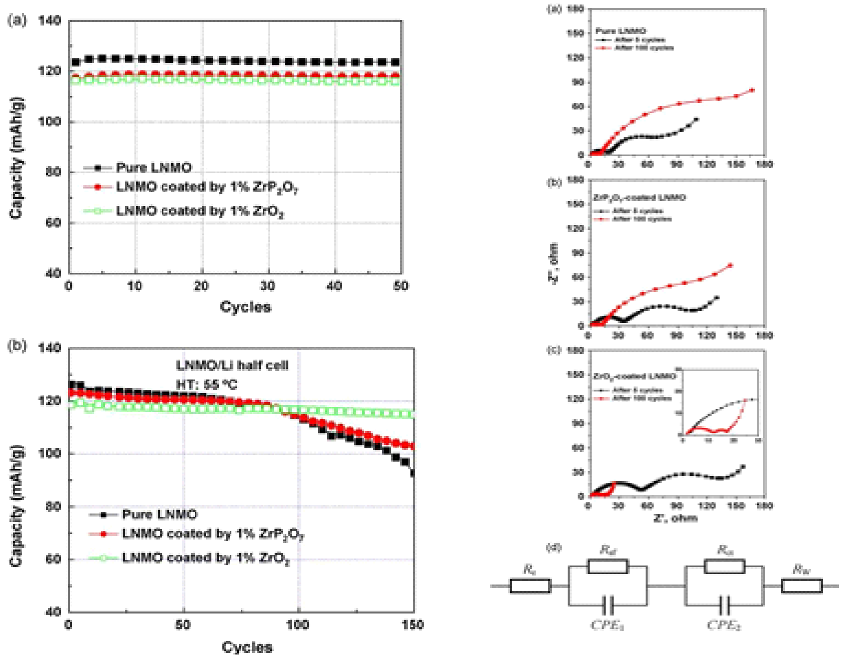

Fig 2.33. Left: Cycle stability of pristine LNMO, ZrP_2O_7-coated LNMO, and ZrO_2-coated LNMO at (a) room temperature and (b) high temperature (55 °C). Right: EIS results of (a) pristine LNMO, (b) ZrP_2O_7-coated LNMO, and c) ZrO_2-coated LNMO after 5 cycles and 100 cycles; (d) the corresponding equivalent circuit [91].

Bismuth oxyfluoride: BiOF

Spinel LNMO powders were coated with BiOF to improve their electrochemical performances [92] (Fig 2.34). The BiOF-coated LNMO showed a significantly improved capacity retention of 84.5% for 70 cycles at 55 °C, while the pristine exhibited a capacity retention of only 31.3% (Fig 2.35). Furthermore, the rate capability of the BiOF-coated LNMO was remarkably enhanced. The improved electrochemical performance is attributed to the BiOF nanolayer scavenging HF in the electrolyte. In addition, the decreased dissolution of transition metals with the BiOF coating was not a major factor for the enhanced battery performances. Therefore, the BiOF coating was found to have positive effects on the improvement of electrochemical properties with the 5V LNMO spinel compound.

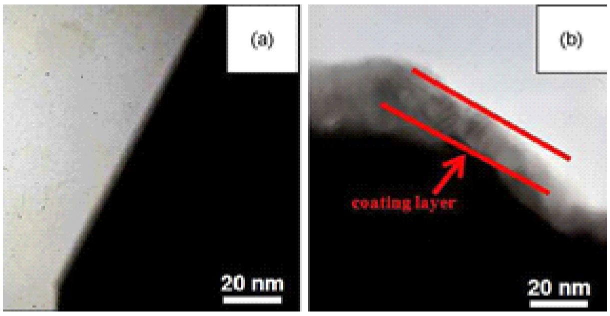

Fig 2.34. TEM bright-field images of (a) pristine LNMO (b) BiOF-coated LNMO [92].

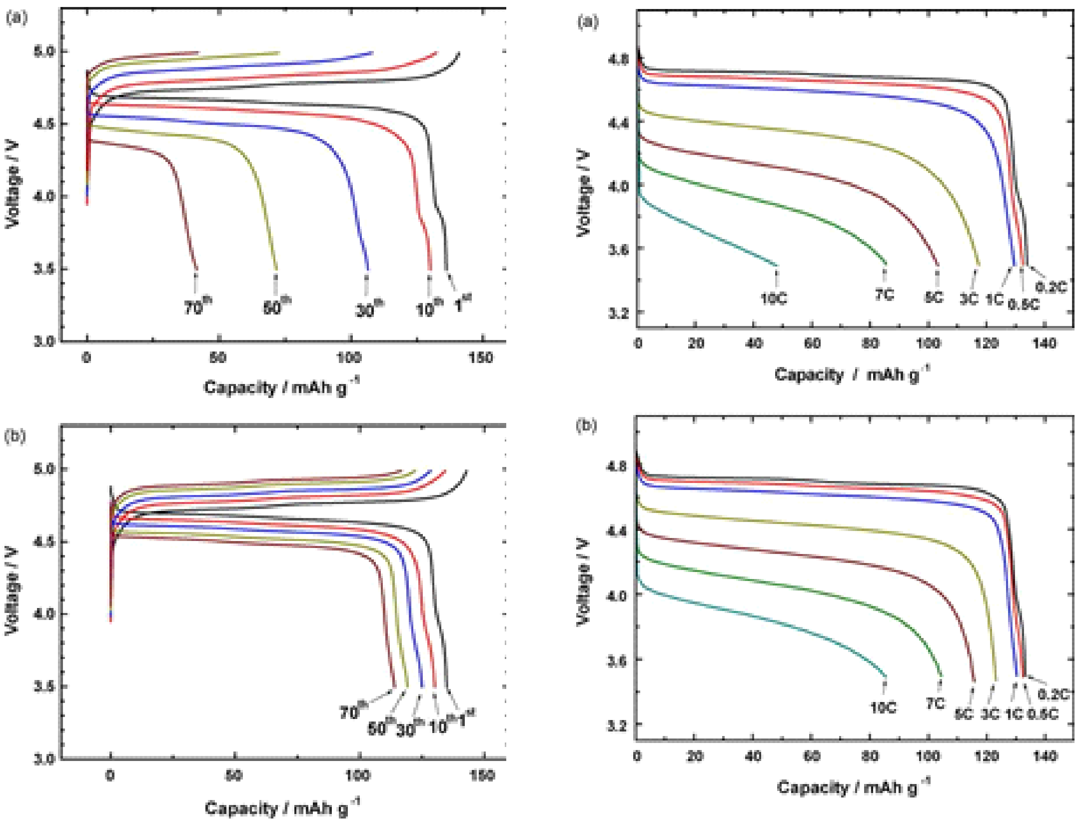

Fig 2.35 Left: Continuous charge and discharge curves of (a) Li/pristine LNMO and (b) Li/BiOF-coated LNMO cells at 55 °C. Right: Rate capabilities of (a) pristine LNMO and (b) BiOF-coated LNMO between 3.5 and 5V at 0.2C, 0.5C, 1C, 3C, 5C, 7C, 10C at 30 °C [92]

2.6.4 Non-metal oxides

Carbon coated LNMO

The LNMO powder was synthesized by a sol–gel method and fired at 850 °C in air for 6 h as in [34]. For preparing the carbon-coated sample, the predetermined sucrose (0.5, 1 and 3 wt.%, respectively, with respect to LNMO) was mixed with the as-prepared LNMO in a solvent mixture of ethanol and distilled water (4:1 in volume). Then, the mixture was completely dried at 75 °C within 3 h and heated at 350 °C for 1 h in air to obtain the modified sample. For convenience, the samples modified with 0, 0.5, 1 and 3wt.% sucrose were remarked as a, b, c and d, respectively (Fig 2.36) [81]. The impedance data were already presented in Fig 2.30.

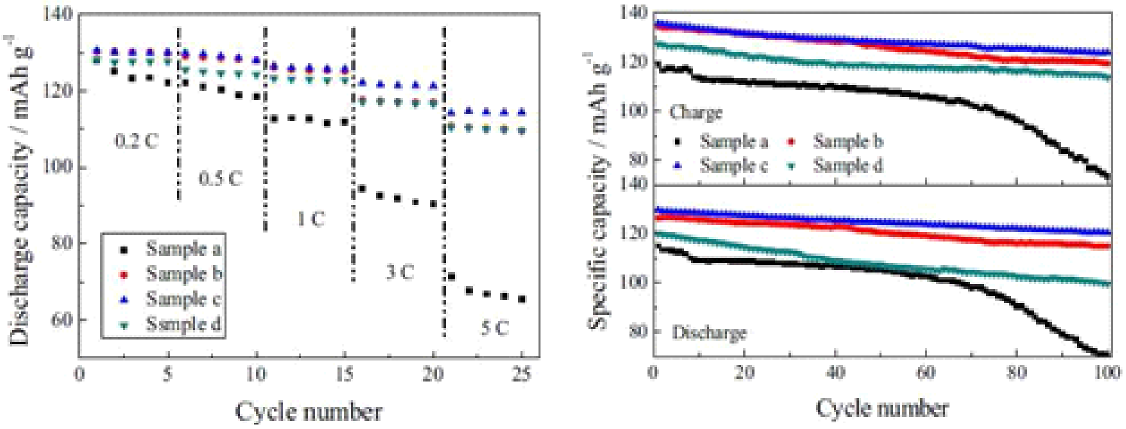

Fig 2.36. Left: Rate capabilities of the bare and carbon-coated LNMO. Right: Rate cycle comparisons of the bare and carbon-coated LNMO [81].

Polymer-metal oxides coatings

A PMMA/Zr(OBu)$_4$ composite was formed on LNMO, which is more flexible that a Zr(OBu)$_4$-derived layer [93]. The charge and discharge curves were very similar to those for bare LNMO and the surface film resistance did not increase by this Zr(OBu)$_4$/PMMA treatment. The discharge capacity was 135mAh g−1 in the first cycle. The charge and discharge efficiency increased to 80–84% in the first cycle by Zr(OBu)$_4$/PMMA treatment, and was still higher than that for an untreated electrode after 30 cycles. XPS measurements suggest that PMMA forms a composite layer with the Zr(OBu)$_4$- derived compound in the electrolyte, where PMMA did not dissolve in the electrolyte. This composite layer was lithium-ion conductive, and could be sustainable enough to suppress subsequent decomposition of the electrolyte at potentials as high as 4.7 V. Thus, the reversibility of lithium-ion insertion/extraction reactions at LNMO could be improved by forming a PMMA/Zr(OBu)$_4$ composite on LNMO. Attempts of making an SiO$_2$/PMMA was not successful, as this layer dissolved in the electrolyte used. A coating of Zr(OBu)$_4$ alone did not reveal a homogeneous coating, as several cracks were observed after cycling.

Polyimide coating

A remarkably improved cell performance and thermal stability of LNMO positive electrode active materials was obtained by exploiting an unusual concept of nanoarchitectured polyimide (PI) coating [94]. The PI coating layer (Fig 2.37), which features a highly continuous surface coverage with nanometer thickness (~10 nm) and providing adequate ion transport, successfully wrapped a large area of the LNMO surface via the thermal imidization of

4-component polyamic acid. A notable contribution of the nanostructure-tuned PI wrapping layer effectively prevent direct exposure of the LNMO surface to the liquid electrolyte that is vulnerable to electrochemical decomposition at high voltages, which indicates that the PI wrapping layer acted as a novel ion-conductive protection skin to suppress the undesired side reactions occurring on the LNMO surface. As a consequence, the PI wrapping layer played a viable role in improving the 5 V cell performance (in particular, cycle performance at 55 °C) and mitigating the interfacial exothermic reaction between the charged LNMO and the liquid electrolyte. The superior cycle performance (at 55 °C) of the PI-wrapped LNMO (PI-LNMO) was further elucidated by observing the suppressed Mn dissolution and the retarded growth of cell impedance (i.e., poorly developed SEI layer and facile charge transfer kinetics). The TOF-SIMS characterization identifying the presence of LiF deposited on the LNMO surface confirmed that the PI wrapping layer substantially hindered the formation of the byproducts that are considered a major cause for the large increase of cell impedance. The nanoarchitectured PI coating proposed in this study opens a new vista in the surface modification of spinel LNMO positive electrode active materials.

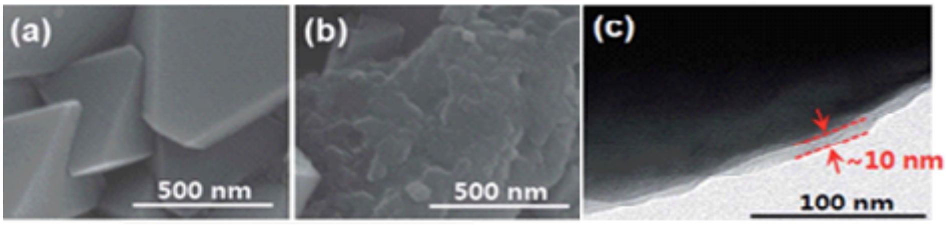

Fig 2.37. [92] FE-SEM photographs of (a) pristine LNMO and (b) PI-LNMO. (c) A TEM photograph of PI-LNMO [94].

2.7 SUMMARY AND CONCLUSIONS

The capacity fade mechanism is related to the increase in surface resistance, which is due to the development of an SEI layer, which was found to be highly resistive. Therefore, the development of the SEI layer is one of the reasons for capacity fade of LNMO during charge-discharge cycles. Furthermore, an $LiFP_6$ salt in the electrolyte is electrochemically unstable at high voltages and so oxidation of PF_6 - occurs via:

$$PF_6^- - e \rightarrow PF_6^{\bullet} \rightarrow PF_5 + F^{\bullet}$$

$$F^{\bullet} \xrightarrow{H - \text{Abstraction}} HF$$

where trace amounts of H_2O present in the electrolyte serves as the source of proton of H abstraction.

The HF formed can attack the active material surface by the following

autocatalytic corrosion reaction:

$$LiM_xO_y + HF \rightarrow LiF + M^{n+} + F^- + H_2O$$

$$H_2O + LiPF_6 \rightarrow LiF + POF_3 + 2HF$$

where M refers to transition metal. The high operating voltage of the 5 V spinel positive electrodes can accelerate the formation of HF and the increased concentration of HF can enhance the corrosion rate of the active material and the deposition rate of SEI components such as LiF and LiOH on positive electrode surface. Thus, the enhanced corrosion by HF can lead to capacity fade and a thicker SEI layer.

The SEI layer has also an impact on the electrochemical performance. The fact that the SEI layer on the bare LNMO is much thicker than that on the surface-modified sample indicates that surface modifications significantly slow down the kinetics of the electrolyte decomposition reaction at the interface between the electrolyte and the active positive electrode material. As a result, corrosion of the active positive electrode material is greatly reduced and the cycling performance is significantly improved. It is stressed that the charge-transfer reaction is one of the rate-determining steps of the lithium insertion/extraction process. The rate of charge-transfer reaction depends not only on the rate constant and electrode potential but also on the rate of Li+ ion and electron transport on to or out of the surface of the active material. The SEI layer formed with the $LiFP_6$ electrolyte solution is reported to be less conductive because the major SEI component LiF is highly resistive to both Li^+ ion and electron transport. Thus, the low charge transfer rate and the poor rate capability of the bare LNMO appear to originate from the thick SEI layer, and the improved charge-transfer rate and rate capability of the surface-modified samples is due to the reduction in the thickness of the SEI layer. The microstructure of the surface modification layer plays an important role in determining the electrochemical performances of the active material. For example, the AlPO4-coated LNMO shows a discrete and dense surface modification layer. This means a small portion of the active material may be directly exposed to the electrolyte. During the initial number of cycles, the SEI layer is less developed, and the uncovered surface may provide the effective sites for the charge-transfer reaction, which leads to a small charge transfer resistance and good rate capability. However, as the cycle number increases, the SEI layer is intensively developed on the uncovered surface and the thick and less conductive SEI layer increases the surface and charge transfer resistances and thereby degrades the rate capability. Also, the slow kinetics of the Li+ ion diffusion through this AlPO4 modification layer may also contribute to the poor rate capability after a long cycling time. Because the uncovered surface is only a small portion, the capacity decay is not serious during cycling. In contrast to these coatings, when the surface modification layers are all continuous and more porous, e.g. in the case of Al_2O_3, ZnO, and Bi_2O_3, the layer can effectively protect the active material from "electrolyte attack" and suppress the fast development of the SEI layer. Besides, the thin SEI layer results in smaller surface resistances and charge transfer resistances, hence, rendering good rate capability even after multiple cycles. Although the surface-modified samples exhibit better electrochemical performance than the bare sample, they also differ significantly in their performance depending on the coating material. Among them, both ZnO and $AlPO_4$ remain unchanged during the annealing and electrochemical cycling processes, but are neither good lithium-ion conductors nor good electronic conductors. Therefore, both the ZnO and $AlPO_4$ coating layers act only as an inert protection shell between the active positive electrode surface and the electrolyte. On the other hand, Al_2O_3, for instance, reacts with the surface of LNMO during the annealing process and forms $LiAlO_2$ that exhibit good lithium-ion conductivity, hence acting as both a protection shell and as a fast lithium-ion diffusion channel, rendering both excellent cycling performance and good rate capability. Similarly, the reported Bi_2O_3 is reduced on the positive electrode surface during electrochemical cycling to metallic Bi, which is an electronic conductor, and "Bi_2O_3" acts both as a protection shell and as a fast electron transfer channel, rendering both excellent rate capability and good cycling performance. However, the cycling performance of the Bi_2O_3- coated LNMO is not as good as that of the Al_2O_3-coated sample, which might be due to the micro-structural changes of the Bi_2O_3 modification layer during the reduction process.

Hence:

· LNMO having the Fd-3m space group is preferred over the $P4_332$ space group. Several methods have been applied to synthesise this structure, but typically a annealing temperature above 730 °C is required. However, this temperature depends a little on the precursors used, as this determines the pre-annealed material.

· Ordered LNMO spinel (space group $P4_332$) with particle size in the order of several microns shows high rate capability and excellent cyclability – capacity of 78 mAh/g at a 167C.The high rate capability observed for the $P4_332$ could also account for the Fd-3m structure.

·high operating voltage plays a crucial factor as it determines the surface area that is exposed to the electrolyte. Due to the high operating voltage there is parasitic reaction during work, which mainly appears as dissolution of the material, e.g. manganese.

· Doping of LNMO with particular Cr showed a significant improvement of the structural integrity.

· Coating LNMO is relevant in order to suppress the dissolution, but also to enhance the charge carrier transfer though the surface. It is noticed that some dopant ions initiate surface segregation, creating already a protective layer and enhanced charge transfer. Nevertheless, coating of pristine LNMO also showed improved performance. Here, ZnO, ZrO_2, Bi_2O_3, and SiO_2 have shown to be sufficient. Other coatings such as $La_{0.7}Sr_{0.3}MnO_3$ and various polymers (e.g. polyimide) improved the charge carrier transfer.

References :

1. Amatucci, G. and J.M. Tarascon, *Optimization of insertion compounds such as LiMn2O4 for Li-ion batteries.* Journal of the Electrochemical Society, 2002. **149**(12): p. K31-K46.

2. Lu, D.S., et al., *Study on Electrode Kinetics of Li+ Insertion in LixMn2O4 (0 <= x <= 1) by Electrochemical Impedance Spectroscopy.* Journal of Physical Chemistry C, 2007. **111**(32): p. 12067-12074.

3. Hasegawa, A., K. Yoshizawa, and T. Yamabe, *Total overlap population analysis for cyclic capacity of metal-substituted-spinel lithium manganate LiMn2O4 for positive electrode material of rechargeable lithium-ion battery.* Journal of the Electrochemical Society, 2001. **148**(7): p. A701-A705.

4. Yi, T.F., et al., *A review of recent developments in the surface modification of LiMn2O4 as positive electrode material of power lithium-ion battery.* Ionics, 2009. **15**(6): p. 779-784.

5. Kawai, H., et al., *High-voltage lithium positive electrode materials.* Journal of Power Sources, 1999. **81**: p. 67-72.

6. Ohzuku, T., S. Takeda, and M. Iwanaga, *Solid-state redox potentials for Li[Me1/2Mn3/2]O-4 (Me : 3d-transition metal) having spinel-framework structures: a series of 5 volt materials for advanced lithium-ion batteries.* Journal of Power Sources, 1999. **81**: p. 90-94.

7. Amine, K., et al., *A new three-volt spinel Li1+xMn1.5Ni0.5O4 for secondary lithium batteries.* Journal of the Electrochemical Society, 1996. **143**(5): p. 1607-1613.

8. Yi, T.F., Y.R. Zhu, and R.S. Zhu, *Density functional theory study of lithium intercalation for 5 V LiNi0.5Mn1.5O4 positive electrode materials.* Solid State Ionics, 2008. **179**(38): p. 2132-2136.

9. Ariyoshi, K., et al., *Topotactic two-phase reactions of Li[Ni1/2Mn3/2]O-4 (P4(3)32) in nonaqueous lithium cells.* Journal of the Electrochemical Society, 2004. **151**(2): p. A296-A303.

10. Kim, J.H., et al., *Comparative study of LiNi0.5Mn1.5O4-delta and LiNi0.5Mn1.5O4 positive electrodes having two crystallographic structures: Fd(3)over-barm and P4(3)32.* Chemistry of Materials, 2004. **16**(5): p. 906-914.

11. Julien, C.M., et al., *Lattice vibrations of materials for lithium rechargeable batteries. VI: Ordered spinels.* Materials Science and Engineering B-Solid State Materials for Advanced Technology, 2006. **130**(1-3): p. 41-48.

12. Zhong, Q.M., et al., *Synthesis and electrochemistry of LiNixMn2-xO4.* Journal of the Electrochemical Society, 1997. **144**(1): p. 205-213.

13. Alcantara, R., et al., *Optimizing preparation conditions for 5 V electrode performance, and structural changes in Li1-xNi0.5Mn1.5O4 spinel.* Electrochimica Acta, 2002. **47**(11): p. 1829-1835.

14. Sun, Y.K., et al., *Synthesis and electrochemical properties of ZnO-coated LiNi0.5Mn1.5O4 spinel as 5 V positive electrode material for lithium secondary batteries (vol 5, pg A99 2002).* Electrochemical and Solid State Letters, 2002. **5**(9): p. L1-L1.

15. Wu, H.M., et al., *Electrochemical and ex situ XRD studies of a LiMn1.5Ni0.5O4 high-voltage positive electrode material.* Electrochimica Acta, 2005. **50**(20): p. 4104-4108.

16. Idemoto, Y., H. Narai, and N. Koura, *Crystal structure and positive electrode performance dependence on oxygen content of LiMn1.5Ni0.5O4 as a positive electrode material for secondary lithium batteries.* Journal of Power Sources, 2003. **119**: p. 125-129.

17. Park, S.H., et al., *Comparative study of different crystallographic structure of LiNi0.5Mn1.5O4-delta positive electrodes with wide operation voltage (2.0-5.0 V).* Electrochimica Acta, 2007. **52**(25): p. 7226-7230.

18. Alcantara, R., et al., *Changes in the local structure of LiMgyNi0.5-yMn1.5O4 electrode materials during lithium extraction.* Chemistry of Materials, 2004. **16**(8): p. 1573-1579.

19. Chen, C.H., et al., *Studies of Mg-substituted Li4-xMgxTi5O12 spinel electrodes (0 <= x <= 1) for lithium batteries.* Journal of the Electrochemical Society, 2001. **148**(1): p. A102-A104.

20. Wagemaker, M., et al., *Extensive migration of Ni and Mn by lithiation of ordered LiMg0.1Ni0.4Mn1.5O4 spinel.* Journal of the American Chemical Society, 2004. **126**(41): p. 13526-13533.

21. Oh, S.H., et al., *Structural and electrochemical investigations on the LiNi0.5-xMn1.5-yMx+yO4 (M = Cr, Al, Zr) compound for 5 V positive electrode material.* Journal of Alloys and Compounds, 2009. **469**(1-2): p. 244-250.

22. Julien, C.M. and M. Massot, *Lattice vibrations of materials for lithium rechargeable batteries I. Lithium manganese oxide spinel.* Materials Science and Engineering B-Solid State Materials for Advanced Technology, 2003. **97**(3): p. 217-230.

23. Feng, X.Y., et al., *Synthesis of LiNi0.5Mn1.5O4 by solid-state reaction with improved electrochemical performance.* Journal of Alloys and Compounds, 2011. **509**(8): p. 3623-3626.

24. Arunkumar, T.A. and A. Manthiram, *Influence of chromium doping on the electrochemical performance of the 5 V spinel positive electrode LiMn1.5Ni0.5O4.* Electrochimica Acta, 2005. **50**(28): p. 5568-5572.

25. Song, J., et al., *Role of Oxygen Vacancies on the Performance of Li[Ni0.5-xMn1.5+x]O-4 (x=0, 0.05, and 0.08) Spinel Positive electrodes for Lithium-Ion Batteries.* Chemistry of Materials, 2012. **24**(15): p. 3101-3109.

26. Park, S.B., et al., *Electrochemical properties of LiNi0.5Mn1.5O4 positive electrode after Cr doping.* Journal of Power Sources, 2006. **159**(1): p. 679-684.

27. Jin, Y.C., C.Y. Lin, and J.G. Duh, *Improving rate capability of high potential LiNi0.5Mn1.5O4-x positive electrode materials via increasing oxygen non-stoichiometries.* Electrochimica Acta, 2012. **69**: p. 45-50.

28. Hao, X.G., M.H. Austin, and B.M. Bartlett, *Two-step hydrothermal synthesis of submicron Li1+xNi0.5Mn1.5O4-delta for lithium-ion battery positive electrodes (x=0.02, delta=0.12).* Dalton Transactions, 2012. **41**(26): p. 8067-8076.

29. Cabana, J., et al., *Composition-Structure Relationships in the Li-Ion Battery Electrode Material LiNi0.5Mn1.5O4.* Chemistry of Materials, 2012. **24**(15): p. 2952-2964.

30. Shu, J., et al., *Comparison of electronic property and structural stability of LiMn2O4 and LiNi0.5Mn1.5O4 as positive electrode materials for lithium-ion batteries.* Computational Materials Science, 2010. **50**(2): p. 776-779.

31. Kim, J.H., S.T. Myung, and Y.K. Sun, *Molten salt synthesis of LiNi0.5Mn1.5O4 spinel for 5 V class positive electrode material of Li-ion secondary battery.* Electrochimica Acta, 2004. **49**(2): p. 219-227.

32. Lee, E.S., et al., *Influence of Cation Ordering and Lattice Distortion on the Charge-Discharge Behavior of LiMn1.5Ni0.5O4 Spinel between 5.0 and 2.0 V.* Chemistry of Materials, 2012. **24**(18): p. 3610-3620.

33. Wang, L.P., et al., *A comparative study of Fd-3m and P4(3)32 "LiNi0.5Mn1.5O4".* Solid State Ionics, 2011. **193**(1): p. 32-38.

34. Yang, T.Y., et al., *The influence of holding time on the performance of LiNi0.5Mn1.5O4 positive electrode for lithium ion battery.* Journal of Alloys and Compounds, 2010. **502**(1): p. 215-219.

35. Kunduraci, M., J.F. Al-Sharab, and G.G. Amatucci, *High-power nanostructured LiMn2-xNixO4 high-voltage lithium-ion battery electrode materials: Electrochemical impact of electronic conductivity and morphology.* Chemistry of Materials, 2006. **18**(15): p. 3585-3592.

36. Kim, J.H., et al., *Effect of Ti substitution for Mn on the structure of LiNi0.5Mn1.5-xTixO4 and their electrochemical properties as lithium insertion material.* Journal of the Electrochemical Society, 2004. **151**(11): p. A1911-A1918.

37. Lee, Y.S., et al., *Preparation and characterization of nano-crystalline LiNi0.5Mn1.5O4 for 5 V positive electrode material by composite carbonate process.* Electrochemistry Communications, 2002. **4**(12): p. 989-994.

38. Ma, X.H., B. Kang, and G. Ceder, *High Rate Micron-Sized Ordered LiNi0.5Mn1.5O4.* Journal of the Electrochemical Society, 2010. **157**(8): p. A925-A931.

39. Ooms, F.G.B., et al., *High-voltage LiMg delta Ni0.5-delta Mn1.5O4 spinels for Li-ion batteries.* Solid State Ionics, 2002. **152**: p. 143-153.

40. Locati, C., et al., *Mg-doped LiNi0.5Mn1.5O4 spinel for positive electrode materials.* Journal of Power Sources, 2007. **174**(2): p. 847-851.

41. Lafont, U., et al., *Nanosized high voltage positive electrode material LiMg0.05Ni0.45Mn1.5O4: Structural, electrochemical and in situ investigation.* Journal of Power Sources, 2009. **189**(1): p. 179-184.

42. Zhang, N.Q., et al., *A facile method to prepare hybrid LiNi0.5Mn1.5O4/C with enhanced rate performance.* Journal of Alloys and Compounds, 2011. **509**(9): p. 3783-3786.

43. Vicente, C.P., J.M. Lloris, and J.L. Tirado, *Understanding the voltage profile of Li insertion into LiNi0.5-yFeyMn1.5O4 in Li cells.* Electrochimica Acta, 2004. **49**(12): p. 1963-1967.

44. Liu, J. and A. Manthiram, *Understanding the Improved Electrochemical Performances of Fe-Substituted 5 V Spinel Positive electrode LiMn1.5Ni0.5O4.* Journal of Physical Chemistry C, 2009. **113**(33): p. 15073-15079.

45. Shin, D.W., et al., *Role of Cation Ordering and Surface Segregation in High-Voltage Spinel LiMn1.5Ni0.5-xMxO4 (M = Cr, Fe, and Ga) Positive electrodes for Lithium-Ion Batteries.* Chemistry of Materials, 2012. **24**(19): p. 3720-3731.

46. Alcantara, R., et al., *Synergistic effects of double substitution in LiNi0.5-yFeyMn1.5O4 spinel as 5 V positive electrode materials.* Journal of the Electrochemical Society, 2005. **152**(1): p. A13-A18.

47. Fey, G.T.K., C.Z. Lu, and T.P. Kumar, *Preparation and electrochemical properties of high-voltage positive electrode materials, LiMyNi0.5-yMn1.5O4 (M = Fe, Cu, Al, Mg; y=0.0-0.4).* Journal of Power Sources, 2003. **115**(2): p. 332-345.

48. Leon, B., et al., *Structure and lithium extraction mechanism in LiNi0.5Mn1.5O4 after double substitution with iron and titanium.* Electrochemical and Solid State Letters, 2006. **9**(2): p. A96-A100.

49. Zhong, G.B., et al., *Effects of Al substitution for Ni and Mn on the electrochemical properties of LiNi0.5Mn1.5O4.* Electrochimica Acta, 2011. **56**(18): p. 6554-6561.

50. Robertson, A.D., S.H. Lu, and W.F. Howard, *M3+-modified LiMn2O4 spinel intercalation positive electrodes .2. Electrochemical stabilization by Cr3+.* Journal of the Electrochemical Society, 1997. **144**(10): p. 3505-3512.

51. Sigala, C., et al., *The Cr-substituted spinel Mn oxides LiCryMn2-yO4 (0<=y<=1): Rietveld analysis of the structure modifications induced by the electrochemical lithium deintercalation.* Journal of Solid State Chemistry, 1997. **132**(2): p. 372-381.

52. Liu, G.Q., et al., *Synthesis and electrochemical performances of spinel LiCr0.1Ni0.4Mn1.5O4 compound.* Materials Research Bulletin, 2007. **42**(11): p. 1955-1961.

53. Liu, G.Q., et al., *Rate capability of spinel LiCr0.1Ni0.4Mn1.5O4.* Journal of Alloys and Compounds, 2010. **501**(2): p. 233-235.

54. Yi, T.F., et al., *Comparison of structure and electrochemical properties for 5 V LiNi0.5Mn1.5O4 and LiNi0.4Cr0.2Mn1.4O4 positive electrode materials.* Journal of Solid State Electrochemistry, 2009. **13**(6): p. 913-919.

55. Aklalouch, M., et al., *Sub-micrometric LiCr0.2Ni0.4Mn1.4O4 spinel as 5 V-positive electrode material exhibiting huge rate capability at 25 and 55 degrees C.* Electrochemistry Communications, 2010. **12**(4): p. 548-552.

56. Aklalouch, M., et al., *Chromium doping as a new approach to improve the cycling performance at high temperature of 5 VLiNi0.5Mn1.5O4-based positive electrode.* Journal of Power Sources, 2008. **185**(1): p. 501-511.

57. Xiao, J., et al., *High-Performance LiNi0.5Mn1.5O4 Spinel Controlled by Mn3+Concentration and Site Disorder.* Advanced Materials, 2012. **24**(16): p. 2109-2116.

58. Oh, S.W., et al., *Effects of Co doping on Li[Ni0.5CoxMn1.5-x]O-4 spinel materials for 5 V lithium secondary batteries via Co-precipitation.* Journal of Power Sources, 2009. **189**(1): p. 752-756.

59. Li, D.C., et al., *Structural and electrochemical characteristics of LiNi0.5-xCo2xMn1.5-xO4 prepared by spray drying process and post-annealing in O-2.* Journal of Power Sources, 2006. **161**(2): p. 1241-1246.

60. Liu, J. and A. Manthiram, *Understanding the Improvement in the Electrochemical Properties of Surface Modified 5 V LiMn1.42Ni0.42Co0.16O4 Spinel Positive electrodes in Lithium-ion Cells.* Chemistry of Materials, 2009. **21**(8): p. 1695-1707.

61. Arunkumar, T.A. and A. Manthiram, *Influence of lattice parameter differences on the electrochemical performance of the 5 V spinel LiMn1.5-yNi0.5-zMy+zO4 (M = Li, Mg, Fe, Co, and Zn).* Electrochemical and Solid State Letters, 2005. **8**(8): p. A403-A405.

62. Noguchi, T., et al., *Effect of Bi oxide surface treatment on 5 V spinel LiNi0.5Mn1.5-xTixO4.* Journal of Power Sources, 2007. **174**(2): p. 359-365.

63. Liu, G.Q., et al., *The electrochemical properties of LiNi0.5Mn1.2Ti0.3O4 compound.* Journal of Alloys and Compounds, 2009. **484**(1-2): p. 567-569.

64. Alcantara, R., et al., *Structural and electrochemical study of new LiNi0.5TixMn1.5-xO4 spinel oxides for 5-V positive electrode materials.* Chemistry of Materials, 2003. **15**(12): p. 2376-2382.

65. Le, H.C., et al., *Synthesis, characterization and electrochemical properties of 4.8 V LiNi0.5Mn1.5O4 positive electrode material in lithium-ion batteries.* Electrochimica Acta, 2010. **55**(18): p. 5110-5116.

66. Toussain.Cj, *High-Temperature X-Ray Diffraction Study of Nio-Li20 System.* Journal of Applied Crystallography, 1971. **4**(Aug1): p. 293-&.

67. Liu, C.G., et al., *Electrochemical properties of LiNi0.5Mn1.3Ti0.2O4/Li4Ti5O12 cells.* International Journal of Minerals Metallurgy and Materials, 2012. **19**(5): p. 457-460.

68. Wang, H.L., et al., *Enhancements of rate capability and cyclic performance of spinel LiNi0.5Mn1.5O4 by trace Ru-doping.* Electrochemistry Communications, 2009. **11**(7): p. 1539-1542.

69. Oh, S.W., et al., *Improvement of electrochemical properties of LiNi0.5Mn1.5O4 spinel material by fluorine substitution.* Journal of Power Sources, 2006. **157**(1): p. 464-470.

70. Yi, T.F., et al., *High rate micron-sized niobium-doped LiMn1.5Ni0.5O4 as ultra high power positive-electrode material for lithium-ion batteries.* Journal of Power Sources, 2012. **211**: p. 59-65.

71. Kim, G.H., et al., *Improvement of high-voltage cycling behavior of surface-modified Li[Ni1/3Co1/3Mn1/3]O-2 positive electrodes by fluorine substitution for Li-ion batteries.* Journal of the Electrochemical Society, 2005. **152**(9): p. A1707-A1713.

72. Xu, X.X., et al., *LiNi0.5Mn1.5O3.975F0.05 as novel 5 V positive electrode material.* Journal of Power Sources, 2007. **174**(2): p. 1113-1116.

73. Du, G.D., et al., *Fluorine-doped LiNi(0.5)Mn(1.5)O(4) for 5 V positive electrode materials of lithium-ion battery.* Materials Research Bulletin, 2008. **43**(12): p. 3607-3613.

74. Sun, Y.K., et al., *Effect of sulfur and nickel doping on morphology and electrochemical performance of LiNi0.5Mn1.5O4-xSx spinel material in 3-V region.* Journal of Power Sources, 2006. **161**(1): p. 19-26.

75. Sha, O., et al., *The multi-substituted LiNi0.475Al0.01Cr0.04Mn1.475O3.95F0.05 positive electrode material with excellent rate capability and cycle life.* Electrochimica Acta, 2012. **77**: p. 250-255.

76. Fang, X., et al., *Electrochemical properties of nano- and micro-sized LiNi0.5Mn1.5O4 synthesized via thermal decomposition of a ternary eutectic Li-Ni-Mn acetate.* Electrochimica Acta, 2010. **55**(3): p. 832-837.

77. Mao, J., K.H. Dai, and Y.C. Zhai, *Electrochemical studies of spinel LiNi0.5Mn1.5O4 positive electrodes with different particle morphologies.* Electrochimica Acta, 2012. **63**: p. 381-390.

78. Aurbach, D., et al., *Studies of cycling behavior, ageing, and interfacial reactions of LiNi0.5Mn1.5O4 and carbon electrodes for lithium-ion 5-V cells.* Journal of Power Sources, 2006. **162**(2): p. 780-789.

79. Duncan, H., Y. Abu-Lebdeh, and I.J. Davidson, *Study of the Positive electrode-Electrolyte Interface of LiMn1.5Ni0.5O4 Synthesized by a Sol-Gel Method for Li-Ion Batteries.* Journal of the Electrochemical Society, 2010. **157**(4): p. A528-A535.

80. Mun, J., et al., *Surface Film Formation on LiNi0.5Mn1.5O4 Electrode in an Ionic Liquid Solvent at Elevated Temperature.* Journal of the Electrochemical Society, 2011. **158**(5): p. A453-A457.

81. Yang, T.Y., et al., *Enhanced rate performance of carbon-coated LiNi0.5Mn1.5O4 positive electrode material for lithium ion batteries.* Electrochimica Acta, 2011. **56**(11): p. 4058-4064.

82. Manthiram, A., K. Chemelewski, and E.S. Lee, *A perspective on the high-voltage LiMn1.5Ni0.5O4 spinel positive electrode for lithium-ion batteries.* Energy & Environmental Science, 2014. **7**(4): p. 1339-1350.

83. Wang, L.P., H. Li, and X.J. Huang, *Electrochemical properties and interfacial reactions of LiNi0.5Mn1.5O4-delta nanorods.* Progress in Natural Science-Materials International, 2012. **22**(3): p. 207-212.

84. Sun, Y.K., C.S. Yoon, and I.H. Oh, *Surface structural change of ZnO-coated LiNi0.5Mn1.5O4 spinel as 5 V positive electrode materials at elevated temperatures.* Electrochimica Acta, 2003. **48**(5): p. 503-506.

85. Brutti, S., et al., *Mitigation of the irreversible capacity and electrolyte decomposition in a LiNi0.5Mn1.5O4/nano-TiO2 Li-ion battery.* Journal of Power Sources, 2011. **196**(22): p. 9792-9799.

86. Arrebola, J.C., et al., *Re-examining the effect of ZnO on nanosized 5 V LiNi0.5Mn1.5O4 spinel: An effective procedure for enhancing its rate capability at room and high temperatures.* Journal of Power Sources, 2010. **195**(13): p. 4278-4284.

87. Baggetto, L., et al., *Fabrication and characterization of Li-Mn-Ni-O sputtered thin film high voltage positive electrodes for Li-ion batteries.* Journal of Power Sources, 2012. **211**: p. 108-118.

88. Liu, J. and A. Manthiram, *Kinetics Study of the 5 V Spinel Positive electrode LiMn(1.5)Ni(0.5)O(4) Before and After Surface Modifications.* Journal of the Electrochemical Society, 2009. **156**(11): p. A833-A838.

89. Fan, Y.K., et al., *Effects of the nanostructured SiO2 coating on the performance of LiNi0.5Mn1.5O4 positive electrode materials for high-voltage Li-ion batteries.* Electrochimica Acta, 2007. **52**(11): p. 3870-3875.

90. Zhao, G.Y., et al., *Enhanced rate and high-temperature performance of La0.7Sr0.3MnO3-coated LiNi0.5Mn1.5O4 positive electrode materials for lithium ion battery.* Journal of Power Sources, 2012. **215**: p. 63-68.

91. Wu, H.M., et al., *Surface modification of LiNi0.5Mn1.5O4 by ZrP2O7 and ZrO2 for lithium-ion batteries.* Journal of Power Sources, 2010. **195**(9): p. 2909-2913.

92. Kang, H.B., et al., *Improved electrochemical properties of BiOF-coated 5 V spinel Li[Ni(0.5)Mni(1.5)]O-4 for rechargeable lithium batteries.* Journal of Power Sources, 2010. **195**(7): p. 2023-2028.

93. Doi, T., et al., *Surface modification of LiNi1/2Mn3/2O4 thin-films by zirconium alkoxide/PMMA composites and their effects on electrochemical properties.* Journal of Power Sources, 2008. **185**(1): p. 473-479.

94. Cho, J.H., et al., *A polymer electrolyte-skinned active material strategy toward high-voltage lithium ion batteries: a polyimide-coated LiNi0.5Mn1.5O4 spinel positive electrode material case.* Energy & Environmental Science, 2012. **5**(5): p. 7124-7131.

Chapter 3 : In-situ X-Ray Absorption Spectroscopy of Cr doped and Cr coated $LiNi_{0.5}Mn_{1.5}O_4$

Abstract

The behaviour of modified $LiNi_{0.5}Mn_{1.5}O_4$– doped with chromium and coated with chromium oxide has been analysed during insertion and extraction of lithium by *in situ* X-Ray Absorption Spectroscopy (XAS) in order to observe the Cr valence and Cr environment in the structure. Several coating thicknesses are investigated. It was found that, in all cases, Cr remains in a valence state of +3 for both the doped and coated samples. The valence does not change upon cycling, indicating that Cr^{3+} is not actively involved in the insertion and extraction process. Nevertheless, according to literature, it improves the power performance of the material by enhancing the charge carrier migration. In $LiNi_{0.42}Cr_{0.08}Mn_{1.5}O_4$, Cr^{3+} resides in an octahedral site coordinated to six oxygen at 1.98 Å and six manganese at 2.99 Å in good agreement with similar compounds from the literature. For the surface coatings, chromium in the coating layer adopts the spinel type structure of the underlying lattice rather than the typical corundum structure of Cr_2O_3. This indicates that the surface coating has good contact with the underlying LMNO material and might either be epitaxial or even might penetrate into the underlying material.

3.1 Introduction

Today, Li-ion batteries provide the highest capacity among the various available battery systems. Nevertheless, there is still a need to further increase the capacity, and one way this can be achieved is to use a high voltage cathode material in order to increase the overall cell voltage.

Spinel-type lithium manganese oxide ($LiMn_2O_4$), as a cathode material for lithium-ion batteries, has attracted much attention due to its low cost, low toxicity, and relatively high energy density. However, $LiMn_2O_4$ in the 4-V region suffers from a poor cycling behaviour. It is well known that its electrochemical performance can be improved by doping. The high-voltage plateau is mainly present in spinels where the B-site – often conventionally indicated by square brackets – contains a combination of Mn and other transition metals, M, giving $Li[M_xMn_{2-x}]O_4$, where M = Cr, Fe, Co, Ni, or Cu and x is close to the maximum value x = 0.5 [1]. In this respect, LNMO has been extensively studied as a cathode material for lithium ion batteries during the past decade due to its improved cycling behaviour compared to the undoped $LiMn_2O_4$ spinel [2]. The high operating potential and three dimensional lithium-ion diffusion paths in the spinel lattice has led to even more attention. Lithium nickel manganese spinel ($LiNi_{0.5}Mn_{1.5}O_4$, referred to as LNMO) presents a high potential of 4.9 V versus metallic lithium, compared to the 3.7 V (vs Li^+/Li^0) for $LiCoO_2$, which is one of the state-of-the-art cathode materials in today's Li ion batteries. Lithium ion batteries with LNMO-based positive electrodes are expected to provide high power/energy density for electric vehicles (EVs), hybrid electric vehicles (HEVs) and large energy storage systems.

LNMO has two different crystal structures of P_{4332} and $F_{d\text{-}3m}$ [3], depending on the oxygen content in the lattice as well as the degree of ordering of the Ni and Mn ions. Besides the 4.9V plateau, the spinel is also able to accept lithium ions at the 3V plateau similar to the $LiMn_2O_4$ spinel [4]. This part will, however, not be addressed in the current discussion. The $F_{d\text{-}3m}$ structure of LNMO exhibits the better electrochemical performances than that with the P_{4332} structure [3]. Besides, it is difficult to synthesize pure stoichiometric LNMO because an impurity phase $Li_yNi_{1-y}O$ tends to be formed during the high temperature synthesis [5]. Another disadvantage of this material for applications is the fast capacity fading at elevated temperatures [5], which has been linked to the poor compatibility with the electrolytes that are commonly used. In order to improve the electrochemical performance the material needs to be stabilized. This can be achieved by various modification methods, such as lattice doping and surface coating [2]. Partial substitutions of Mn and (or) Ni in LNMO with other cations have been investigated [6]. Electrochemical testing under high rates, for both ordered and disordered structures of this material, has been studied for nano- and micron-sized particles [1,2]. It is nevertheless stressed that ion or electron transport in the particle is not the rate-limiting process; instead the performance of the material is mainly obstructed by the charge transfer properties of either electrons or Li-ions through the interface or interphase. Hence, the surface plays a crucial role in the charge transfer. In this research we studied the effect of doping LNMO with chromium, by replacing nickel, or by coating it with a chromium oxide.

Chromium oxide has been widely studied due to its importance in industrial applications. This includes coating of materials for high temperature uses, wear resistance for tribological applications [7] and, of particular interest for this study, in catalytic applications showing enhanced electron transfer (e.g. for methanol synthesis) [9, 10]. Moreover, it was used in battery applications where chromium oxide coating on $LiMn_2O_4$ increased the Mn^{4+} concentration at the surface and preventing thereby any direct contact between the active particles and the electrolyte, reducing the dissolution of manganese and the oxidation of the electrolyte [8]. In this study, several LNMO-based materials have been produced by means of carbon combustion synthesis and tested in cell type batteries (LNMO//$LiPF_6$ 1M// Li). The present study reports the electrochemical behaviour during charging and discharging the cell, and ***in*** *situ* monitoring via X-Ray Absorption Spectroscopy (XAS). The XAS results in the X-Ray Absorption Near Edge Spectra (XANES) monitor the change of the oxidation state of chromium. Similarly, the Extended X-ray Absorption Fine Stucture (EXAFS) follow the structural behaviour at different states of charge.

3.2 Experimental

Synthesis – LNMO and $LiCr_{0.08}Ni_{0.42}Mn_{1.5}O_4$ were synthesized via a Carbon Combustion Method (CCS) [9]. Stoichiometric quantities of Li_2CO_3, Mn_3O_4, NiO and Cr_2O_3 were mixed together with carbon black (Li:C molar ratio=4:1) and ground manually for 10 minutes prior to ball milling and then ground for 30 minutes with a planetary ball-mill (Fritsch P-0150). The mixture was first heated up to 950°C at 2ºC/min and kept there for 12 hours. In a second step, the material was forced to cool down slowly to room temperature over 48 hours (about 0.3ºC/min) in order to ensure adequate oxygen uptake.

To form the chromium oxide layer (samples Cr023 to Cr046), LNMO was immersed in an aqueous solution of various concentrations of $Cr(NO_3)_3.9H_2O$ (Sigma-Aldrich). The concentrations were chosen such that the amount of chromium to transition metal (Ni + Mn) in the solid was 0.2 to 1.7 mole% (see Table 3.1). The powders were exposed to the solution for 2 hours. The solution then was placed in a furnace at 120°C for 2 hours to allow the water to evaporate. The remaining powder was rinsed with ethanol, dried again and was finally annealed at 600ºC for 8 hours. It is stressed that there is no linear relation between the amount of Cr left in the coating and the initial Cr used in the solution.

Table 3.1 Samples with sample numbers.The calculated thickness of the final coating has been added. Samples Cr171 was only doped.Sample Cr046+ was coated then doped

Sample number	**Mole% of [Cr]/[Ni+Mn]**	**Coating thickness, nm**
Cr000	0	0
Cr023	0.23	0.45
Cr034	0.34	N/A
Cr046	0.46	1.53
Cr057	0.57	1.69
Cr171	1.71	N/A
Cr046+	0.46 + doping	7.99

Structural analysis (ICP-OES, SEM, BET, XRD) - The overall atomic compositions of the as-prepared samples were measured with Inductively Coupled Plasma Optical Emission Spectroscopy (ICP-OES). This involved dissolving 50 mg of sample in an acidic solution (4mL HCl(30%) + 2mL HNO_3(65%) + 1mL HF(40%)), in a microwave (Microwave PRO) for 30 min at 1300W.

For the characterization of the particle size and morphology, an SEM (Philips XL20) operated at 20 kV was used.

Brunauer–Emmett–Teller (BET) measurements were performed with nitrogen gas to obtain the surface area of our material.

The crystal structure was analysed with a Bruker D8 ADVANCE X-ray diffractometer using CoKα radiation (wavelength 1.789 Å). Measurements were recorded between 2θ of 5-90°.

Electrochemical measurements – In order to prepare the electrode, a ratio of 80 wt% active material (sample), 12 wt% polyvinylidene fluoride (PVDF) and 8 wt% carbon black were mixed with N-methyl-2-pyrrolidone (NMP) solvent. The slurry was uniformly cast on aluminium foil via doctor blade The cast foils were dried in an oven at 120 °C for 10 hours. From these coatings, cylindrical disks were punched out with a diameter of 1,5cm. The disks were pressed with a pressure around 1700 kg/cm^2 before drying in a vacuum oven for 12 hours.

Pouch cells were assembled in an argon-filled glove box with lithium metal disk (2.011cm^2) as the counter electrodes and polypropylene as the separator filled with commercial organic electrolyte consisting of 1M LPF_6 in 1:1 ethylene carbonate (EC) and dimethyl carbonate (DMC). Galvanostatic cycling tests were operated with a Maccor battery cycler in a potential range of 3.5V to 5V and typical currents of few mA/cm^2, resembling roughly a 1C rate.

X-Ray Absorption Spectroscopy – Data acquisition was carried out on the BM26 (DUBBLE) XAS beam line at the European Synchrotron Radiation Facility (ESRF). Spectra were collected at the Cr K-edge in fluorescence geometry at room temperature. The beam energy is tuned by a Si(111) double crystal monochromator, which was calibrated with an Cr metal foil (taken at the first point of inflexion, 5989 eV). The fluorescent X ray intensities were measured using a 9-element monolithic Ge detector [10].

The measurements were carried out at different cycle numbers at a certain state of charge (SoC) either on the charge or discharge to monitor an eventual change of oxidation state of the chromium depending on the number of charge/discharge.

In situ XANES has been recorded and data analysis was started by transforming the fluorescence data to obtain the absorbance μt as a function of X-ray energy E. The data reduction was performed on the software VIPER whereby the edge position, E_0, was identified from the inflection point on the main absorption edge [11]. Following this, it was possible to remove both the pre- and post-edge backgrounds in order to obtain the normalized absorbance μ.

The XANES spectra gives information about valence and site symmetry of the target atom – in this case Cr. The energies of the valence orbitals, and, therefore, the energy position of the edge and pre-edge features are correlated with the valence state of chromium in the sample. The edge position, which is defined by the intensity at half height of the normalized absorbance [12]. The valence state of chromium in the samples has been estimated by comparing the position of the absorbance edge with a a-Cr_2O_3, with a known valence state of 3+.

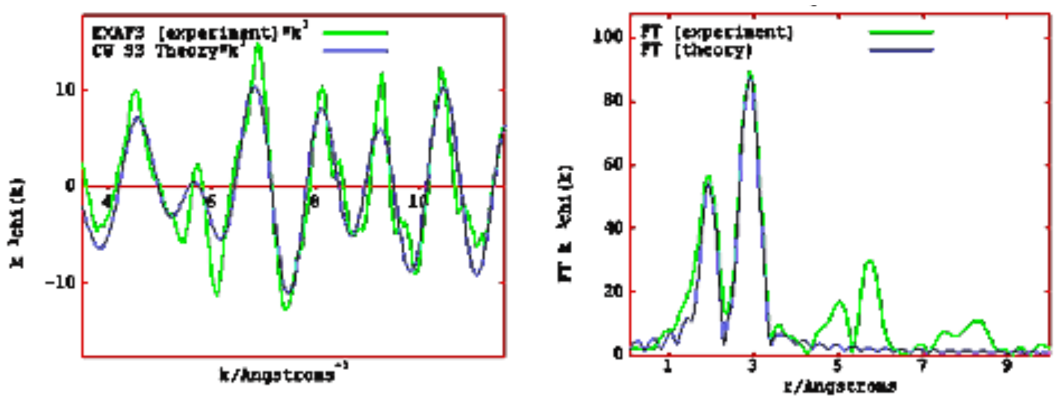

(a) **(b)**

Figure 3.1. ***a)*** *The EXAFS spectra* $\chi(k)k^3$ *and* ***b)*** *the Fourier transforms F(R) of the EXAFS spectra* $\chi(k)k^3$ *for the Cr K-edge in sample Cr171.*

A more detailed discussion on the chromium site can be based on the in-situ EXAFS measurements, which gives information about bond lengths and coordination numbers. The amplitude reduction factor (AFAC) was estimated to be 0.5 by fitting the known corundum structure of Cr_2O_3 reference sample. The EXAFS fits were done with a 3rd order k-weighting ($\chi(k)k^3$) using a range from 3 to 12 Å^{-1}, which includes the two first shells (Figure 3.1). Structural parameters where refined using a least square fitting routine in EXCURVE9.27 [K. Klementiev, B.G. Searle, A. Wander, N.M. Harrison A.J. Dent J.F.W. Mosselman J.E. Inglesfield; CCLRC Technical Report, No. DL-TR-2005-001: Warrington, UK, 2004].

3.3 Results and discussion

SEM micrographs are shown for the pristine LNMO (Figure 3.2a) and a chromium oxide coated sample (Figures 3.2b and 3.2c) at different magnifications. The picture shows clear micron-sized crystals in the order of 2 to 7 µm.

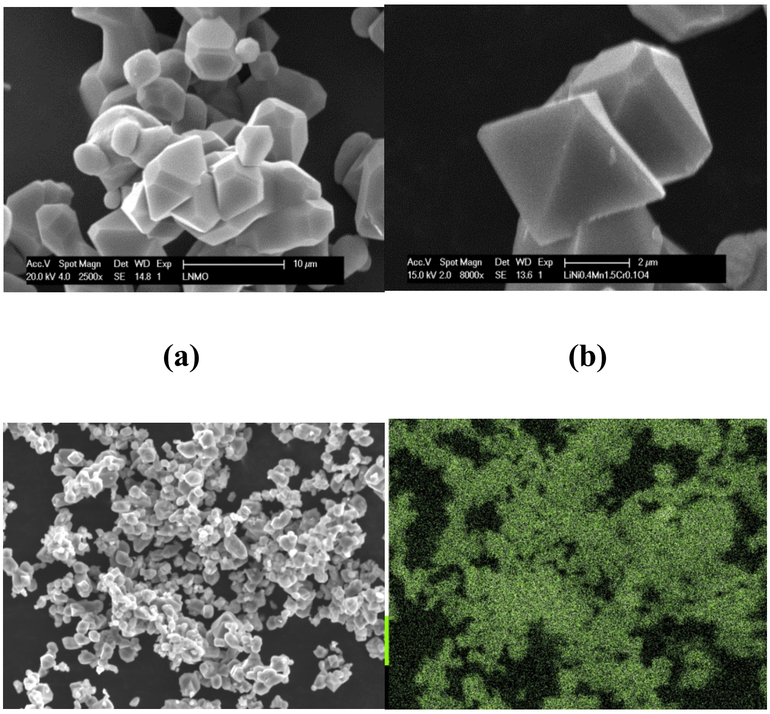

(a) **(b)**

(c) **(d)**

Figure 3.2. SEM micrographs of (a) pristine LNMO and (b), and (c) coated LNMO samples (sample Cr057), as well as (d) EDX images of the Cr-distribution of Figure 1c.

Figure 3.2d shows the distribution of chromium corresponding to the sample shown in Figure 3.2c. Clearly, the coated chromium is homogeneously distributed over the entire sample. It is stressed that this appears to be the same for all samples prepared and tested.

The BET surface area was calculated to be 0.32 m^2/g and was independent of the chromium oxide coating.

The Mn/Ni ratio and Cr content were calculated from ICP-OES analyses data. The Mn/Ni ratio agrees very well with the intended stoichiometry of 3 (1.5/0.5). The Cr content runs from 0.23mole% to 1.71mole% of the total transition metal content depending on the amount of chromium used in the beginning of the preparation. Knowing the BET surface area and an accepted density of 5.22 g/cm^3 as taken from Cr_2O_3 with the corundum structure, and the Cr/(Ni+Mn) ratio, the layer thickness has been calculated of the various chromium oxide coatings. The thickness then ranges from 0.5 to 8 nm.

The XRD patterns of the samples have been recorded for the various coated samples, and no differences can be detected between the various samples (see Figure 3.3). It could mean that the coating is either amorphous, adopts a similar structure as the LNMO, or the amount is simply too small as already calculated above. Nevertheless, the usual impurity phase of $Li_xNi_{1-x}O$ is visible. This impurity then is also responsible for a higher Mn content in the LNMO phase, which is reflected by the additional voltage plateau in the charge and discharge curve of Figure 3.4.

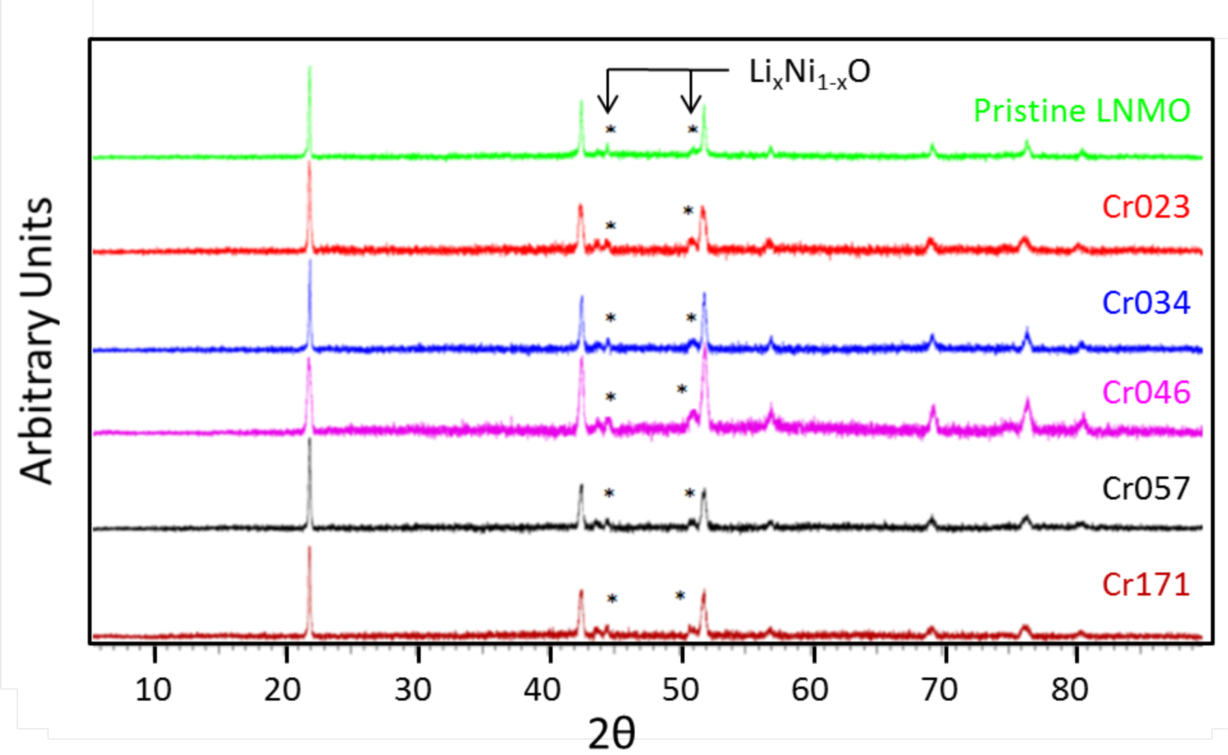

Figure 3.3. XRD pattern showing different LNMO based materials. The thickness of the samples corresponds to the values given in Table 1. The asterisk (*) indicate the positions of the impurity phase $Li_xNi_{1-x}O$. Pattern have been shifted vertically for clarity

Figures 3.4a and 3.4b present the charge and discharge profiles for the chromium oxide coated sample, Cr057, with a thickness of 1.69nm. The profile shows a clear voltage plateau at 4.1V due to the Mn^{3+}/Mn^{4+} redox couple and the standard double plateau near 4.7V associated with the redox couples Ni^{2+}/Ni^{3+} and Ni^{3+}/Ni^{4+}. Both materials were used in a pouch-cell battery for a few cycles (one cycle equals to one charge plus one discharge), depending on the desired state of charge. At a specific SoC, the charge or discharge is being stopped and after a certain relaxation time, the batteries were disconnected from the Maccor cycler and placed in the beam line of the synchrotron for XAS measurements. After the measurement, the cell was reconnected to the Maccor and charge or discharge were resumed for another few cycles.

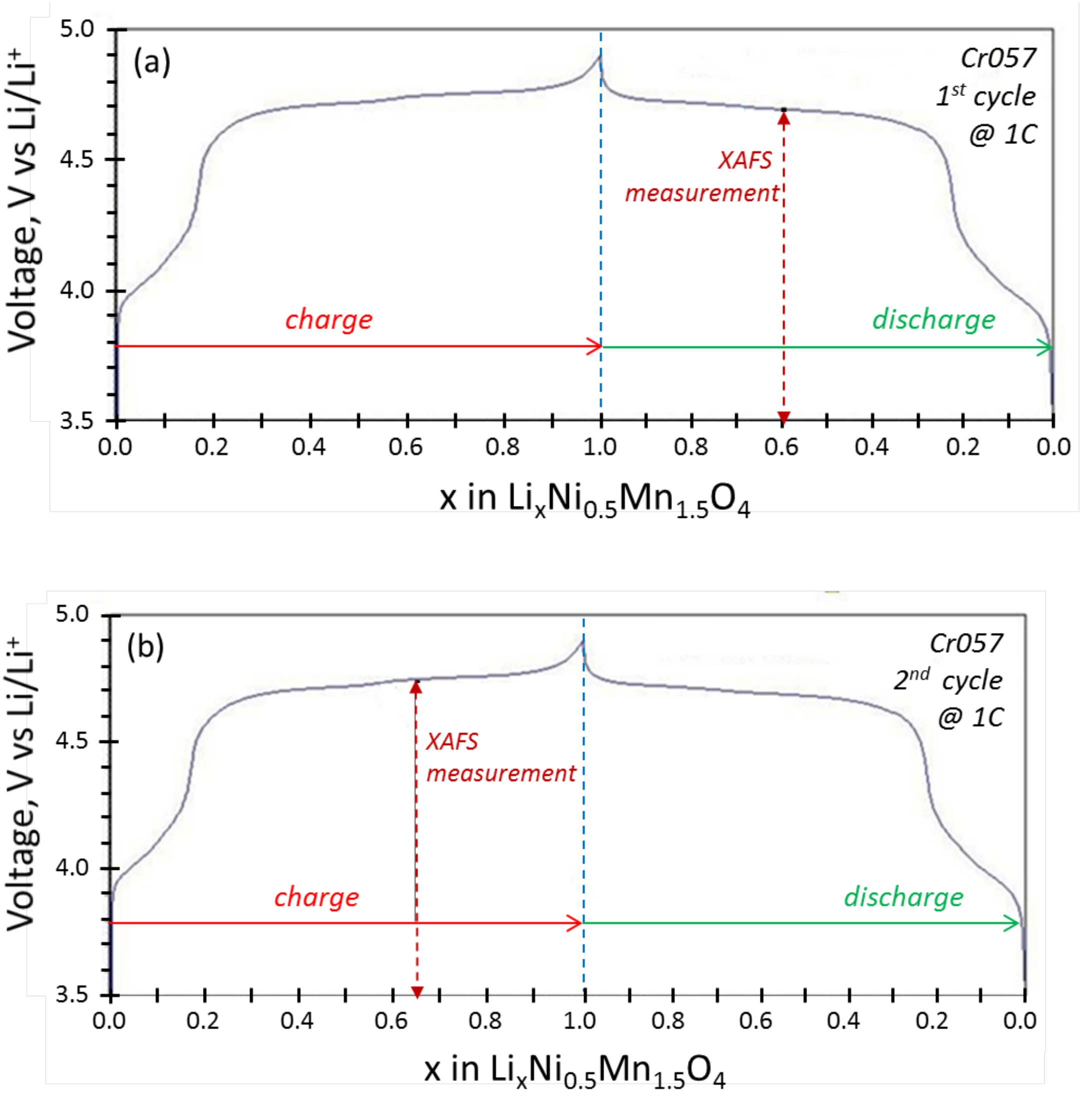

Figure 3.4. First (a) and second (b) galvanostatic charge/discharge cycle of sample Cr057 at a 1C rate. The arrows indicate the SoC at which an XAFS measurement was recorded.

Figure 3.5 shows the XANES spectra of the Cr K-edge obtained from doped $LiNi_{0.42}Cr_{0.08}Mn_{1.5}O_4$ and LNMO chromium oxide surface coated samples cycled between 3.5V and 4.9V. The doped sample was recorded as a pristine material (pellet) and after 16 cycles. The coated samples were recorded as pristine cells and after a various number of cycles.

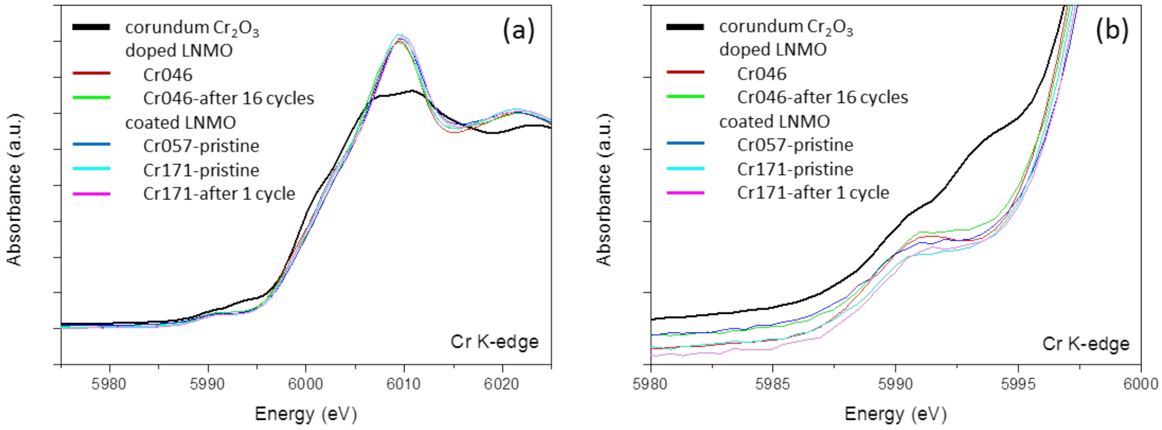

Figure 3.5: (a) Normalised Cr – K-edge profiles for the Cr_2O_3 reference sample and doped and coated LNMO and (b) magnification of (a) near the pre-edge. Note the similarity in edge position for both the reference and test samples.

The edge shape clearly indicates a difference between the Cr_2O_3 corundum and the doped as well as coated LNMO spinel samples, demonstrating a distinct difference in local structure. The Cr K-edge position remains the same for all the samples implying that there is no change in valence state. It should be noted that this agrees with studies of $Li_{1-x}Mn_{2-y}Cr_yO_4$ from Nakai *et al*. [13] whereby chromium does not change oxidation state upon cycling, instead stabilizing the spinel structure. The current result, however, is in contrast to results obtained by Ammundsen et al. [14] showing that chromium does change valence, but the results in Ammundsen et al. might be due to an increased concentration of chromium in the sample.

The minimal intensity of the pre-edge peak in the XANES spectra of both the standard Cr_2O_3 and the spinel data indicates that chromium is located at an inversion center in the structure. For instance, Cr_2O_3 forms a corundum structure where chromium occupies octahedral sites in the lattice. Octahedral symmetry is recognized by three small resonances in the pre-edge region which are assigned to transitions of 1s electrons into anti-bonding orbitals with octahedral symmetry [12]. The pre-edge region (Figure 3.5b) indicates that Cr exists in an octahedral coordination for all the samples (doped / coated / cycled / pristine). The results have been compared to studies performed by Farges et al. [18] who deduces that Cr is located in a very regular site of Al in the classical spinel $MgAl_{2-y}Cr_yO_4$. They reported three pre-edge features, but here the 1st and 3rd peaks are barely visible due to the poor statistics in this region, which is related to the extremely low concentrations of chromium. A similar pre-edge peak is reported for Cr in an octahedral site in the spinel $FeCr_2O_4$ [15].

For the EXAFS measurements (Figure 3.6a), doped and coated LNMO have been fitted with a structural model consisting of six oxygen atoms around the central chromium cation at an initial distance of 1.98 Å. This is followed by a secondary shell of six Mn at a distance of 2.91 Å. In addition, unconstrained fits give values of coordination numbers (N) close to 6. In this model the neighboring lithium atoms are disregarded due to their negligible effect on the photoelectron scattering.

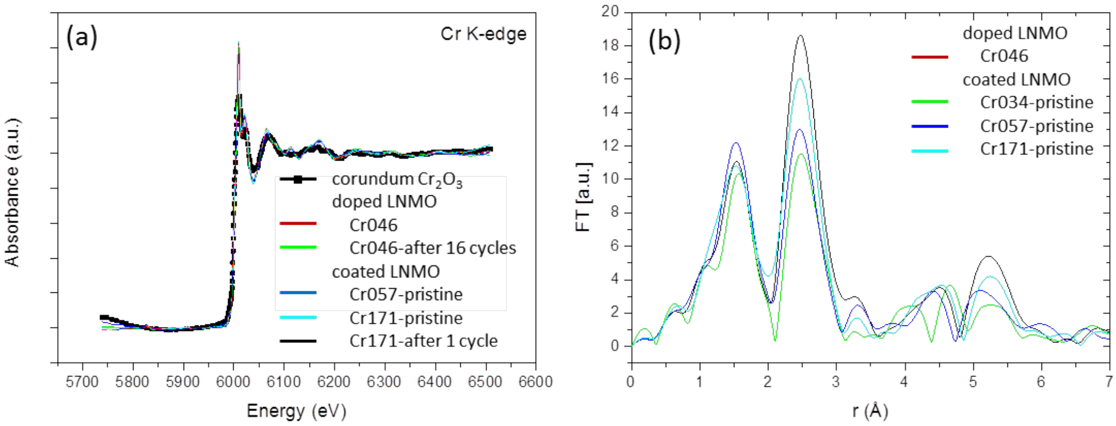

Figure 3.6. EXAFS spectra for a selected series of samples as indicated in the inset (a), and Fourier transform of the normalized EXAFS illustrating change in coordination/disorder of the second shell as a function of surface coating concentration (b)

The first peak at ~1.9 Å (Figure 3.6b) can be attributed to Cr – O interactions. It can be seen that the amplitude of this peak is relatively invariant within experimental error. It would indicate that chromium has a stable 6 coordinated oxygen shell in octahedral symmetry in agreement with the XANES information for both doped and coated situations. Furthermore, changing the thickness of chromium oxide coating seems to have very little structural effect on the first shell. The second peak at ~2.9 Å is due to either a Cr – Mn or Cr – Ni interaction depending on whether the host structure is ordered or disordered. It should be noted that as Cr and Mn are near neighbours in the Periodic Table, these two elements have similar backscattering properties and hence cannot be distinguished by EXAFS. However, the similarity in backscattering properties allows one to use either Mn or Cr to represent the metal backscatterer, without significantly affecting the EXAFS structural parameters that are determined by detailed fits to the data. In this case, the metal backscatterer is represented using the phase information and scattering amplitude of Mn to model the data. The greater proportion of Mn in the sample than either Ni or Cr, makes it more likely that chromium be surrounded by Mn.

Table 3.2. The bond distance R, Debye–Waller factor A, coordination number N. The value of the R-factor, which is a measure of the goodness of the fit is included. The number between parenthesis is the uncertainty in the last digit or digits of the parameter (10% or less).

			O			**Mn**		
	Sample	**N**	**R (A)**	**A ($2\sigma^2$)**	**N**	**r (A)**	**A ($2\sigma^2$)**	**R**
Doped:	Cr046+	6	1.99(1)	0.007(1)	6	2.91(1)	0.003 (1)	41.50
	Cr046+ after 16 cycles	6	1.98(1)	0.005(1)	6	2.91(1)	0.006 (1)	40.48
Coated:	Cr023 after 1min	6	1.98(1)	0.007(1)	6	2.91(1)	0.013 (1)	56.94
	Cr023 after 2cycles	6	1.98(1)	0.011(1)	6	2.89(1)	0.009 (1)	51.60
	Cr034	6	1.99(1)	0.006(1)	6	2.92(1)	0.009 (1)	49.62
	Cr034 after 2cycles	6	1.98(1)	0.007(1)	6	2.91(1)	0.018 (1)	74.83
	Cr057	6	1.98(1)	0.005(1)	6	2.91(1)	0.008 (1)	44.69
	Cr171	6	1.99(1)	0.007(1)	6	2.91(1)	0.006 (1)	44.69
	Cr171 after 1cycle	6	1.98(1)	0.006(1)	6	2.90(1)	0.007 (1)	43.41

Best fits of the EXAFS data are listed in Table 3.2. The Cr – O bond distance of 1.98 Å is in good agreement with that of 1.97 Å, which is expected for the Cr^{+3}-O bond the Cr substituted

$LiMn_{2-y}Cr_yO_4$ spinel structure[16]. The presence of six Mn atoms at ~2.9 Å conforms with that expected for Cr occupying octahedral sites in a lattice type similar to $LiMn_{1.825}Cr_{0.175}O_4$ from Jugovic et al [17]. There is no shift in the peak position so the bond lengths in both the 1st and 2nd shells are maintained upon cycling. The 2nd shell disagrees with the Cr-Cr distances in corundum Cr_2O_3 which are 2.65 and 2.89 Å [18]. Although much less common, the *g*-Cr_2O_3 oxide has a spinel structure and has been reported to be stable in very thin films [19].

Inspection of Table 3.2 shows that as the Cr content increases from Cr034, to Cr057 to Cr171 the Debye-Waller factor for the second shell decreases from 0.009 to 0.008 to 0.006 $Å^2$, which mirrors the decrease in amplitude of peaks in the second shell (Figure 3.6b). It is tempting to attribute this increased disorder to a real increase in static disorder imposed by the strain on the structure caused by the formation of vacancies at the surface. It would also follow that the thinner coatings would be more strongly affected by the strain induced by the substrate.

However, due to the direct correlation during the fitting between the number of atoms (N) and the Debye-Waller factor (*A*) these changes could also be related to the change in number of atoms as the surface coating concentration changes. It is not clear if this reduction in coordination number would be a real effect or if it would just be a numerical artefact of the analysis. It would mean the second shell contains either vacancies (surface termination) or lithium ions (as they are very weak backscatterers and cannot be clearly seen by EXAFS).

3.4 Conclusions

Coatings of chromium oxide have been successfully prepared on micron-sized particles of LNMO by a kind of dip-coating the LNMO powders in solutions of chromium nitrate. The chromium oxide layer was uniformly distributed over the entire particle. The thickness was estimated based on the BET surface area and the atomic ratio of chromium and manganese. The layer thickness then was between 0.4 and 2 nm depending on the amount of chromium nitrate used during dip-coating.

The assumption of the +3 valence of chromium was confirmed by XAS measurements. It was found that chromium remains in a valence state of +3 for both the doped and coated samples, irrespective of the thickness of the coating. Neither does the chromium valence change upon cycling, indicating that chromium is not involved in the intercalation redox process. However, the kinetics by coating with chromium oxide has been improved. Hence, Cr^{+3} acts as a catalyst for electrochemical processes occurring at the interface. For the same reason, Cr^{+3} improves the power performance once it is incorporated in the structure, e.g. by doping LNMO with chromium.

As measured with EXAFS, in $LiNi_{0.42}Cr_{0.08}Mn_{1.5}O_4$, chromium resides in an octahedral site coordinated to 6 oxygen at 1.98 Å and 6 manganese at 2.99 Å in good agreement with similar compounds from the literature. For the surface coatings, the site of the chromium is similar to those in doped $LiNi_{0.5}Mn_{1.5}O_4$, *i.e.* Cr^{+3} is in an octahedral site. It is, therefore, reasonable to conclude that the coating of chromium oxide adopts the spinel structure of the underlying lattice rather than the typical corundum structure of Cr_2O_3. Despite a deep research, a form of Cr_2O_3 where Cr remains in tetrahedral sites has not been reported. Consequently, and in correlation with the XRD results [12, 13], Cr is believed to adopt the spinel structure similar to its parent material LNMO, as soon as it remains in the first few atomic layers of the coating, and, therefore, creating an epitaxial layer. This then also proves a strong bond between the parent material and the coating. It is, however, stressed that the “epitaxial layer” could also indicate that instead of being a "coating", the Cr is partly "penetrating" into the underlying parent material. This has not been confirmed but may be an issue for further analysis.

Acknowledgments

The authors are members of ALISTORE – ERI. The financial support (for AB) is thankfully acknowledged from the ALISTORE-ERI. The authors would like to acknowledge the DUBBLE beam line staff for useful discussions and first class support, The Netherlands Organisation for Scientific research is also thanked for access to the DUBBEL beam lines.

References

1. Liu, D., et al., *Spinel materials for high-voltage cathodes in Li-ion batteries.* Rsc Advances, 2014. **4**(1): p. 154-167.
2. Manthiram, A., K. Chemelewski, and E.S. Lee, *A perspective on the high-voltage LiMn1.5Ni0.5O4 spinel cathode for lithium-ion batteries.* Energy & Environmental Science, 2014. **7**(4): p. 1339-1350.
3. Liu, G.Q., L. Wen, and Y.M. Liu, *Spinel LiNi0.5Mn1.5O4 and its derivatives as cathodes for high-voltage Li-ion batteries.* Journal of Solid State Electrochemistry, 2010. **14**(12): p. 2191-2202.
4. Kraytsberg, A. and Y. Ein-Eli, *Higher, Stronger, Better ... A Review of 5 Volt Cathode Materials for Advanced Lithium-Ion Batteries.* Advanced Energy Materials, 2012. **2**(8): p. 922-939.
5. Zhong, G.B., et al., *Electrochemical investigations of the LiNi0.45M0.10Mn1.45O4 (M = Fe, Co, Cr) 5V cathode materials for lithium ion batteries.* Journal of Power Sources, 2012. **205**: p. 385-393.
6. Feng, X.Y., et al., *Nonstoichiometric Li-1 +/- x Ni0.5Mn1.5O4 with different structures and electrochemical properties.* Chinese Science Bulletin, 2012. **57**(32): p. 4176-4180.
7. Wang, T.G., et al., *Study on nanocrystalline Cr2O3 films deposited by arc ion plating: II. Mechanical and tribological properties.* Surface & Coatings Technology, 2012. **206**(10): p. 2638-2644.
8. Sahan, H., et al., *Effect of the Cr2O3 coating on electrochemical properties of spinel LiMn2O4 as a cathode material for lithium battery applications.* Solid State Ionics, 2010. **181**(31-32): p. 1437-1444.
9. Zhang, L., et al., *Carbon combustion synthesis of LiNi0.5Mn1.5O4 and its use as a cathode material for lithium ion batteries.* Journal of Alloys and Compounds, 2009. **480**(2): p. 802-805.
10. Detectors, B.-D.-. 2012; Available from: http://www.esrf.eu/UsersAndScience/Experiments/CRG/BM26/Xafs/detectors.
11. Klementiev, K., *VIPER, freeware.* Journal of Physics D: Applied Physics, 2001. **34**: p. 209-17.

12. Arcon, I., B. Mirtic, and A. Kodre, *Determination of Valence States of Chromium in Calcium Chromates by Using X-ray Absorption Near-Edge Structure (XANES) Spectroscopy.* Journal of the American Ceramic Society, 1998. **81**(1): p. 222-224.
13. Nakai, I., et al., *In situ XAFS study of the electrochemical deintercalation of Li from Li1-xMn2-yCryO4 (y=1/9, 1/6, 1/3).* Journal of Power Sources, 2001. **97-8**: p. 412-414.
14. Ammundsen, B., et al., *Local structure and first cycle redox mechanism of layered Li1.2Cr0.4Mn0.4O2 cathode material.* Journal of the Electrochemical Society, 2002. **149**(4): p. A431-A436.
15. Jiao, F., et al., *Synchrotron-Based XANES Speciation of Chromium in the Oxy-Fuel Fly Ash Collected from Lab-Scale Drop-Tube Furnace.* Environmental Science & Technology, 2011. **45**(15): p. 6640-6646.
16. Balasubramanian, M., et al., *In Situ X-Ray Absorption Study of a Layered Manganese-Chromium Oxide-Based Cathode Material.* Journal of The Electrochemical Society, 2002. **149**(2): p. A176-A184.
17. Jugovic, D., et al., *Structural and magnetic characterization of Li Mn1.825 Cr0.175 O4 spinel obtained by ultrasonic spray pyrolysis.* Materials Research Bulletin, 2007. **42**: p. 515-522.
18. Gaudry, E., et al., *Structural and electronic relaxations around substitutional Cr3+ and Fe3+ ions in corundum.* Physical Review B, 2003. **67**(9).
19. Robbert, P.S., et al., *Novel electronic and magnetic properties of ultrathin chromium oxide films grown on Pt(111).* Journal of Vacuum Science & Technology a-Vacuum Surfaces and Films, 1998. **16**(3): p. 990-995.

Chapter 4 : AFM/SECM study

4.1 Introduction

In the previous chapter, comparisons between different LNMO samples containing chromium have been investigated, regarding the change of oxidation state.

We saw that no difference was visible between a doped and a coated LNMO material. Very promising results in terms of electrochemical results are expected and proofs of the enhanced kinetics due to chromium to be found. In this chapter, the description of a system where it is possible to determine the effect of the chromium, is made. It would be of great interest to measure this enhancement directly on the cell, while having a topographic picture of the interface.

To do so, a AFM and SECM were coupled together.

It then helped understand the surface charge transfer mechanisms and could, for instance, image the type, and the coverage, of coating needed to improve transfer.

This chapter describes the work that has been done to obtain a full description of the insertion/de-insertion of lithium ions in and out of this crystal, while cycling a full cell.

The work was shared between two EC-funded projects, the EuroLiion project and the E-stars project, of which certain results were already presented in the PhD thesis of Esteban Garcia-Tamayo.

4.2 Theory

4.2.1 Atomic Force Microscopy

Atomic Force Microscopy (AFM) is a type of Scanning Probe Microscopy (SPM) which can image the surface of both insulating and conducting substrates. An AFM probe consists of a sharp tip mounted on a flexible lever, fixed to a larger chip. The tip is scanned across the sample surface by means of a piezoelectric translator. The tip can be in contact with the surface (contact mode), and then the force acting on the tip changes according to the sample topography, resulting in a varying deflection of the lever. The probe can also be vibrated at its resonance frequency by means of a piezo oscillator, which is called tapping mode or semicontact mode (depending on the AFM manufacturer). During this oscillation, the tip just slightly taps the sample surface and the amplitude signal is detected, which can be translated to topography data as well. The deflection of the lever or the amplitude signal is detected by means of laser beam deflection off the cantilever, and subsequent detection with a double-segment photodiode, see Fig 4.1 [1]

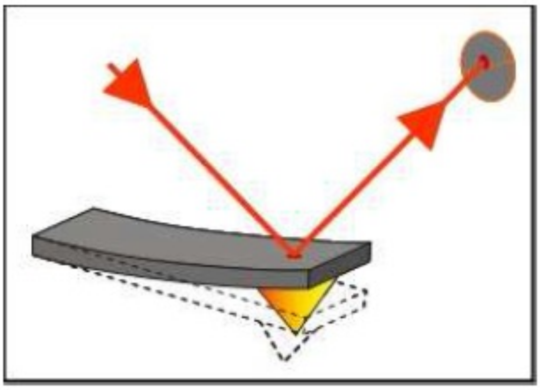

Figure 4.1 : AFM cantilever with tip, where cantilever deflection is measured by the changing deflection of a laser beam.[2]

The AFM is most typically used to scan the topography of samples. Because of the sensitive measurement of the cantilever deflection, resolutions of 0.01 nm in the direction orthogonal to the sample can be obtained. Silicon nitride and single-crystal silicon cantilevers are commonly used in commercial instruments. Ideally the tip would end in a single atom, giving atomic resolution in both horizontal directions. However the tips available have a radius of curvature around 10 nm. Possible artefacts have to be considered when using this technique. These are for example convolution of the surface topography with the tip geometry (e.g., structures sharper than the tip result in an image of the tip) or destruction of sensitive samples by the load of the probe. An important potential of AFM for surface chemistry is its capability to perform in situ measurements under liquids and in air. This allows direct observation of surface processes by operating the microscope with a liquid cell. In this cell, both sample and cantilever can be immersed in the liquid while measurements are made. Such studies can also be performed with a bias voltage applied to the substrate, which opens up valuable opportunities for electrochemical AFM (EC-AFM). For instance topographic measurements of a cycling battery could be made using this technique. [1, 3]

The AFM also has a number of configurations with which specific values of a substrate can be measured. One of them is the conducting or current sensing mode (C-AFM or CS-AFM). In this mode a metal-coated probe is scanned over the surface in contact mode while a fixed bias voltage is applied between the conductive probe and the substrate. This results in a local tip-surface current, typically dominated by the electronic component, with a resolution of 1-10 pA. [4] This method is used to scan the electronic conductivity of substrates, and has been applied to LMn_2O_4 layers [5]. However, no AFM option exists to measure the ionic conductivity of substrates by applying a voltage between the probe and substrate. We would like to measure in liquid at a constant distance from the surface, with a bias voltage applied between the probe and substrate. The probe would then be the counter electrode to the substrate. C-AFM measures in air and has direct contact between probe and substrate, which would short circuit our system. EC-AFM can only allow a voltage between the substrate and a reference electrode, and not a voltage to the probe. But another SPM technique is able to measure the ionic conductivity of a substrate [6].

4.2.2 Scanning Electrochemical Miscroscopy

Another type of Scanning Probe Microscopy is the Scanning Electrochemical Microscopy (SECM). This method can image the reactivity of a surface at a microscopic scale, using an ultramicroelectrode (UME) instead of a cantilever for a probe. This probe consists of a metal core covered by glass, where only the top of the metal is exposed. A bias voltage is applied to the UME, resulting in a redox reaction at the exposed metal. Both the substrate and the probe are immersed in a solution containing an oxidizable species R. When a sufficiently positive potential is applied to the probe, R is oxidized to O, using electrons from the UME (Figure 4.2a).[7]

The current flow (It) resulting from the applied potential is time dependent. It also depends on the tip diameter and decays to a steady-state value it,∞ at distances far from the substrate. The steady-state current is governed by the mass transfer of O to the UME and is given by Equation 4.1 where O is the concentration of O in the solution, D the diffusion coefficient and a the diameter of the tip. When the tip is closer to the sample surface, the measured current is different from $i_{t,\infty}$. The current is then expressed relative to $i_{t,\infty}$ to obtain a normalized, time independent value [8]

$$i_{t,\infty} = 4n[O]FD\alpha \qquad \text{(Equation 4.1)}$$

When the tip is brought within a few tip radii of a conductive surface (Figure 4.2b) the O species formed in the reaction at the tip diffuses to the substrate where it can be reduced back to R. This process produces an additional flux of R to the tip and hence "positive feedback", so the tip current increases. The shorter the tip-substrate separation distance (d), the larger the tip current.[7]

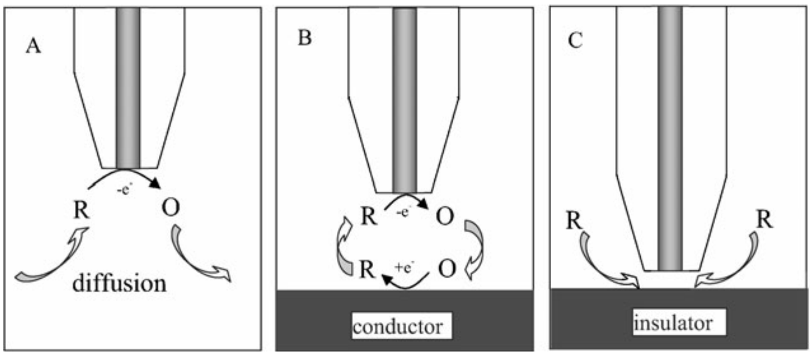

Fig 4.2 : Feedback mode of the SECM operation. (A) The UME tip is far from the substrate. (B) Positive feedback: species R is regenerated at the substrate. (C) Negative feedback: diffusion of R to the tip is hindered by the substrate.

If the substrate is an inert electrical insulator, the tip generated species, O, cannot react at its surface. At small d the insulator blocks the diffusion of species R to the tip surface, giving lower tip current or "negative feedback" (Figure 4.2c). Overall, the rate of the mediator (R) regeneration at the substrate determines the magnitude of the tip current, which means the tip current vs. distance dependence provides information on the kinetics of the process at the substrate (Figure 4.3) [7].

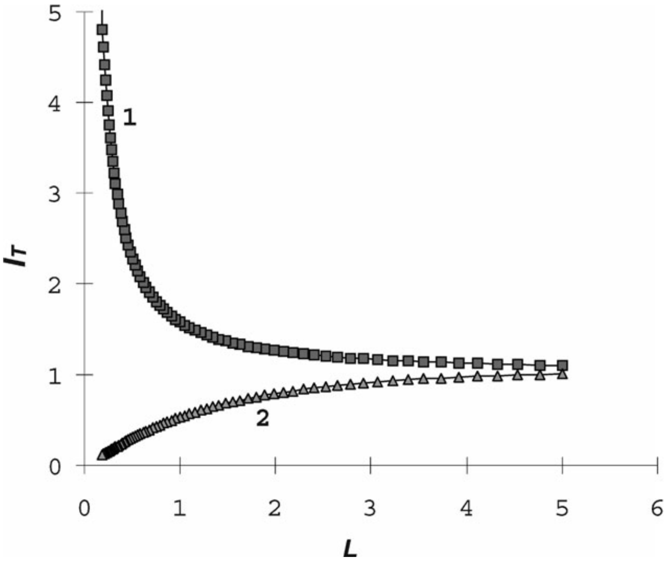

Fig 4.3 : Theoretical approach curves for a tip electrode over a conductive (1) and insulating (2) substrate.

An SECM operates by scanning an electrode in a fixed plane without distance feedback. This means the UME tip can easily crash, and the tip-substrate separation is not well-defined or constant. Next to this, the size of UME tips limit them to micrometre resolution. To obtain figures with sub-micrometre resolution at a constant and well controlled height, a combination of an AFM and SECM can be made, as described in the next section [9].

4.2.3 SECM-AFM Combination

The first SECM-AFM combination was described in 2000 by MacPherson and Unwin [10], and since this moment there have been a lot of approaches to combining these SPM methods [9, 11, 12]. They all involve specially designed AFM probes, mounted in an AFM and operated with a bipotentiostat. Probe options include: 1) Hand-fabricated probes, made from an etched wire, insulated at all but the tip end. 2) A commercial silicon nitride probe, coated in metal and insulator and using focused ion beam technology to reshape the probe so as to expose the electrode. 3) Batch microfabricated probes, made at the wafer level, which incorporate a triangular electrode at the very end of the probe. 4) Nanoelectrode probes based on the use of single-walled carbon nanotube bundles on AFM tips. All of these probe designs contain a small electrode and one of their main uses has been to carry out high resolution topographical and electrochemical imaging of surfaces [9]. For research in Lithium-ion batteries we don’t have to make such complicated special tips, however, because a standard silicon tip can act both as probe and electrode. When lithiating it with a small enough amount of lithium, the tip should remain intact and the tip diameter should not be too much increased. Lithium ions can then migrate from the tip to the surface, or the other way around, driven by an applied voltage. The resulting current can be measured and indicates the ease of lithium ion (de)intercalation on the substrate/electrolyte interface. This method would then be very similar to existing SECM/AFM combinations. To our knowledge, no one has attempted using standard silicon AFM probes for Li-ion battery SECM characterization yet [11, 12]. A dual-mode AFM/SECM method described by Davoodi et al. could be used for collecting data. After a normal AFM linescan to obtain a surface profile in the first pass, the feedback was stopped and the tip withdrawn to a desired distance from the surface. In the second pass, the probe followed the surface profile in the second linescan with a constant lift-up distance, and collected the local current. This distance should be optimized so the probe does not touch the surface, but also not be too far because this decreases the resolution [13].

The image resolution with an AFM probe could ideally be as high as the tip diameter is small. However two aspects introduce strong limitations to the image resolution. First, measurable forces concentrated in a few atoms generate strong deformation of the tip and/or substrate. Secondly, long range forces (e.g. electrostatic forces) are sensitive to the overall shape of the tip. The second argument appears to be especially relevant in electrochemical systems in which variations of the applied potential may introduce substantial changes in the charge of the diffuse layer [12] The diffusion profile of ions through the electrolyte should be taken into account as this strongly influences the obtained pictures. Most diffusion profile models are for cases where the probe is insulated and only the tip is exposed [13, 14], and one model describes the case for an un-insulated probe [9]. To limit the diffusion distance of ions, short pulses were used here to obtain higher spatial resolution. In this diffusion limited case a time lag of the order d2/2D was found for the response (d=separation distance, D=diffusion constant). It is recommended that probes should be insulated when imaging conductive substrates. However, it would be more convenient if un-insulated probes can be used.

4.3 Experimental

In this section details of the experimental setup, materials and procedures used in this project will be given. However, a description of the complete electrochemical AFM combination (i.e. a system where morphological images can be taken while performing in-situ electrochemical measurements) won’t be given, as this functionality is not possible at present. Ideas on the final system will be therefore discussed at the end of the results and discussion section.

4.3.1 AFM and Electrochemical Cell setups

The AFM used in this research is an NT-MDT Ntegra platform P9, controlled by Nova px software. For electrochemical experiments the SMENA liquid head was used. An optical microscope (Optem 2.0x mini) was available on top of the AFM setup.

When measurements in liquid are required, the SMENA liquid head is used instead of a standard AFM head. A picture of the electrochemical cell (EC) in the AFM setup with the SMENA head attached to it, is shown in Figure 4.4(a). By using the optical microscope (with a digital camera function) placed above the head, images of the probe, positioned under a transparent crystal, could be taken using mirrors. Such a picture of an immersed probe is shown in Figure 4.4(b). During liquid AFM experiments, the laser intensity is automatically lower because of absorption by the electrolyte and reflections through the crystal. In these types of measurements, contact mode is preferred as it is easier to carry out and the damage to the sample is less relevant.

For future application, there is the possibility to make a topographic line scan first and then follow the same path with the probe in a second run at a constant distance. This is the sort of strategy desired for electrochemical measurements. An optimal distance can be found by making slow approach curves and looking where the current starts to increase. Another option would be to scan at different points and, while the feedback loop is turned off, the probe is then retracted around 3 um from the surface.

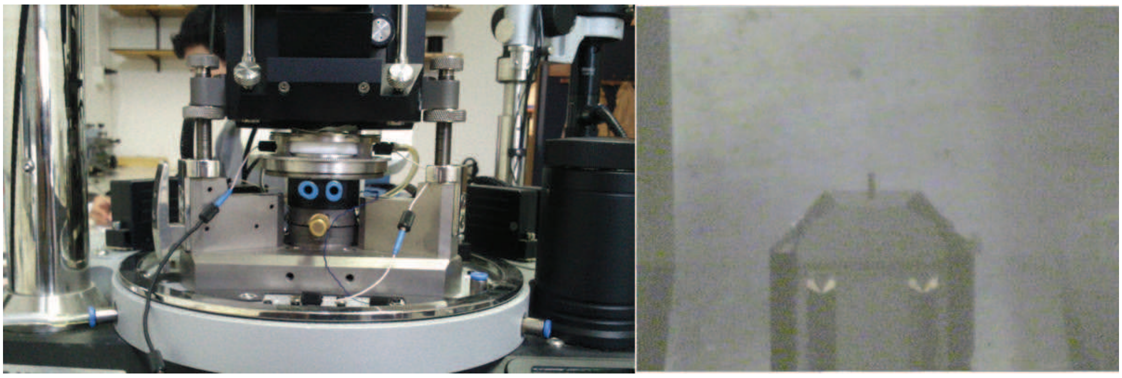

Figure 4.4 – Electrochemical cell in the AFM setup with SMENA head attached. (a) Side image and (b) digital microscope image (top) of immersed probe.

The full system and the connection layout are schematically shown in Figure 4.5(a). The EC is designed for electrochemical measurements with the Scanning Tunneling Microscope (STM) head of NT-MDT [13]. The sample (1) is placed at the bottom of the cell's chamber (5) which is filled with liquid electrolyte (4). The sample or working electrode (WE) is connected to the bipotentiostat (2). A reference electrode (3) is immersed in the electrolyte close to the working electrode (WE). Finally, the scanner (6) is connected to the probe port of the bipotentiostat. The EC has three electrical connections, two of them are ports placed in the diameter of the chamber, while the third one rests at the bottom. An extra connection for the tip was added on top of the cell. The bipotentiostat delivered with the NT-MDT electrochemical cell package was not used as it has limited functionalities to what was needed, therefore a Maccor (model 2200) was used to perform the electrochemical tests, as it will be described in Subsection 5.2.2. . Figure 4.5(b) shows a schematic drawing where the cross-section of the EC and all the components are exposed.

A picture of the AFM probe holder can be seen in Figure 4.5(c). This holder is attached to the AFM head by means of a magnetic ring (localized at the top in Figure 4.5(b) and bottom in Figure 4.5(c)). A fork is used for the correct handling of the probe holder and it also helps to keep a distance of roughly 1 mm between the probe and the sample preventing tip crash. The fork is taken off only when the probe holder is correctly attached to the head, as the distance between probe and sample is then controlled by the AFM system. For pressurizing the working area and to make sure the cell is airtight, the probe holder is equipped with a silicon membrane. Between the membrane and the base, a copper wire was coupled to provide a connection between the probe and the outside. The SMENA head has a crystal on the top through which the laser can see the probe while it is immersed in a liquid. The AFM (silicon) tip is placed on top of the crystal and will be used as an in-situ AFM electrochemical probe and as counter electrode.

Figure 4.5(d) shows a picture of the EC base. A TeflonR chamber, whose inner part has a stainless steel cover, is then filled with the electrolyte solution. The sample is placed on the bottom of the chamber and is mechanically held to it by a brass L-shaped hook (visible in the right side, Figure 4.5(b)), which also serves as a current collector. A second L-shaped brass hook, with a drilled hole in the extreme which is immersed in the electrolyte, holds a piece of metallic lithium that will act as reference electrode. These hooks fit in stainless steel clips (as seen in Figure 4.5(b)), which are in contact with wires to allow the connection with the bipotentiostat. The EC also features gas inlets.

4.3.2 Electrochemical procedures

All electrochemical measurements were done using the electrochemical cell. Most of them were carried out in the glovebox, where built-in ports permitted the connection to a Maccor S4000 cycler. For those electrochemical tests combined with the AFM (performed outside the glovebox), a Maccor S2200 was used.

Most of the experiments were in a two-electrode setup which consisted of silicon (AFM probe) as working electrode and metallic lithium as reference and counter electrode. The experiments performed are summarized in Table 4.1.

Table 4.1 : Summary of electrochemical experiments

Experiment number	Probe previously used	Applied current/voltage (uA / V)	Voltage limits (V)	Number of cycles
A	Yes	10	0.05-1.5	5
B	Yes	3	0.05-1.5	10
C	Yes	3	0.05-1.5	1
D	No	3	0.05-1.5	10

E	No	3	0.05-1.5	1
F	No	3	0.05	1 discharge
G	No	1, 5, 1	0.05-1.5	30
H	No	3 / 0.3	0.3	1 discharge

All experiments started with a galvanostatic discharge. Samples were then either cycled further galvanostatically, or discharged potentiostatically. Galvanostatic cycling was done to observe the behavior after the first cycle. As mentioned in Subsection 4.1.3 a constant voltage is required. Therefore poten- tiostatic discharge is the most probable mode to be used in the final system. To prevent jumps in the voltage, the potentiostatic voltage has to be achieved by galvanostatic charge or discharge. Three-electrode experiments were also carried out, using LNMO (produced in the same way as for Chapter 3) as third electrode. The Reference Control functionality available for the Maccor S4000, which gives the option of an auxiliary input, was used in this case. This scheme provides voltage control between the WE and the RE, while the current flows between the WE and CE. The channel output voltage is then WE vs. RE and the auxiliary voltage output gives WE vs. CE.

During most electrochemical test performed, there was electrolyte evaporation

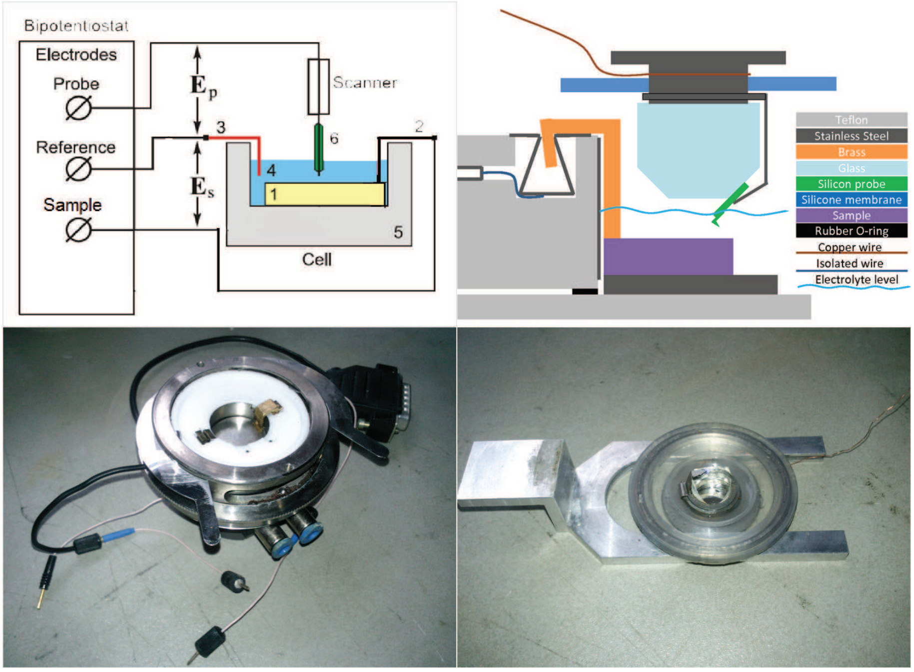

Figure 4.5 – (a) Scheme of the electrochemical setup with layout of connections: (1) sample (working electrode); (2) current-collector;(3) Li^0 reference electrode;(4) electrolyte; (5) cell housing; (6) Silicon SPM tip (counter electrode). (b) Cross-section schematic drawing of the liquid cell for the AFM; images of (c) bottom part; and (d) top part

because of leakage in the electrochemical cell. As a result, the electrolyte volume in the chamber was constantly changing during the reaction making it difficult to know what part of the probe was actually immersed. This gives rise to an intrinsic problem to calculate the C-rate as it is based on the electrode weight. Therefore, a fixed current of 3 μA was chosen for most experiments (as shown in Table 4.1) and will be more elaborately discussed in subsection 4.4.1.

4.3.3 Materials Used

The AFM probes used were of the types NSG03 [8] and NSG30 [1]. These are probes fabricated by NT-MDT meant for non-contact or semi contact scanning, but can also be used in liquid and in contact mode. They are made from single crystalline silicon (n-type) doped with antimony, with a bulk resistivity of 0.025 Ω cm. The chip sizes are 3.4 x 1.6 x 0.3 mm. The tips are 14-16 μm high and have a typical curvature radius of 10 nm. The cantilever dimensions are different for the two types of probe. For the NSG30, the size is 125±10 x 40±5 x 4.0±0.5 μm and for the NSG03 the size is 135±10 x 30±5 x 1.5±0.5 μm. The volume and mass of every part of an NSG30 probe is given in Table 4.2, using a density of 2.329 g cm^{-3}. The mass ratio between the probe components is given as well [15].

Table 4.2 : Volume and mass of NSG30 probe components

	Dimensions	Volume	Mass	Mass ratio
V *chip*	3.4 x 1.6 x 0.3 mm	1.6 mm^3	3.8 mg	4 - 10^6
V *cantilever*	125 x 40 x 4 μm	20-103 μm^3	47 ng	50
V *tip*	1/4 $*$ 15 x 10 x 11 μm	413 μm^3	0.96 ng	1

Thin LNMO layers were electrosprayed, based on recipes described in next chapter. Spray times of 10 minutes, with fixed flow rates and concentrations, were chosen to achieve relatively flat layers. Aluminum foil and silicon wafers (thickness 0.8 mm) were used as substrates. Some LNMO samples were coated with chromium oxide, following the details described in Chapter 5.

Experiments in the glovebox (MBraun) were performed under argon atmosphere. For most experiments outside the glovebox, the cell chamber was constantly flushed with helium so as to create an inert environment. Metallic lithium was used as negative electrode. The electrolyte solution used was 1.0 M $LiPF_6$ in ethylene carbonate : dimethyl carbonate (EC:DMC) (1:1 by wt%). As DMC evaporates quickly at room temperature and EC subsequently crystallizes, DMC (Dimethyl carbonate, anhydrous, Merck) was often added to again dissolve the electrolyte.

4.3.4 Probes storage and characterization

In order to decrease the waiting time of the first probe discharge (lithium insertion), using a probe which has been previously lithiated could be convenient. Therefore an investigation of whether the probes changed after a certain storage time was conducted. After the electrochemical experiments most probes were rinsed with different solvents: with DMC in the glovebox, with ethanol outside the glovebox, with both DMC and ethanol, and some were not rinsed at all. These probes were then stored.

Stored probes were characterized using a Phillips XL20 scanning electron microscope, operated at 15 kV. Moreover, a JEOL JSS-7500F SEM coupled to a NORAN System SIX, was used for energy dispersive x-ray spectroscopy (EDX) analysis.

4.4 Results and Discussion

In this chapter the results of both the experiments and the ’development process’ will be discussed. The first section covers the electrochemical experiments. This is followed by some data on the storage of tips, and topographical images in the AFM. In Section 4.4.1 a discussion on the setup problems will be carried out and of some improvements that have either already been applied, or that should be applied to continue with this research. Finally, an important part will deal with how we think the modified AFM will look like, in the end.

4.4.1 Electrochemical experiments

Silicon probes were charged and discharged versus metallic lithium as described in section 4.4.2. Figure 4.6 shows the second cycle, as the first cycle usually involves SEI layer formation and also irreversible reduction of surface layers formed on silicon (SiOx, Si-OR and Si-R) [14]. The discharge plateau between 0.2 and 0.05 V and the charge plateau between 0.3 and 0.7 V gives a similar electrochemical behavior to what has been previously reported in the literature [9]. From this electrochemical behavior we can conclude that we have a working battery of silicon vs. lithium, which proves that the silicon probe can be lithiated. Some lithiated probes have been studied with Scanning Electron Microscopy. In Figures 4.7(a and b), a probe is shown which has been discharged to 0.05V (i.e. lithiated). When compared with the fresh tip in Figure 4.7(c), a change of the surface can be observed, although the shape of tip is still intact. A probe which was discharged to 0.01V and charged again is shown in Figure 4.7(d). Here it is very clear that the de-intercalation of lithium caused the silicon host to crumble. As this crumbling destroys the tip, making it unpractical for AFM measurements, the cut-off voltage for the discharge should not be very low.

Discharge curves from some of the probes previously used (including those shown in the SEM picture above) are shown in Figure 4.7. Probes A and C had been cycled earlier, while probes D, E and F were pristine, as described in Table 4.1. It can be immediately appreciated that the open circuit voltage of pristine tips is between 2 and 3 V and probes previously used have an OCV between 0.5 and 2 V. This is because of the reactions we see at higher voltages, suggesting that surface layers are reduced and an SEI is formed, as discussed in section 2.5. All probes show a voltage plateau at voltages between 0.5 and 0.05V, indicating lithium insertion in the silicon. The exact voltage levels and lengths of the plateaus differ significantly however, even though the setups and procedures are practically identical. In experiment A, a current of 10 μA instead of 3 μA was used, but this does not influence the Voltage-Capacity curves. Another noteworthy aspect is the noise and voltage jumps which are caused by poor electrical connections. This will be discussed in more detail in section 4.5.1.

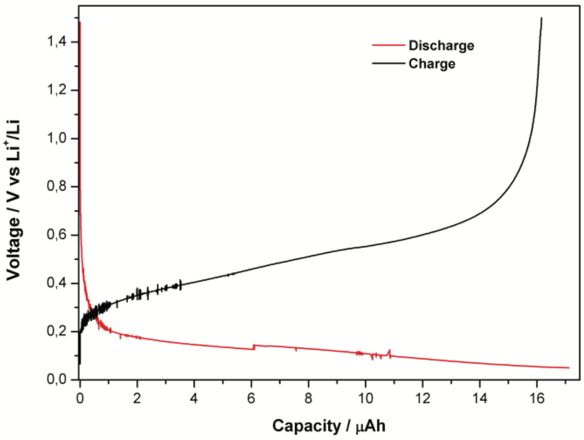

Figure 4.6 – Charge and discharge of silicon probe vs. metallic lithium (experiment B)

As mentioned in sections 4.1.2 and 4.2.2, it is necessary to identify which voltage to use for potentiostatic measurements, in combination with the AFM. This voltage should be stable, i.e. at a plateau, to be able to measure for a significant amount of time at a constant voltage. However, it would be convenient if this voltage is as high as possible so that there is as little as possible lithium in the silicon in order to avoid too much volume expansion of the tip and, also, to minimize the waiting time until the voltage is reached. Still, lithium should be inserted at this voltage in any probe. Taking these above considerations into account, it is decided that 0.3V is the highest possible voltage.

Usually, the applied current in galvanostatic measurements is based on the electrode mass and expressed in C-rate. However, in this project a constant current was used (see section 4.2.2) because the mass of active silicon varies during the experiment as, because of the electrolyte evaporation, the exposure of the AFM's cantilever varies. Potentiostatic experiments are preferred for the combination with the AFM, as previously discussed in this subsection.

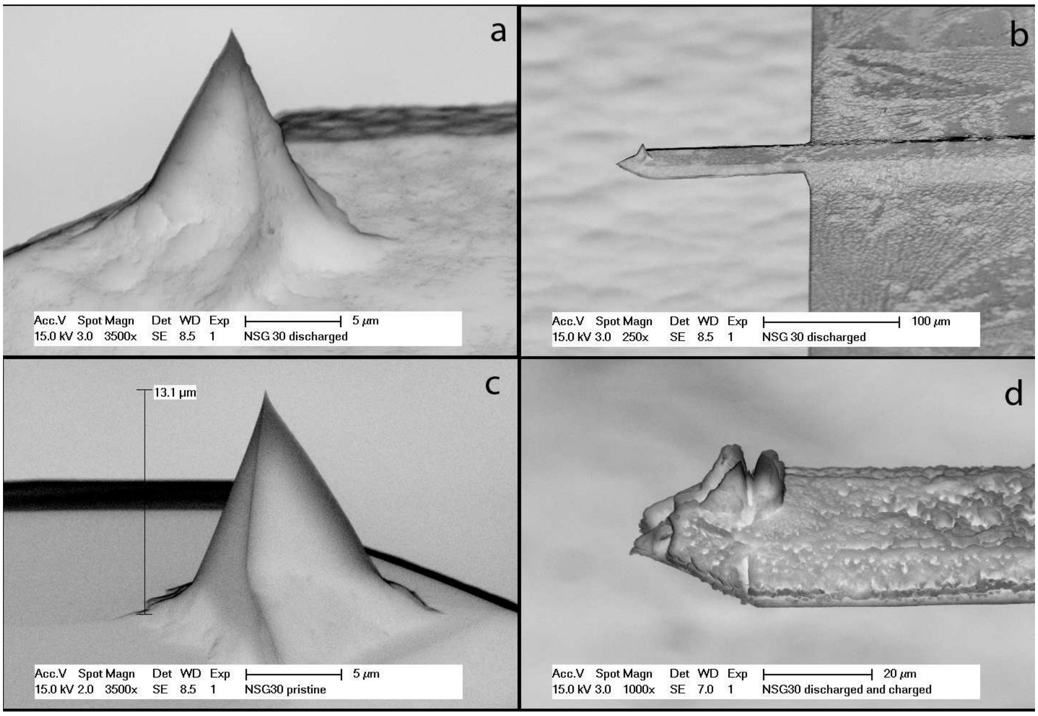

Figure 4.7 – SEM pictures of NSG30 tips; a) once discharged tip(in exp. E); b) once discharged tip and cantilever (in exp. E); c) pristine tip; d)once discharged and charged tip (in exp. F)

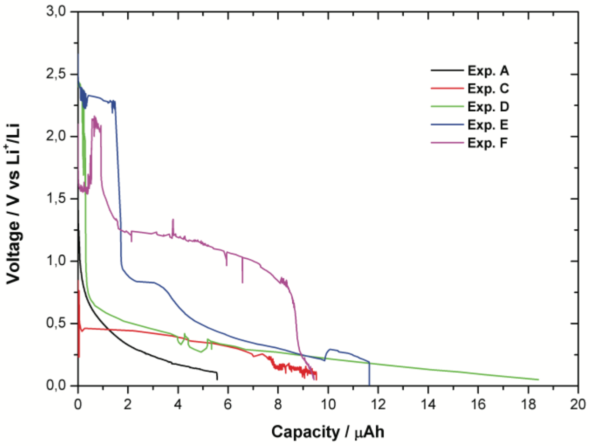

Figure 4.8 – Discharge curves of experiments A, C-F. Experiments E and F correspond to SEM pictures above

To obtain the desired voltage of 0.3V, the cell is discharged galvanostatically at a current of 3 µA, as depicted in Figure 4.9. When the voltage reaches 0.3V, 10 minutes of potentiostatic discharge followed, after which the cell was turned to a rest stage. In this case the voltage profile is flat, indicating perfect electrical connections. The current slightly fluctuates around 3 µA, as it does in every galvanostatic experiment, and decays in the potentiostatic mode. This is because there is a decreasing amount of silicon which can be lithiated at this voltage. A similar effect is described in section 4.1.2. An attempt was also made at doing three-electrode measurements, where a third electrode of LNMO was added. As described in Subsection 4.2.2,an auxiliary voltage input in the Reference Control mode of the Maccor was used. In this case, LNMO was acting as the working electrode (WE), Si as the counter electrode (CE) and Li as the reference electrode (RE). This means that the reaction between LNMO vs. Li could be controlled, while the current would actually run between LNMO and Si. Such measurement is shown in Figure 4.10. A very slow charging of the LNMO can be seen, and a faster discharge of Si.

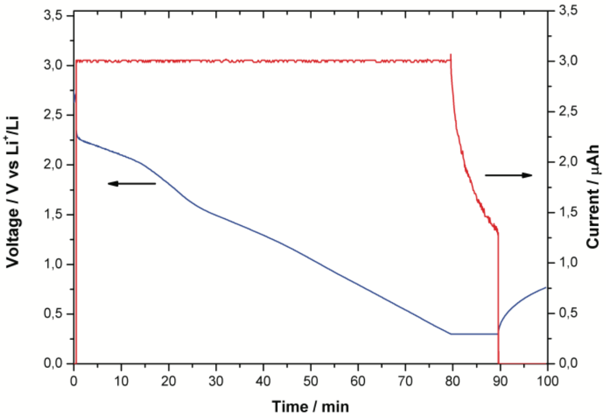

Figure 4.9 – Time profile of galvanostatic discharge (3 µA) to a voltage value of 0.3 V, followed by 10 min potentiostatic discharge (experiment H)

The spike obtained at around 70 minutes is probably due to loss of contact for a very short time, leading to fast relaxation of LNMO and Si. Nevertheless, the system recovered and resumed charging and discharging. Finally, the voltage of Si vs. Li drops below 0 V, which could only indicate lithium plating on silicon. As the capacity of LNMO is higher than that of Si, because of the big difference in active masses, the LNMO is not fully charged while the Si is already fully discharged. Hence, the capacities should be better matched, or the control should be with regards to silicon and not to LNMO.

The ideal setup would use the Maccor cycler to control LNMO vs Si and Si vs Li simultaneously, as the probe is then constantly kept at the same level of lithiation avoiding a decreasing current vs. time due to the probe delithiating. Unfortunately, with this system, in its present form, it was not possible to perform such a measurement. This means that two devices have to be used for voltage control, one recording the reaction between LNMO and Si (preferably the Maccor), while the voltage of Si and Li could be kept stable by attaching, for example, a Si vs. Li battery, which is at the same voltage, with a very large capacity.

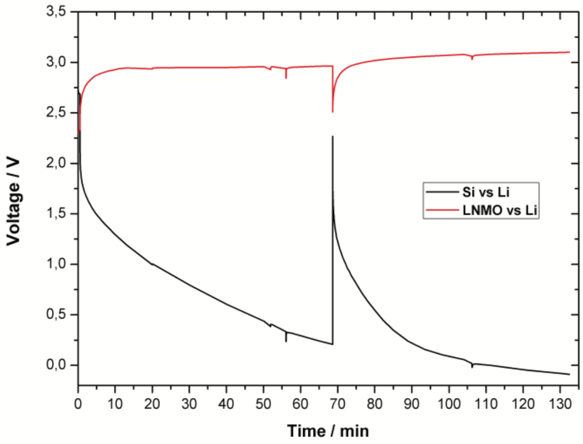

Figure 4.10 – Three-electrode measurements of LNMO (WE) vs Si (CE) and Li (RE)

4.4.2 Probe storage

The probes were stored at ambient conditions, so they could have reacted with air and moisture. Figure 4.10 shows SEM pictures of NSG03 probes under different circumstances. The tip and cantilever in Figure 4.11(a and b) are the same as the tip in Figure 4.10(c), but after being stored for two months. When comparing Figure 4.11(a) to Figure 4.11(c) the protrusion on the tip and the 'islands' on the cantilever seem to have decreased in size. During this time the lithium seems to insert further into the silicon, thereby distributing more evenly. Besides, after this period of time, the cantilever bends as seen in Figure 4.11(b). For a non-lithiated tip stored in exactly the same environment as the lithiated one, no bending of the cantilever is observed (Figure 4.10(d)). An explanation for this is that, most probably, lithium inserts further into the cantilever increasing its volume in certain spots causing mechanical stresses that makes it bend. This would mean that the bottom part of the cantilever (when mounted in the setup) reacts with more lithium than the top part. Note that in Figure 4.8 the tip is at the top in contrast to how it will be mounted in the AFM set-up. If the cantilever is bended too much, the laser spot in the AFM cannot be reflected in the right direction, leaving the probe useless.

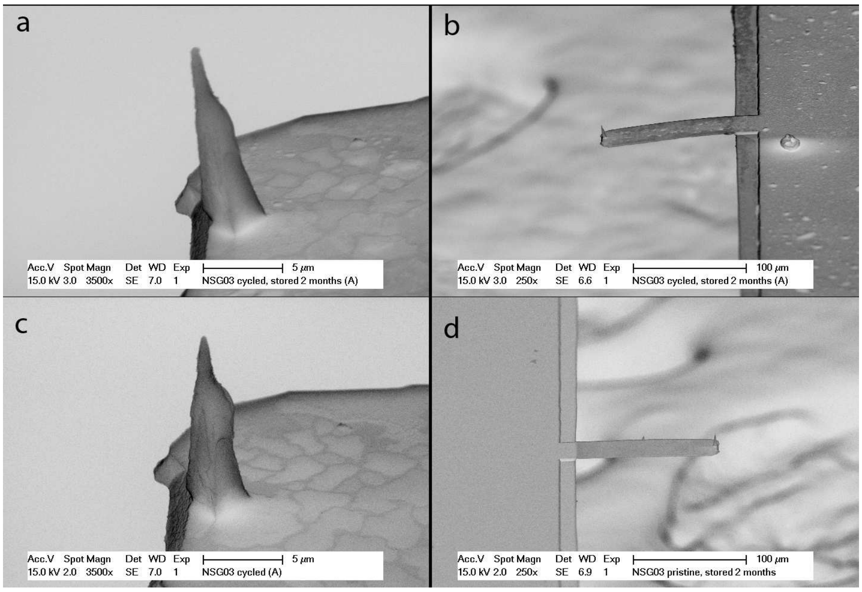

Figure 4.11 – NSG03 probes; (a) lithiated tip stored for 2 months; (b) bended cantilever, same as a; (c) same tip as a, directly after lithiation; (d) stored pristine probe, with no bended cantilever

After some storage time has passed, crystals are formed if the probe was not rinsed before storing it. Most of these crystals are cubic, as can be seen in Figure 4.10 and in the SEM micrographs shown in Figure 4.14, which will be described later. EDX images of a stored cantilever are shown in Figure 4.12. The tip is shown from above and a large crystal is lying next to it. In fact this is the same probe as in Figure 4.6(a and b), although these EDX pictures are made after a month of storage. The cantilever itself mostly consists of silicon, as expected, with traces of oxygen, nitrogen and sodium. The crystal is clearly formed from the electrolyte salt ($LiPF_6$), because it is mainly constituted of fluorine and phosphorus.

4.4.3 Topographical AFM scanning of the sample

In order for the combined electrochemical AFM method to work, it should be possible to scan with a lithiated probe, as discussed in section 4.1.2.

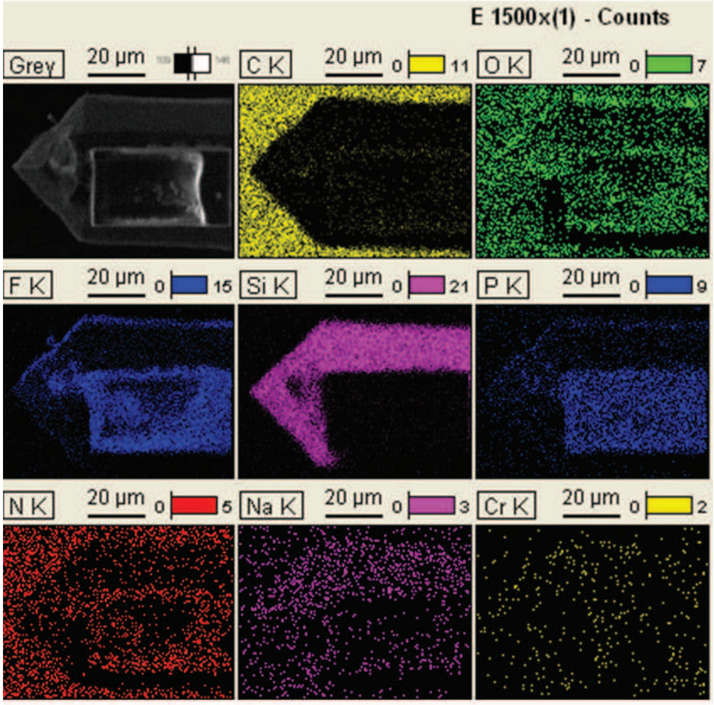

Figure 4.12 – EDX pictures of a probe cantilever and tip, from experiment F, taken one month after Figure 4.6(a and b). Color scales give the counts of elements in the picture

To prove that a lithiated probe can be controlled, a topographical scan in the contact mode was performed in a dry environment. Figure 4.13(a) shows an AFM image performed with a pristine tip on a sample of LNMO partially coated with chromium oxide, synthesized as described in Chapter 3. Figure 4.13(b), on its turn, shows a clear topographic image carried out with a lithiated tip. Therefore the feasibility of a scanned topography with a lithiated probe is demonstrated. The next step is to replicate the experiment in-situ. To obtain this image, a tip force of approximately twice the one used in regular procedures was required.

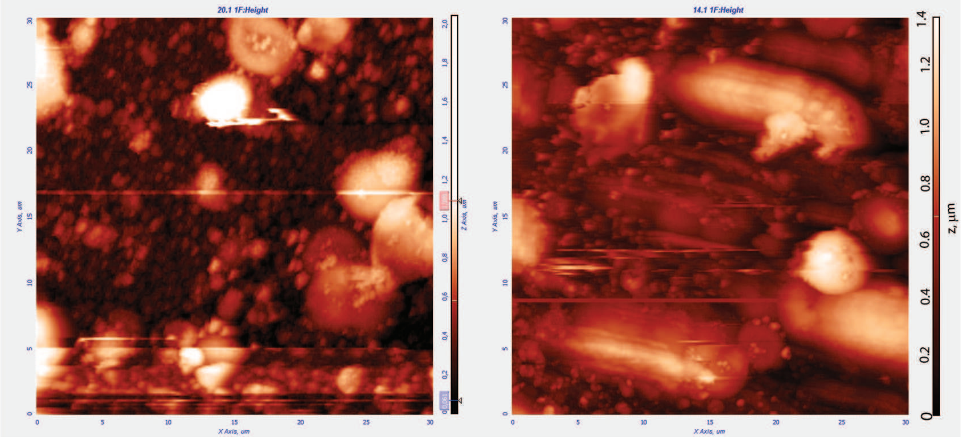

Figure 4.13 – AFM scan of LNMO with chromium oxide; (a) scanned with a pristine probe (30x30 µm); (b) scanned with a lithiated probe(30x30 µm)

Before the probe was used for AFM scanning it was observed under the SEM (Figure 4.14). The tip is shorter than the pristine one, which means it 'broke' during electrochemical measurements. However, for this purpose, it broke in a convenient way as there is still a relatively sharp tip with an approximate tip radius of 350 nm (Figure 4.14(b)). This corresponds quite well with the smallest artifacts observed in Figure 4.10(b), which are of the same order of magnitude, therefore the tip convolution is small enough. This probe had been stored for two weeks, and as discussed in the previous subsection, crystal formation of LiPF6 can be seen on the chip and cantilever.

It is the aim of this research to make a topographic scan using a pristine (non-lithiated) tip in electrolyte, followed by a second scan made at a constant distance from the surface with a lithiated tip (see Subsection 4.1.2). Figure 4.13(a) shows an AFM scan done on a similar kind of sample as those shown in Figure 4.11, only this time performed in liquid electrolyte with a pristine tip. Scanning within the filled liquid cell is not

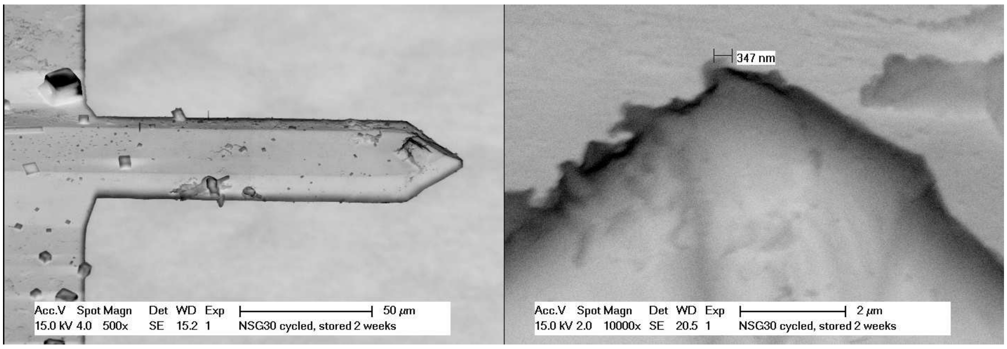

Figure 4.14 – Probe which was used to scan Figure 4.10(b); (a) cantilever (b) tip end

straightforward, however, as will be discussed more elaborately in the next subsection. Simultaneous to AFM approaching and scanning, a voltage of 0.2V was applied between the probe and lithium. Unfortunately, no stable current flow was measured as shown by the voltage-and-current graph vs. time in Figure 4.14(b), most likely because of poor electrical connections.

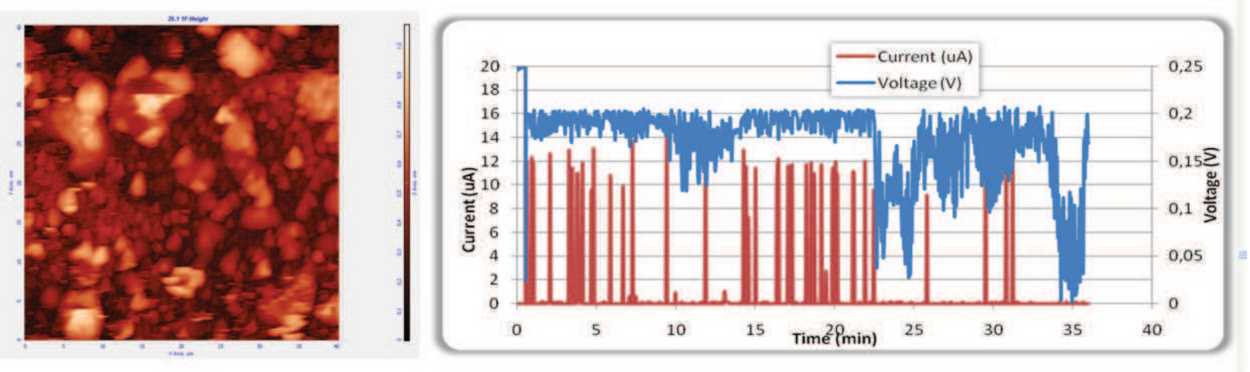

Figure 4.15 – (a) AFM scan of LNMO with chromium oxide, scanned in electrolyte (40x40 μm); (b) Electrochemical behavior of Si vs Li during AFM scanning

4.5 Future research

As has been mentioned before, the technique presents several unresolved issues at present. Because of this, it was hard to achieve reproducibility in the experiments. Solutions have already been found and implemented for some issues. For others, further research is needed in order to optimize the setup, the technique and the procedure.

4.5.1 Setup improvement

The main problem in almost all the experiments was that the electrical connections were not stable, as it is clearly observed from the shape of the graphs in Figure 4.8, 4.10 and 4.15(b). In the schematic drawing of Figure 4.15 all the electrical connection points of the cell are shown. The points of which there were poor or no electrical connection are indicated in red circles.

- (1) The copper wire that is wound around the stainless steel crystal base oxidizes and unwinds with time. This was partly solved by placing the wire underneath the membrane ridge, preventing unwinding. It does, however, increase the chance of gas leakage.

- (2) The brass hook does not apply enough pressure on the sample to have a stable connection. Because of its shape, there is no mechanical force applied on the hook by the clip, so it ‘floats’ in the setup.

- (3) The wire underneath the clip is the most troublesome connection. The clip oxidizes with the electrochemical reactions, forming an insulating oxide layer. On top of this, the pressure the clip provides on the wire is not high enough, giving mechanical instability. Finally, the wire is very fragile and broke several times during the experiments. A solution for the issue with oxidation is that the wire, clip and hook should preferably be made of platinum.

- (4) The electrolyte level drops during prolonged experiments, leaving the probe un-immersed in the electrolyte. This is mainly because DMC evaporates quickly at room temperature. The remaining electrolyte solution, EC, finally crystallizes (after more or less 10 h), as it does so at room temperature. Experiments could be done with the probe in crystalline electrolyte, however the cantilever would break when the cell was opened to add more DMC in order to dilute it. This could be prevented by arraying out short experiments in the cell (4 h). Moreover, low electrolyte levels were also due to leakage through the bottom, the side connections or the top, mainly caused by the constant (although needed) manipulation of the cell during experiments. Another important aspect in these types of measurements is that the reactions should take place in an environment without moisture, oxygen or nitrogen.

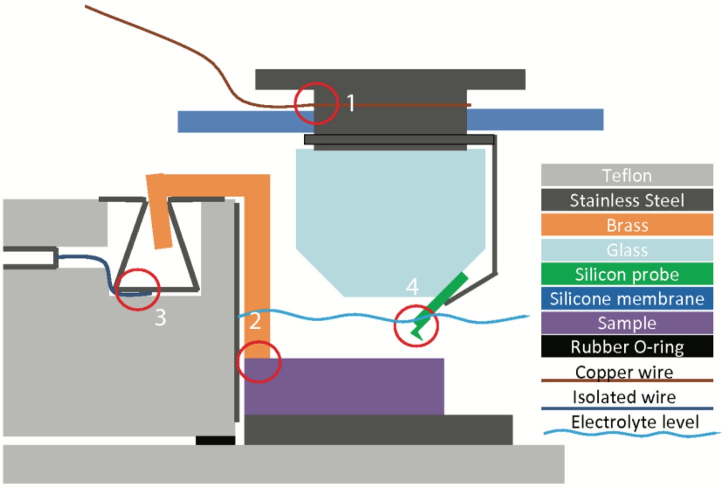

Figure 4.16 – Schematic of the faulty connections in the setup, half the cell is shown

Therefore a stable environment with inert gas should be used and all the leaks avoided.

- All the parts of the setup have to be dried, especially the AFM probe when used in the AFM setup. If this is not done properly, bubble formation (probably H2) and layer formation (a LixNyOz compound) occurred at the probe. Such artifacts can be seen in Figure 4.17. Beside reaction contamination, the bubbles blocked the laser and the formed layer de- creased the reflected laser intensity. This stopped the laser feedback and the probe position could not be read or controlled by the AFM software. When experiments were carried out in the glovebox, probes which were not dried did not cause bubble or layer formation, therefore the environment where the measurement takes place also plays an important role.

- As the cell was not completely airtight, a balloon filled with helium gas was connected during measurements performed outside the glovebox, to compensate for gas leakage. The main leak seemed to be at the top of the cell, between the stainless steel base of the crystal and the membrane.

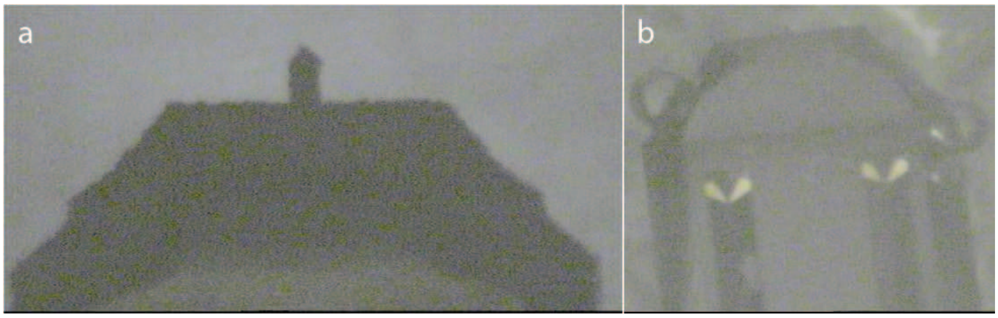

Figure 4.17 – Contaminated cell. (a) probe with layer formation in cell; (b) probe with bubbles and oxidized lithium foil.

4.5.2 Towards electrochemical experiments in a modified AFM system

Based on all the previously discussed results, a description will be made on how the modified AFM would work. For each step, a reference to the section where that part is discussed in detail will be given.

In the glovebox, the cell will be assembled with an LNMO sample (or any other active material) at the bottom, functioning as a working electrode (WE), and metallic lithium foil at the side, working as a reference electrode (RE), (Subsection 4.3.1). Before assembly, every part will be dried in the vacuum oven, including the probe to be used (Subsection 4.4.1). The cell will then be placed in the AFM. The gas flow and electrical connectors and the AFM head will be installed (Subsections 4.2.1 and 4.3.1). At this time the AFM and Maccor hardware/software are already operational.

A manual approach of the tip is done, followed by resonance and aiming and finally the computer drives the last part of the approach to the substrate (Subsection 4.2.1, Subsection 4.4.1). The probe will then make topographic line scans of the substrate and is subsequently retracted from the surface, so that it won't short circuit the system (Subsections 4.2.1 and 4.4.1). Now the probe can be prelithiated using the metallic lithium (RE), i.e. the cell of silicon vs. lithium will be discharged galvanostatically to 0.3V (Subsections 4.2.2 and 4.3.1). Right afterwards, the cell is switched to potentiostatic mode and the voltage between silicon and lithium is kept at 0.3V (Subsections 4.2.2 and 4.4.1).

A three-electrode setup is then made, in which the voltage of silicon vs. lithium is kept constant and LNMO can be cycled vs. silicon (Subsections 4.2.2 and 4.4.1). This could probably be done using the Maccor to control LNMO vs. silicon and using a large silicon/lithium battery to control the probe voltage vs. lithium (Subsection 4.4.1). The tip can now repeat the scan lines previously made, but at a certain distance from the substrate (Subsections 4.4.1). At the same time, the current between LNMO and Si is being measured, as this provides information of the rate of lithium ion transfer in the cell (Subsection 4.4.1). In this manner the whole sample can be scanned. Afterwards the current data lines can be overlaid to obtain a 2D figure of the current at all the locations (Subsection 4.4.1). This image could then be com- pared to the topographic image to see if enhanced or reduced surface reactivity is related to objects, e.g. catalysts, at the surface (4.4.1).

In an even more advanced system the AFM will be connected to an Electrochemical Impedance Spectrometer.

4.6 Conclusions and Recommendations

In this research project, a silicon AFM probe was successfully used as an electrode in a Lithium-ion battery setup. This was proven by electrochemical curves and SEM pictures. In two-electrode experiments of silicon vs. metallic lithium, it was found that the capacity of the probe was very low, hence dis- charge rates of 3 μA were used. A voltage of 0.3 V was chosen for potentiostatic operation, because most probes show a pseudo-plateau (due to Li alloying) at this voltage.

Moreover, such a tip was proven to allow a AFM scan on a LNMO sample (Fig 4.13)

In AFM experiments, a three-electrode setup with a LNMO sample as working electrode would be preferred. Ideally, simultaneous control of both LNMO vs. Si and Si vs. Li would be needed in this system. A working three- electrode setup with LNMO as WE, Si as CE and Li as RE was achieved, using the Reference Control mode of the Maccor (S4000) cycler.

It was found that it is possible to prelithiate probes and store them in ambient conditions, so as to use them in a later stage. However, for storage times in the order of a month, SEM pictures do show bending of the cantilever and formation of crystals on the probe.

The obtained electrochemical results were not very reproducible and showed significant noise. This resulted from poor electrical connections of the AFM cell. The initially observed side reactions with moisture and air could be prevented by predrying all the setup parts, including the probe, and controlling the environment with an inert gas.

A topographical scan of LNMO with a lithiated probe was also accomplished. This indicates that these probes can be used for further measurements.

Moreover, it was also possible to scan a similar LNMO sample immersed in liquid electrolyte with a normal (non-lithiated) probe in the AFM cell.

It is highly recommended to further improve the quality of the electrical connections when continuing with this research with the electrochemical AFM cell. This would make the results much more stable, reliable and reproducible. In more detail, the side wires should then be replaced by a stronger wire or metal strip. The hooks should be reshaped to apply more mechanical pressure on the sample. The clips should be thoroughly cleaned to remove oxidation or, better, new clips should be made. Ideally, all these parts should be made of platinum to produce a robust and corrosion-free system.

The ideal way to combine topographic and electrochemical data is to make topographic line scans and repeat these at a certain distance with a lithiated tip. A convenient distance for this has to be found.

As further proof that this system works (as it is expected to), it would be interesting to make an approach of Si vs. LNMO while measuring the current. There should be an increase in the current for short separation distances. Also it would be interesting to know what the electrochemical response is in the case of short circuiting, by touching the surface with the probe, while applying a voltage. This method can be used to study the safety of the various electrode materials on a nanometer scale.

When the system will be ready to work, the next step would be to increase the resolution. The tip size should remain as small as possible, while containing enough lithium. It might also be necessary to coat the tip with an insulating material, to obtain a better diffusion profile. Furthermore, it might be worth considering placing the AFM inside a glovebox or to put a portable glovebox around the AFM. This would significantly decrease the chance of contamination although, unfortunately, would make the handling of the system harder.

Nevertheless, we think it is possible to make a modified AFM for in situ electrochemical characterization. Topographical data would be collected in the first run of the sample by a non-lithated tip. A second run at fixed distance from the surface with a lithiated tip would then provide data on the rate of ion transport. By combining these data, we strongly believe it should be possible to relate surface artifacts, e.g. a coating, to increase the ionic conductivity.

Following these problems and the lack of results it induced, several expert teams in AFM and SECM, including manufacturers of those devices, have been contacted to come up with a solution. Unfortunately, so far, it is impossible to operate a combination of AFM-SECM setup due to the organic media of the electrolyte, which would degrade the cantilever.

Due to the fact that not sufficient data were obtained to justify the electrochemical results, chapter 5 will describe structural and surface characterization techniques in order to analyse the charge transfer phenomenon.

References

1. al, K.e., *Analytical Chemistry, 2nd edition.* 2004.

2. University, L., *Principle of Scanning probe microscopy.* (http://www.physics.leidenuniv.nl/sections/cm/ip/projects/thermo/rost/STMTech/Principle_of_SPM.htm.).

3. Vidu, R., F.T. Quinlan, and P. Stroeve, *Use of in situ electrochemical atomic force microscopy (EC-AFM) to monitor positive electrode surface reaction in organic electrolyte.* Industrial & Engineering Chemistry Research, 2002. **41**(25): p. 6546-6554.

4. Bruker, *Nanoscale charge transport in LED materials using conducting AFM.* 2010.

5. Matsuo, Y., R. Kostecki, and F. McLarnon, *Surface layer formation on thin-film LiMn2O4 electrodes at elevated temperatures.* Journal of the Electrochemical Society, 2001. **148**(7): p. A687-A692.

6. NT-MDT, *Electrochemical measurements: Instruction Manual.* 2011.

7. Sun, P., F.O. Laforge, and M.V. Mirkin, *Scanning electrochemical microscopy in the 21st century.* Physical Chemistry Chemical Physics, 2007. **9**(7): p. 802-823.

8. Bard, A.J., et al., *Chemical Imaging of Surfaces with the Scanning Electrochemical Microscope.* Science, 1991. **254**(5028): p. 68-74.

9. Holder, M.N., et al., *Combined scanning electrochemical-atomic force microscopy (SECM-AFM): Simulation and experiment for flux-generation at un-insulated metal-coated probes.* Journal of Electroanalytical Chemistry, 2005. **585**(1): p. 8-18.

10. Macpherson, J.V. and P.R. Unwin, *Combined scanning electrochemical-atomic force microscopy.* Analytical Chemistry, 2000. **72**(2): p. 276-285.

11. Kalinin, S.V. and N. Balke, *Local Electrochemical Functionality in Energy Storage Materials and Devices by Scanning Probe Microscopies: Status and Perspectives.* Advanced Materials, 2010. **22**(35): p. E193-E209.

12. Fermin, D.J., *Nanoscale probing of electrode surfaces by scanning force microscopy.* Chimia, 2006. **60**(11): p. A789-A794.

13. Davoodi, A., et al., *Developing an AFM-Based SECM system; Instrumental setup, SECM simulation, characterization, and calibration.* Journal of the Electrochemical Society, 2008. **155**(8): p. C474-C485.

14. Sklyar, O., et al., *Numerical simulation of scanning electrochemical Microscopy experiments with frame-shaped integrated atomic force microscopy-SECM probes using the boundary element method.* Analytical Chemistry, 2005. **77**(3): p. 764-771.

15. Bauer, S., et al., *In operando study of the high voltage spinel positive electrode material LiNi0.5Mn1.5O4 using two dimensional full-field spectroscopic imaging of Ni and Mn.* Physical Chemistry Chemical Physics, 2015. **17**(25): p. 16388-16397.

Chapter 5: Surface and structural studies

$LiNi_{0.5}Mn_{1.5}O_4$ (LNMO) is nowadays one of the most interesting variant of $LiMn_2O_4$ due to its high stability and capacity. Higher power applications, however, require higher charge- and discharge rates. Lithium transport inside the particle has been shown to be a fast process and, instead, ionic and electronic transfer from the electrolyte into the bulk, or vice-versa, seems to be the rate limiting factor. We saw that a good combination would be an ordered LNMO spinel having the $F_{d\text{-}3m}$ structure, with particle size in the order of microns. The high voltage at which it operates the material also is subject to dissolution of manganese. To avoid this reaction, coatings are found to be efficient, as well as to enhance the charge carrier transfer through the surface. In the meantime, doping, and especially with chromium, showed a significant improvement of the structural stability. In this chapter, we will compare pristine LNMO, Cr-coated LNMO and Cr-doped LNMO to have a better understanding and overview of the effect of Cr on the performance of this LNMO. All materials produced were characterized by SEM, EDX, XRD, XPS and electrochemical measurements. It will be shown that chromium doping has no effect on the spinel structure and that it has a number of benefits on the performance of the cell.

5.1 Introduction

During the last two decades, Li-ion technology has developed widely, winning over other energy storage solutions for small applications. Only in the past few years, the phenomenon also spread to larger applications, including EV, HEVs, as well as military and aerospace, to name a few.

As thoroughly developed in the literature, LNMO is one of the most interesting materials for Li-ion batteries positive electrodes, due to its high stability, high capacity and the intrinsic rate capability of its 3-dimensional lithium migration in the lattice [1, 2].

However, the presence of Mn^{3+} ions during the cycling causes several drawbacks, namely capacity fading, Jahn-Teller distortions [3, 4], dissolution of the material into the electrolyte [5-7] and electrolyte decomposition [8]. The use of Mn^{4+} as a source of manganese and Ni^{2+} as a source of nickel greatly helps suppressing Jahn-teller distortions, while using coatings on LNMO particles has been shown to prevent spinel dissolution and corrosion reactions [9-13].

As concluded in chapter 2, larger particles seem to have a higher rate capability, strongly pointing at the fact that the rate limiting process is the lithium transfer properties between the electrolyte and the bulk, and not the ion or electron transport in the particle. The reactions occurring at the electrode/electrolyte interface need to be studied in order to further enhance the performance.

Despite the fact that doping (substitution of cations) or coatings have shown good results, it is still of importance to understand the role of a surface coating and the nature of its layer and determine if a partial or full layer is needed. Among other species, chromium oxides have been studied for their applications in industry [14-16]. In this study, the focus is made on their catalytic behaviour for electron transfer and conduction [17-23]. Moreover, chromium (III) has already been used to prevent the direct contact between $LiMn_2O_4$ and the electrolyte, by increasing the Mn^{4+} concentration at the surface [7], therefore reducing the dissolution of manganese and the electrolyte oxidation.

In the previous chapter, we saw we were unable to fully analyse the charge transfer phenomenon at the interface between the LNMO and the electrolyte. To do so, in this chapter, we propose an extensive study of different LNMO samples combined with a decoration layer of chromium. The focus will be on electrochemical results by using several structural techniques.

5.2 Experimental

$LiNi_{0.5}Mn_{1.5}O_4$ (LNMO) and $LiNi_{0.42}Mn_{1.5}Cr_{0.08}0_4$ (LNMOCrO) powders were synthesized using a Carbon Combustion Method. Stoichiometric amount of Li_2CO_3, Mn_3O_4, Cr_2O_3 and NiO together with carbon black (Li:C molar ratio = 4:1) were mixed and ground manually for 10 minutes prior to ball milling in a planetary ball-mill (Fritsch P-0150) for 30 minutes at maximum speed. The mixture was first heated up to 950°C at 2°C/min and kept there for 12 hours. A second heating step at the same temperature was used to force the powder to cool down slowly to room temperature in 48 hours in order to ensure adequate oxygen uptake. The particles have a particle size of 1–10 μm and a specific surface area of 0.32 m^2/g. For the XAS measurements, $LiNi_{0.42}Mn_{1.5}Cr_{0.08}O_4$, a specific member of the general material $LiCr^{3+}{}_zNi^{2+}{}_yMn^{3+}{}_{1-2y-z}Mn^{4+}{}_{1+y}O_4$ with $0 < z < 0.5$ and $0 < y < 0.5-z$, has been investigated. For z=0 and y=0 one has $LiMn_2O_4$ (LMO) and for z=0 one has $LiNi_{0.5}Mn_{1.5}O_4$ (LNMO). The $LiCr_{0.08}Ni_{0.42}Mn_{1.5}O_4$ material will be referred to hereafter as LNMO-Cr.

LNMO-Cr has a molar mass of 182,15 g/mol and a theoretical capacity of 135,36 mAh/g (11,8 mAh/g from Mn^{3+}/Mn^{4+} and 123,6 mAh/g from Ni^{2+}/Ni^{4+}). The conversion of Mn^{3+}/Mn^{4+} takes place between 5.0 and 4.3 V vs Li/Li^+ and the conversion of Ni^{2+}/Ni^{4+} takes place between 4.3 and 4.9 V vs Li/Li^+, more specifically, Ni^{2+}/Ni^{3+} between 4.3 and 4.7 V and Ni^{3+}/Ni^{4+} from 4.7 to 4.9 V.

The active material LNMO-Cr has been coated on an aluminium current collector (14 mm) with the composition: LNMO-Cr/CB/G/PvdF 84/4/4/8 by mass (CB=carbon black C45, G=graphite KS4, PvdF=Solef 21216). The coating has a loading of active material of approximately 25 mg/cm^2.

The thin layer materials have been prepared by Electro-Hydro-Dynamic Atomization (EHDA) following the parameters of Table 1

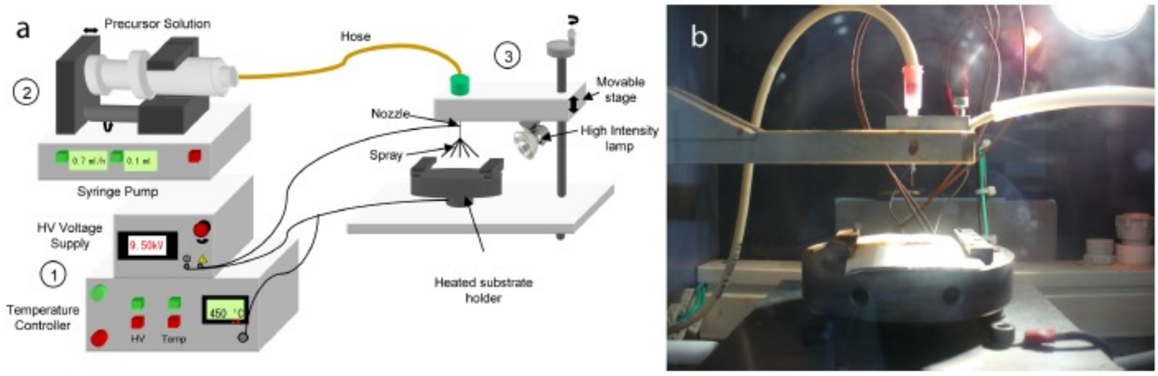

Schematic drawing (a) and photo (b) of the electrostatic spray deposition setup used for the direct synthesis and assembly of the thin layer LNMO positive electrodes. The nozzle, feeding hose and the heated substrate holder are clearly visible. The halogen lamp helps with the visualisation of the spraying mode.

Table 1 : optimized set of experimental parameters

Voltage (kV)	Molar concentration (M)	Flow rate (ml.h-1)	Nozzle (mm)	Temperature (°C)	Annealing temperature (°C)	Distance (cm)
8-9	0.05	0.3	20	450	500	2.5

The texture, morphology, particle sizes and thickness of the films have been investigated using a Philips XL20 scanning electron microscope (SEM) operated at 15 kV. Composition and crystalline structure was studied by means of X-ray diffraction (XRD) using a Bruker (AXS D8 Advance) X-ray diffractometer with a Cu-Kα radiation source (=1.5418Å) and by energy dispersive x-ray spectroscopy (EDX) which was coupled to the SEM system and was measured directly after morphology studies. The electrochemical tests for the powder materials were performed using as positive electrode the Cr_2O_3-coated LNMO films, a polyethylene separator (Solupor), few drops of 1M $LiPF_6$ in ethylene carbonate/ dimethyl carbonate (1:1) as electrolyte and metallic Li as anode. PvdF as a binder and Carbon Black as well as graphite were used for conductivity enhancements. Ratios for each cell will be displayed in the Results and Discussion section.

For the thin films, the thin layers were sprayed directly on the stainless steel coin-cell and used as such as a positive electrode, a polyethylene separator , few drops of 1M $LiPF_6$ in EC/DMC (1:1) as electrolyte, and metallic Li as an anode. The cells were assembled in an Ar filled glove box (coin cells in the case of electrodes and pouch cells in the case of the LAR-3D architectured electrodes). Galvanostatic measurements between 3.5 and 4.9 V were performed on a MACCOR S4000 cycler using different gravimetric current densities and C-rates.

In order to correlate the concentration of lithium ions and the content in nickel ions in the charging cell, both ex-situ and in-situ X-Ray Raman spectroscopy were performed on the beamline ID20 of the European Synchrotron Radiation Facility, Grenoble, France. The spectra were measured using an X-ray Raman scattering spectrometer that is equipped with 72 analysers, out of which 24 were used for the measurements owing to the finite opening angle of the electrochemical cell. Figure 5.2 shows the results on the low-energy region of the spectra, composed mostly of Ni, Mn, and Cr M-absorption edges and Li K edge.

Most of the measurements reported here were done in ex-situ conditions owing to the lower signal from the cell in the in operando conditions, as well as eventual discharge of the battery cell owing to the x-ray beam. The results are confirmed by dedicated in operando measurements for the Ni L3 edge for states of charge of 50% and 100%.

The results show that the Ni^{2+}/Ni^{4+} redox reaction takes place through an intermediate stage of Ni^{3+}, in accordance with the results of [24].

5.3 Results and discussion

5.3.1 Structure of the films

XAS measurements

For the ex-situ measurement of the charged electrodes, batteries have been constructed in an Argon filled glovebox using Swagelok type cells with PEEK body, stainless-steel (SS) electrodes (8 mm diameter) and PTFE back and front ferrules. The positive electrode was a disc of 7,94 mm diameter cut from the LNMO-Cr coating, the anode a 6 mm disc of Li- metal (~0.75 mm thick). The anode and positive electrode were separated by 4 layers of Solupor and ~5 pipet drops of 1 M $LiPF_6$ EC/DMC 1:1 (Aldrich) were added.

Initially, one side of the Swagelok cell was tightly closed (SS electrodes + ferrules and nut). Then the battery stack was build and electrolyte added. The second SS electrode + ferrules and nut were added but not tightened directly. The completed cell was first clamped in a spanner compressing the battery stack. While maintaining pressure, the cell was finally closed tightly. Parafilm was wrapped around both ends of the cell as an extra sealing before the cells were removed from the glovebox.

The cells have been charged to specific states-of-charge (SOC) to produce the ex-situ samples. The general test procedure for the Maccor battery tester consisted of 1) a rest step of 30 sec; 2) a constant current charge with 0.2 C- rate to 5.5 V as a standard starting point; 3) a constant current charge step with 0.2 C-rate to a cut-off condition where the capacity reached a value of x C with x=0.25; 0.50; 0.75; 0.875; 1.0. The cells had typical active masses of 13 mg (~1.55 mAh based on a practical capacity of 120 mAh/g).

After the charge procedure finished, the cells were directly inserted in the glovebox and the positive electrode removed. In order to avoid possible shorts and therefor a change in SOC the anode was removed first and pure DMC was inserted in the cell to dilute the electrolyte present. Then the cell was further opened and the positive electrode removed and washed in pure DMC. The washed positive electrode was allowed to dry in the glovebox and subsequently placed in an empty Swagelok cell with a gap of ~4 mm between the SS electrodes. The PEEK cells for the X-ray measurements had specially thin walls of 0.5 mm to lower signal absorption.

7 cells that have been tested for in-situ measurement were made according to the same procedure. However, for some of them, the amount of Li-metal was increased to 5 stacked pieces and 6 layers of separator in order to create a “x-ray transparent” gap between the SS electrodes of ~3 mm. The in-situ cell was fully charged to 5 V with a 0.2C-rate before starting the X-ray measurement.

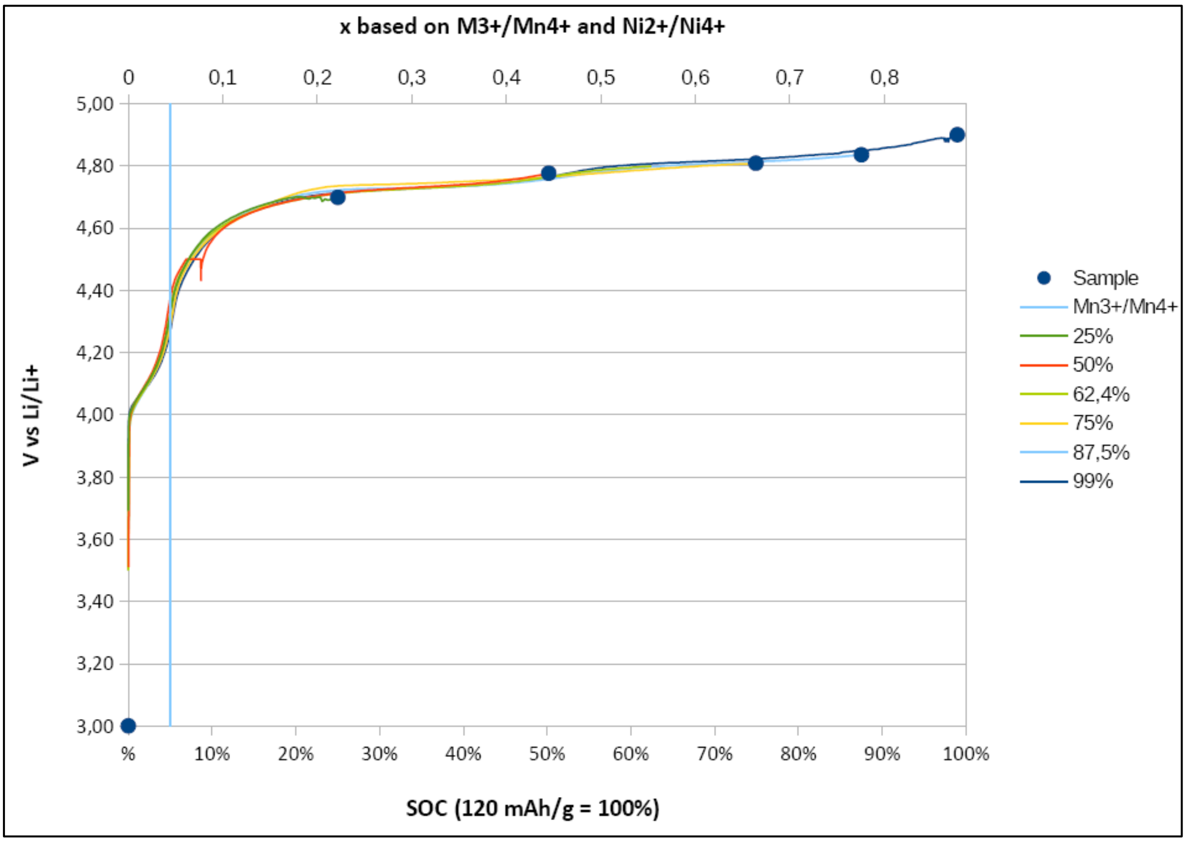

Figure 5.1: *Charge curves of the ex-situ LNMO-Cr samples.*

In Figure 5.1, the different samples measured at different state of charge can be seen (blue points). Those different points correspond to each different data in Figure 5.2. The different line colours indicate a different SoC.

Several cells were charged at different state of charge, in order to obtain a complete overview during the whole charge.

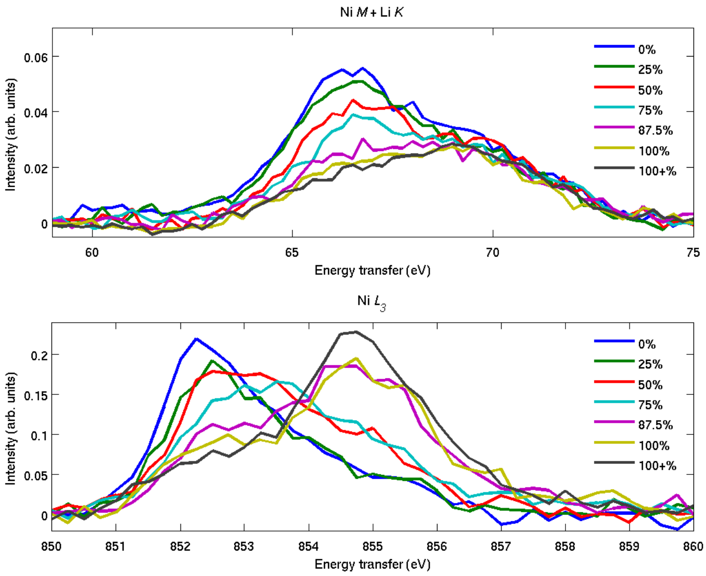

Figure 5.2 : Li edge (up) and Ni edge (down) at different SOC.

Results are shown in Figure 5.2 and 5.3. It is stressed that this technique is unique in its kind as we were able to monitor the change in the Li and Ni signal simultaneously.

From the shifted peaks, it is clear that during the charge, the oxidation state of Nickel is changing first from $^{2+}$ to $^{3+}$ first, then from $^{3+}$ to $^{4+}$. From this result, it has been possible to draw a curve relating the Ni and Li contents (Figure 5.3).

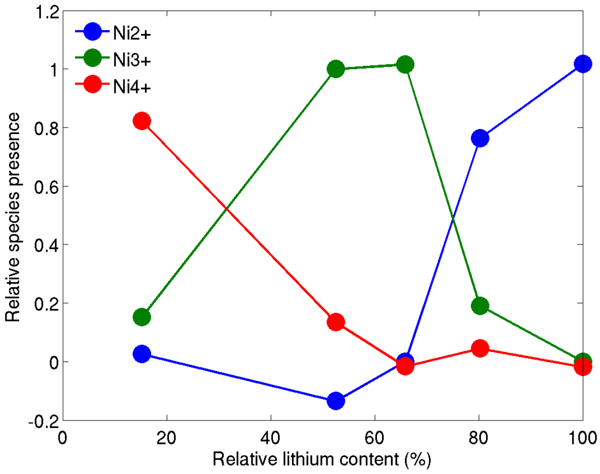

Figure 5.3 : Lithium content versus Nickel content

We can observe clearly that the more lithium is depleted, the higher the content of Ni^{4+} is.

Indeed, the more we progress on the charge curve, the more the content in Ni^{2+} decreases in favour of Ni^{3+}. In a second step, Ni^{3+} decreases and gives places to an all Ni^{4+} content. This trend clearly follows the Li concentration in the electrode.

The goal of the XAS measurement was to study the surface structure of our samples and see if we could correlate the presence of chromium and the effect it has on the performances of the battery.

We were unable to do so and found instead a correlation between the Li and Ni^{2+} contents.

To study the surface, we decided to use the XPS tool. The experiment is described in the next section.

XPS measurements

In order to get better insight in the surface state, XPS measurements were performed on the HIKE KMC-1 beamline in the Helmholtz Zentrum, Berlin, on both pure LNMO (Figure 5.5) and Cr-doped LNMO (Figure 5.6) in that respect, pristine material, pristine in contact with electrolyte but not cycled (OCV) and materials cycled for 1 and 5 cycles were measured.

The peaks of carbon 1s, oxygen 1s, fluorine 1s, phosphorus 2p and manganese 2p are shown.

The C-C bond at 284.4 eV originating from the conductive carbon in the electrode has been used as reference peak and all other spectra are thus shifted accordingly. In the carbon spectra of the pristine sample, the major peaks are located at 284.4, 286.0, and 291.0 eV and those are assigned to the C-C bond of conductive carbon, C-H bond in the binder, and lastly the $C-F_2$ bond in the binder [25]. A noticeable contribution is seen at 295.5 eV and this is ascribed to the $C-F_3$ bond in the binder. The major change happening in the carbon spectra upon cycling is that there is an increase of the signal at around 285.4 eV and 290.3 eV. The signal at 285.4 is ascribed to general C-H bonds, most likely from decomposition of the organic solvent. The peak at 290.3 matches the energy of carbonate species [26]. The changes in the carbon spectra are minimal, the peak at 291 eV shifts to 290.3 eV and this could be due to deposition of carbonates on the surface, which is a typical product of electrolyte decomposition. The two clearly separated peaks at 284.4 and 286.0 eV in the beginning joined together after cycling, meaning an increase of the signal at around 285eV and this is the general bond energy of hydrocarbons and thus strengthen the idea of a SEI formation.

In the oxygen spectra the peak at 529.9 eV is ascribed to the oxygen in the spinel structure and the peak at 532 is from minor C=O contamination. C-O bonds are at 533 eV and $Li_xPF_yO_z$ is around 533-534 eV. The carbon-oxygen species signal increases with cycle number, predominantly by C-O and this is in accordance with the theory of deposited carbonates as also seen in the carbon spectra.

Fluorine spectra remain mainly unchanged, the small shift can originate from the formation of a dipole layer between the bulk and the SEI.

Obviously, phosphor together with oxygen is a clear indicator of the formation of an SEI layer, since the only source of phosphor is from the salt in the electrolyte, and the SEI formation requires incorporating this into the surface of the sample. The existence of only one peak suggests that it is $LiPF_6$ salt trapped in the organic matrix of SEI, since otherwise a dual peak is obtained from $LiPF_6$ and LiF which is known as a salt decomposition product [27].

It is again stressed that the measurements were carried out with samples that have been taken out of the cell and do not contain any electrolyte anymore. Hence, only surface atoms are being measured.

The manganese spectra are virtually unchanged, indicating that it does not take part in any chemical reactions.

Thus, the phosphor and oxygen spectra clearly show evidence of SEI formation on the surface of the electrode. The SEI seems to mainly be composed of organic components containing carbonates and hydrocarbons and does not show any salt decomposition indicating that the salt is stable at the used potentials. Within the accuracy of the measurements, we observe no difference between the pristine and OCV samples, indicating that the decomposition is electrochemically induced and does not evolve during time. Hence, the surface reaction does not occur as soon as LNMO is in contact with the electrolyte. The only difference that was obtained was a small phosphorus peak. This however was already assigned to $LiPF_6$ rather than to LiF or any LixPFyOz, indicating that the phosphorus might come from trapped $LiPF_6$ in the pores of the electrode. It is further stressed that this signal is very small and only visible at long exposure time.

On the F_{1s} spectra, it is clearly visible that the peak induced by LiF at 687 eV is disappearing from the spectra on the Cr-doped material. It clearly signifies that the LiF effect completely disappears when chromium is present. Hence the ionic and electronic transport at the interface between the electrode and the electrolyte is allowed. It is a strong sign of the chromium effect on the overall performances of the cell.

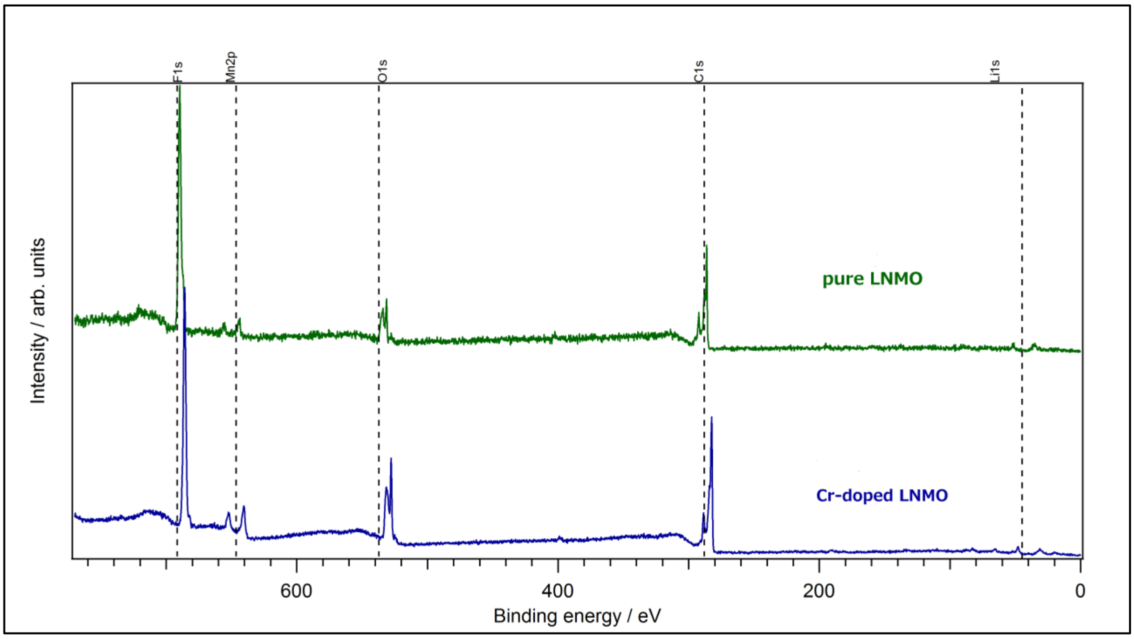

Figure 5.4: Summary spectra of LNMO and Cr-doped LNMO.

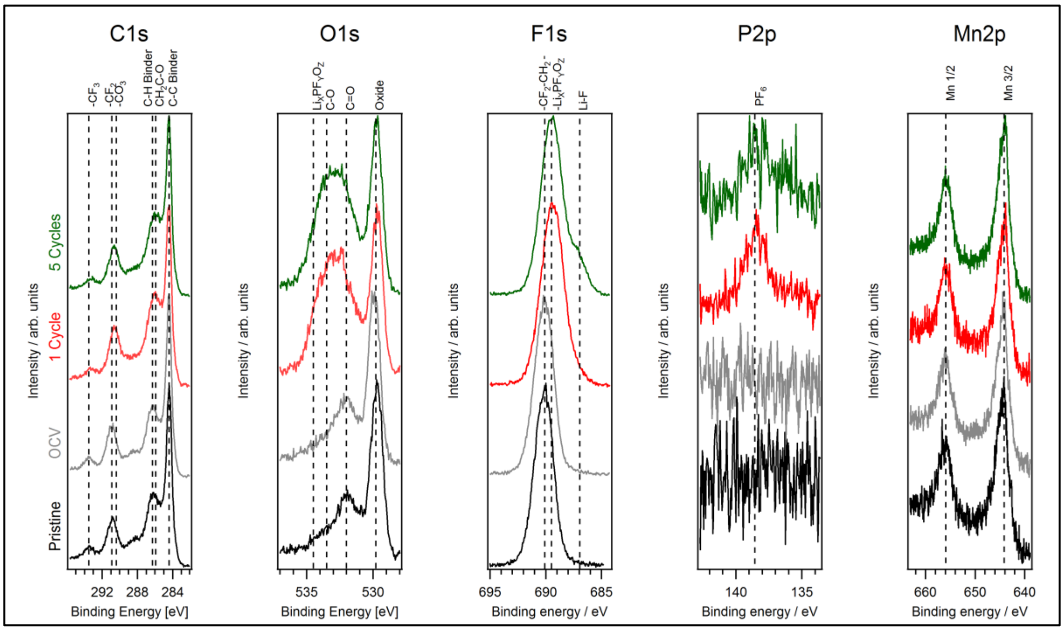

Figure 5.5 : XPS spectra of pure LNMO sample. Evolution is shown from bottom to top. Pristine (black line), material soaked with electrolyte or OCV (grey line), material after 1 cycle (red line) and material after 5 cycles (green line).

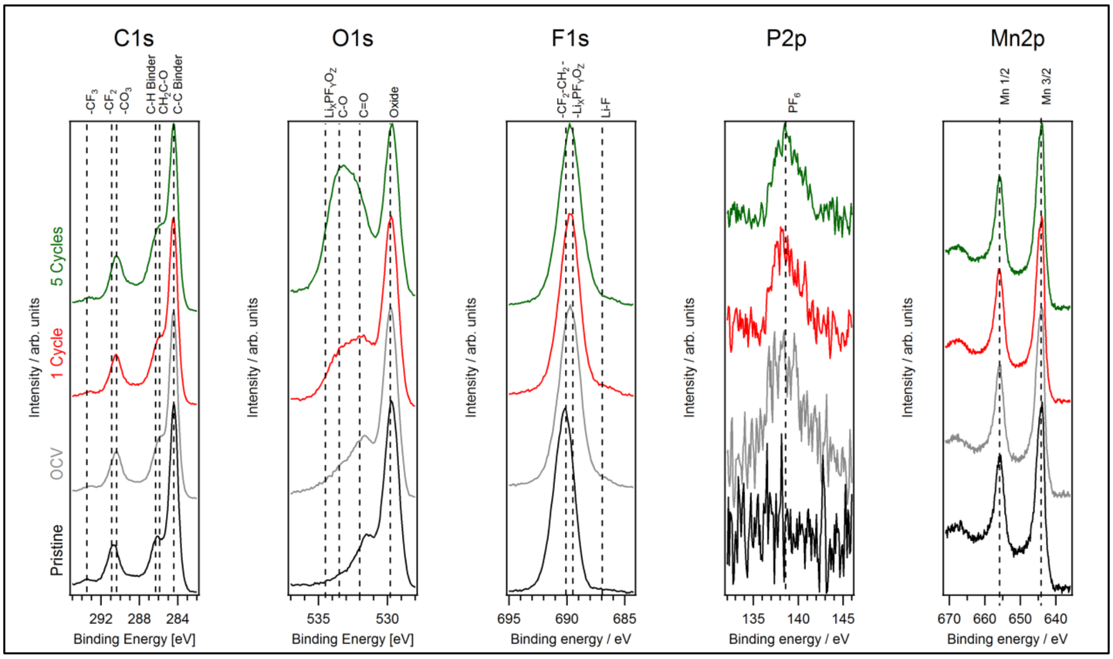

Figure 5.6 : XPS spectra of Cr-doped LNMO sample. Evolution is shown from bottom to top. Pristine (black line), material soaked with electrolyte or OCV (grey line), material after 1 cycle (red line) and material after 5 cycles (green line).

Hence, it can be concluded that a SEI is formed, consisting mostly of organic decomposition products on both the Cr-doped and the pure LNMO spinels. The doping transition metal has no effect on the formed SEI, which is only formed when the batteries are cycled, and not before that.

This could mean that the change, which occurs after chromium doping, doesn't come from the surface of the material but directly from the bulk material, which is in accordance with respective results from electrochemical measurements (see 5.5.2), EDX and XRD results, as well as with XAS measurements done at DUBBEL beam line ID20 and data from the group.

XRD

Figure 5.7 shows the XRD patterns of pure LNMO and Cr-doped LNMO powders. We do not observe any additional reflections in the pattern of the Cr-doped sample. Else the relative intensities are very similar in both patterns, indicating that Cr doping does not induce structural changes. To find out where the chromium is, EDX measurements were performed and the results are shown in Figure 5.9.

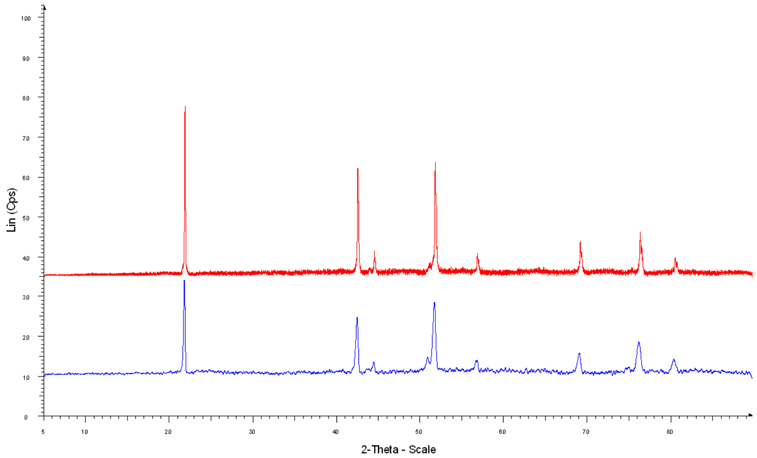

Figure 5.7 : XRD patterns of pure LNMO (red) and $LiNi_{0.42}Mn_{1.5}Cr_{0.08}O_4$ (blue) powders

Figure 5.8 shows SEM micrographs of the sprayed samples. The increasing coverage by Cr_2O_3 can be observed over the flat LNMO layer. When the spray time goes up, there is a clear augmentation of chromium oxide agglomeration, as well as of the density per area unit.

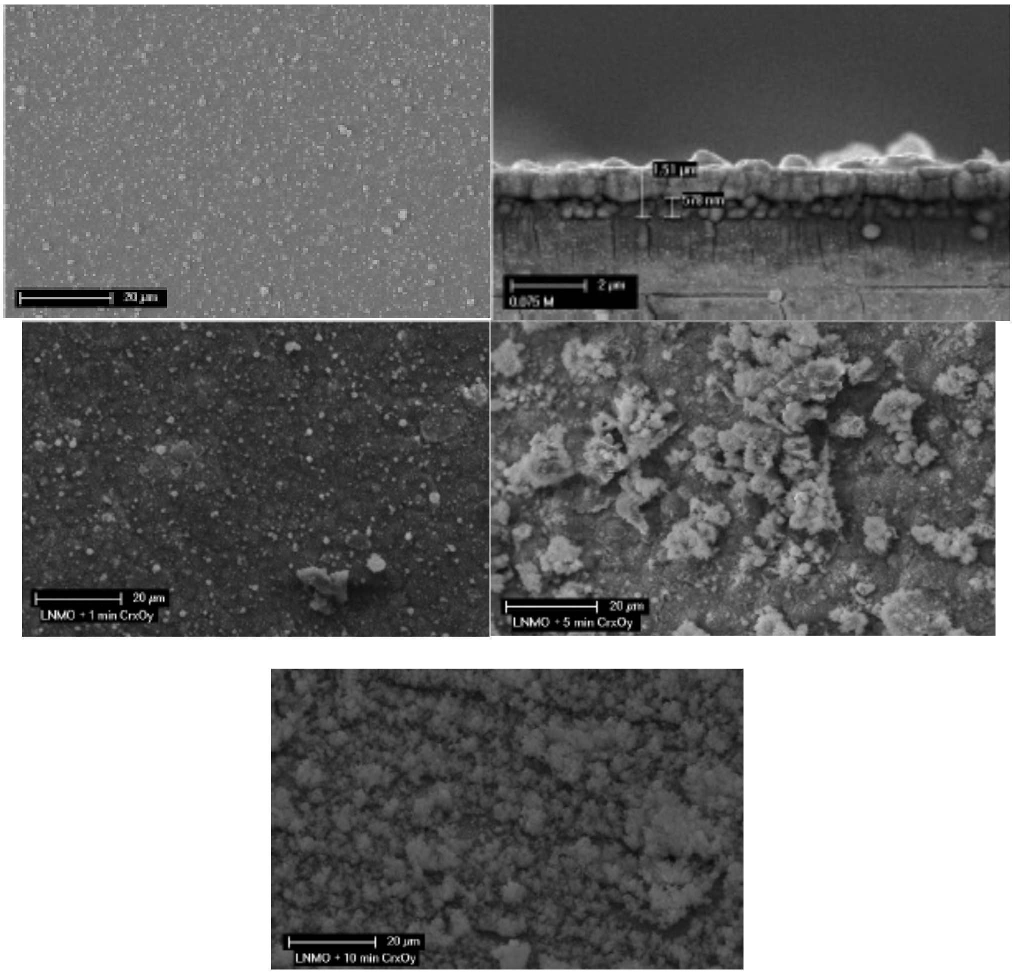

Figure 5.8 : SEM pictures of bare $LiNi_{0.5}Mn_{1.5}O_4$ films without coating + cross section (top) ; with Cr_2O_3 coating for 1min (left); 5min (right); 10min (bottom) sprayed materials.

In order to prove the presence of chromium, SEM coupled with EDX elemental mapping was performed. Figure 5.8 and 5.9 show the pictures of the sprayed Cr_2O_3-coated LNMO. The coverage of chromium throughout the surface of the LNMO film is shown to be very homogeneous.

The Ni and Mn dispersion were measured and these are also evenly distributed.

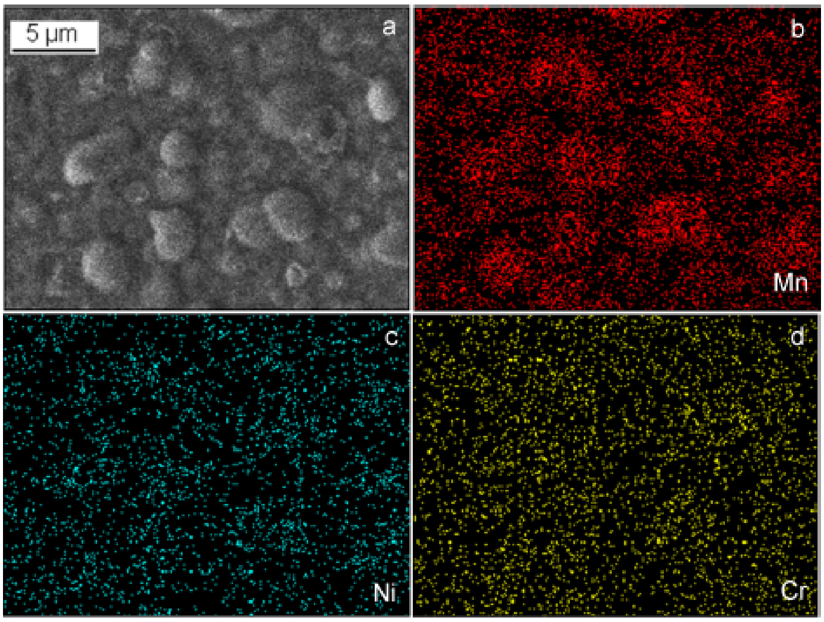

Figure 5.9 : SEM image and corresponding EDX elemental mappings for the 1mn Cr_2O_3-coated sprayed $LiNi_{0.5}Mn_{1.5}O_4$

A similar measurement was performed on the Cr-doped LNMO powder. In Figure 5.10, crystals between 5-10 um can be observed. It is also clear that the distribution of each element is homogeneous. In the middle of the pictures is shown a broken crystal. In order to demonstrate that Cr distribution is everywhere the same, not only at the surface, but also in the bulk. A striking result is the uneven distribution between the Ni concentration. It can be attributed to the cooling process of the carbon combustion synthesis, where elements are recombined together, which could induce such a difference in homogeneity.

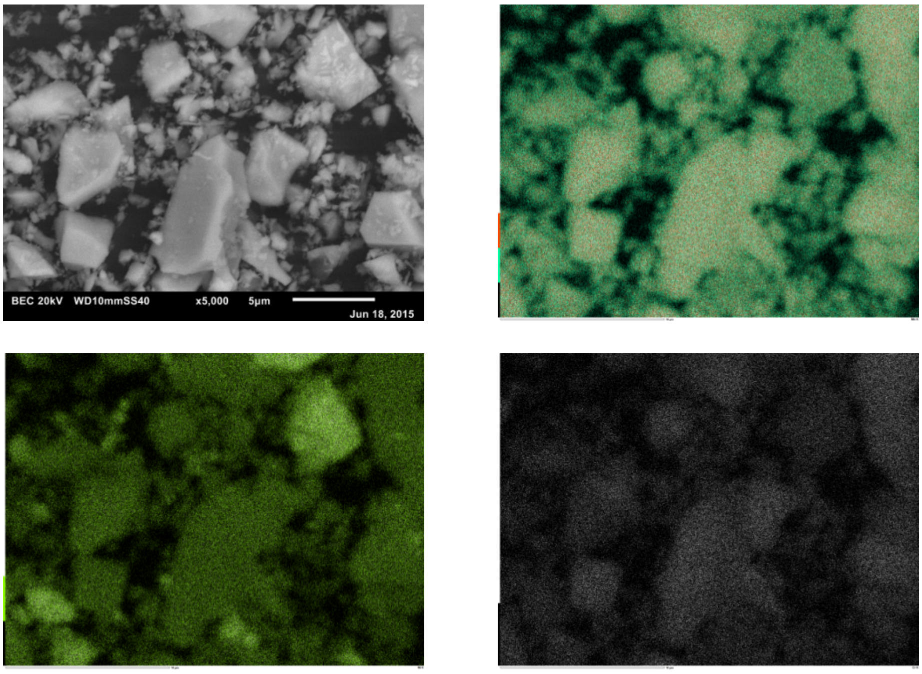

Figure 5.10 : SEM image and corresponding EDX elemental mappings for the $LiNi_{0.42}Mn_{1.5}Cr_{0.08}O_4$ powder. A crystal has been broken by ball-milling (in the middle of the picture) to show the even distribution of Cr in the whole material.

5.3.2 Electrochemical behaviour

The various samples have all been assembled into CR2330-type coin cells with lithium metal as counter electrode and commercial LiPF6 in EC:DMC (1:1) electrolyte. All sprayed materials are pure and contain no binder or other additive. The Cr-doped LNMO has been mixed with PvdF and carbon black, following the ratio : 80 wt% active material/12 wt% PvdF/8 wt% carbon black.

Figure 5.11 compares the different materials at different current densities (1C =147 mA.g^{-1}) between 3.5 and 4.9V versus Li. The cells were charged at 0.1C and then discharged at different C rates.

It is clear that only the Cr-doped sample shows well defined plateaus related to the oxido-reduction of Ni^{4+} to Ni^{2+} (around 4,7V) and Mn^{4+} to Mn^{3+} (around 4.1V), even at high discharge rates.

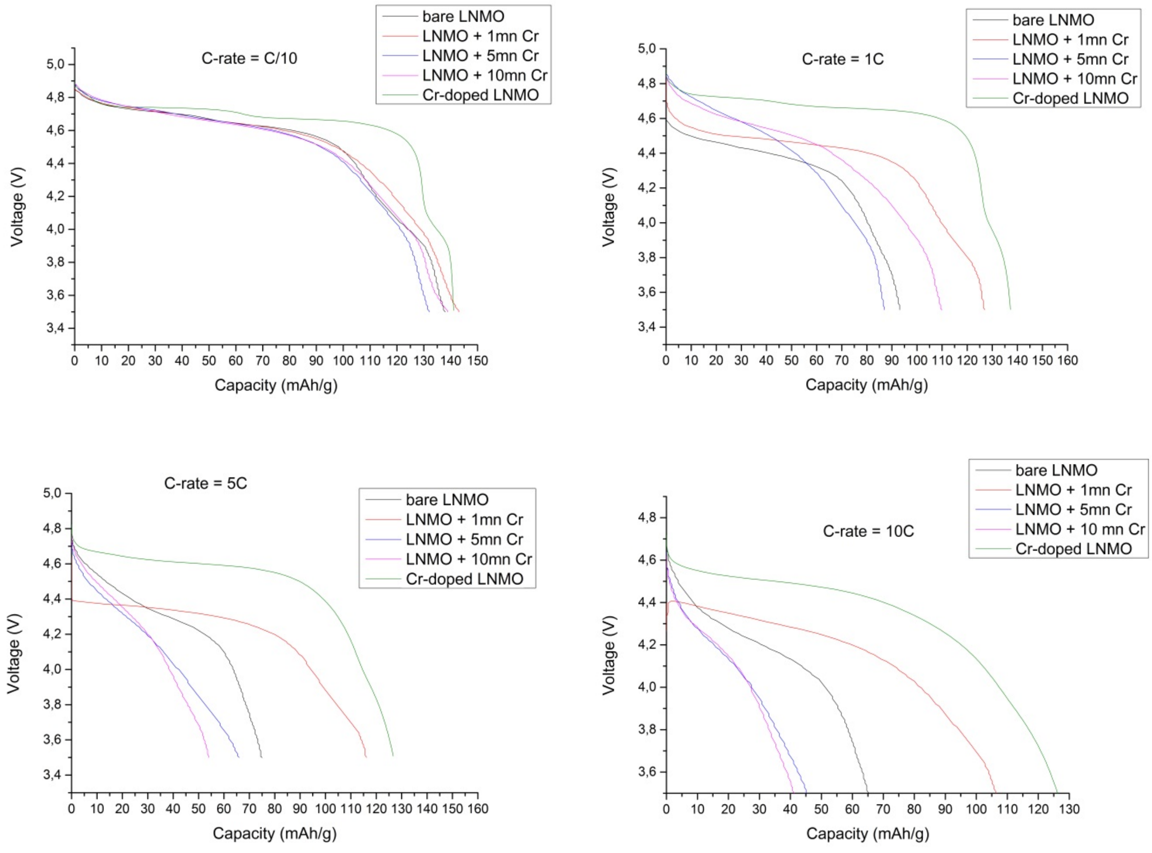

Figure 5.11 : Discharge curves of LNMO before and after coating with Cr_2O_3, as well as Cr-doped LNMO

The reason for not obtaining the two high voltage plateaus might be due to a too high internal resistance of the electrode. Indeed, for the sprayed materials, there has been no carbon added to increase the electronic conductivity.

For the sprayed samples, the discharge capacity is rapidly decreasing as the discharge rate increases. Also when the spraying time for chromium is increased, a significant capacity reduction is observed. Apparently the Cr_2O_3 coating is blocking the electrons or ions, leading to a huge capacity loss. It is stressed that this loss is mainly reversible and is observed only due to a huge ohmic loss. However, this trend is not observed in the Cr-doped LNMO, due to the synthesis method. Indeed, the chromium, which acts as a catalyst {to be published}, is mixed directly with all the other compounds and thus cannot form an insulating layer, as seen for the sprayed samples.

Liu et al [12], demonstrated the increased rate capability and retention for all surface modification cases in their study. They suggest that the reduction of surface-layer and charge-transfer resistances induces this performance enhancement. Surface oxide coatings normally degrade the kinetics of the charge-transfer reaction by blocking the surface of the material. In our case, the opposite happens. The surface oxide coatings are promoting the charge transfer reaction by preventing the SEI layer to grow on the surface of the material.

It is well known that the spinel structure of LNMO allows a fast lithium insertion and de-insertion reaction [28-31].

An epitaxial growth of Cr_2O_3 that adopts the spinel structure of the positive electrode material would act as catalyst {to be published} for reactions occurring at the interface, while, as it is inactive towards the species in the electrolyte, it prevents the formation of an SEI layer. Hence it improves the ionic exchange from the electrolyte to the positive electrode material.

It is however stressed that an optimum amount of chromium oxide must be present to allow a proper ratio between its catalytic and its insulating natures.

5.4 Conclusion

The structure of the samples before and after coating exhibit reflection characteristics only of the LNMO cubic spinel structure for all samples, indicating that the surface modification does not change the crystallographic structure of the initial positive electrode. However, Cr_2O_3 seems to be present homogeneously throughout the surface of the positive electrode film, as suggested by elemental mapping, instead of the active sites initially intended. XRD and EDS results, together with XAS information from similar experiments, suggest the formation of an epitaxial Cr_2O_3 spinel type coating. As this coating seems to be homogeneous, it opens the possibility of using LNMO-based positive electrodes with such modified surface together with conventional electrolyte. The epitaxial growth of a Cr_2O_3 coating, that takes the spinel structure of the underlying positive electrode, act as a catalyst for electrochemical processes occurring at the interface while, at the same time, as it is inactive towards the organic species in the electrolyte, it hinders the formation of an SEI layer improving the ionic exchange from the electrolyte into the active material (XPS) enhancing the battery performance. Nevertheless, an optimum amount of Cr_2O_3 surface modification must be present as a good relation is needed between its catalytic activity (while, at the same time, helps at suppressing SEI layer formation) and its insulating nature.

We possess now an overall knowledge of the mechanisms occurring in the cell, electrochemically, as well as in the structure.

References

1. Amine, K., et al., *Preparation and electrochemical investigation of LiMn2-xMexO4 (Me : Ni, Fe, and x=0.5, 1) positive electrode materials for secondary lithium batteries.* Journal of Power Sources, 1997. **68**(2): p. 604-608.

2. Zhong, Q.M., et al., *Synthesis and electrochemistry of LiNixMn2-xO4.* Journal of the Electrochemical Society, 1997. **144**(1): p. 205-213.

3. Gummow, R.J., A. Dekock, and M.M. Thackeray, *Improved Capacity Retention in Rechargeable 4v Lithium Lithium Manganese Oxide (Spinel) Cells.* Solid State Ionics, 1994. **69**(1): p. 59-67.

4. Thackeray, M.M., et al., *Structural fatigue in spinel electrodes in high voltage (4V) Li/LixMn2O4 cells.* Electrochemical and Solid State Letters, 1998. **1**(1): p. 7-9.

5. Jang, D.H. and S.M. Oh, *Effects of carbon additives on spinel dissolution and capacity losses in 4V Li/LixMn2O4 rechargeable cells.* Electrochimica Acta, 1998. **43**(9): p. 1023-1029.

6. Aoshima, T., et al., *Mechanisms of manganese spinels dissolution and capacity fade at high temperature.* Journal of Power Sources, 2001. **97-8**: p. 377-380.

7. Sahan, H., et al., *Effect of the Cr2O3 coating on electrochemical properties of spinel LiMn2O4 as a positive electrode material for lithium battery applications.* Solid State Ionics, 2010. **181**(31-32): p. 1437-1444.

8. Gao, Y. and J.R. Dahn, *Correlation between the growth of the 3.3 V discharge plateau and capacity fading in Li1+xMn2-xO4 materials.* Solid State Ionics, 1996. **84**(1-2): p. 33-40.

9. Sun, Y.K., et al., *Electrochemical performance of nano-sized ZnO-coated LiNi0.5Mn1.5O4 spinel as 5 V materials at elevated temperatures.* Electrochemistry Communications, 2002. **4**(4): p. 344-348.

10. Sun, Y.K., C.S. Yoon, and I.H. Oh, *Surface structural change of ZnO-coated LiNi0.5Mn1.5O4 spinel as 5 V positive electrode materials at elevated temperatures.* Electrochimica Acta, 2003. **48**(5): p. 503-506.

11. Alcantara, R., et al., *X-ray diffraction and electrochemical impedance spectroscopy study of zinc coated LiNi0.5Mn1.5O4 electrodes.* Journal of Electroanalytical Chemistry, 2004. **566**(1): p. 187-192.

12. Liu, J. and A. Manthiram, *Improved Electrochemical Performance of the 5 V Spinel Positive electrode LiMn1.5Ni0.42Zn0.08O4 by Surface Modification.* Journal of the Electrochemical Society, 2009. **156**(1): p. A66-A72.

13. Noguchi, T., et al., *Effect of Bi oxide surface treatment on 5 V spinel LiNi0.5Mn1.5-xTixO4.* Journal of Power Sources, 2007. **174**(2): p. 359-365.

14. Berdahl, P., *Pigments to Reflect the Infrared Radiation from Fire.* Journal of Heat Transfer-Transactions of the Asme, 1995. **117**(2): p. 355-358.

15. Kitsunai, H., et al., *Transitions of Microscopic Wear Mechanism for Cr2o3 Ceramic Coatings during Repeated Sliding Observed in a Scanning Electron-Microscope Tribosystem.* Wear, 1991. **151**(2): p. 279-289.

16. Bhushan, B., G.S.A.M. Theunissen, and X.D. Li, *Tribological studies of chromium oxide films for magnetic recording applications.* Thin Solid Films, 1997. **311**(1-2): p. 67-80.

17. Weckhuysen, B.M. and R.A. Schoonheydt, *Olefin polymerization over supported chromium oxide catalysts.* Catalysis Today, 1999. **51**(2): p. 215-221.

18. Spitz, R., *Supported Chromium Oxide Catalysts for Olefin Polymerization .9. Nature of Narrow Gamma-Phase Esr Signal and Its Correlation with Catalytic Activity.* Journal of Catalysis, 1974. **35**(3): p. 345-352.

19. Miessero.Kg, *Nature of Active Sites of Supported Chromic Oxide Polymerization Catalysts.* Journal of Catalysis, 1971. **22**(3): p. 340-&.

20. De Rossi, S., et al., *Chromia/zirconia catalysts with Cr content exceeding the monolayer. A comparison with chromia/alumina and chromia/silica for isobutane dehydrogenation.* Applied Catalysis a-General, 1998. **167**(2): p. 257-270.

21. Myers, D.L. and J.H. Lunsford, *Silica-Supported Chromium Catalysts for Ethylene Polymerization - the Active Oxidation-States of Chromium.* Journal of Catalysis, 1986. **99**(1): p. 140-148.

22. Abu-Zied, B.M., *Structural and catalytic activity studies of silver/chromia catalysts.* Applied Catalysis a-General, 2000. **198**(1-2): p. 139-153.

23. Wang, S.B., et al., *Dehydrogenation of ethane with carbon dioxide over supported chromium oxide catalysts.* Applied Catalysis a-General, 2000. **196**(1): p. 1-8.

24. Bauer, S., et al., *In operando study of the high voltage spinel positive electrode material LiNi0.5Mn1.5O4 using two dimensional full-field spectroscopic imaging of Ni and Mn.* Physical Chemistry Chemical Physics, 2015. **17**(25): p. 16388-16397.

25. El Ouatani, L., et al., *Effect of Vinylene Carbonate Additive in Li-Ion Batteries: Comparison of LiCoO2/C, LiFePO4/C, and LiCoO2/Li4Ti5O12 Systems.* Journal of the Electrochemical Society, 2009. **156**(6): p. A468-A477.

26. Younesi, R., M. Hahlin, and K. Edstrom, *Surface Characterization of the Carbon Positive electrode and the Lithium Anode of Li-O-2 Batteries Using LiClO4 or LiBOB Salts.* Acs Applied Materials & Interfaces, 2013. **5**(4): p. 1333-1341.

27. Lin, X.K., et al., *A Comprehensive Capacity Fade Model and Analysis for Li-Ion Batteries.* Journal of the Electrochemical Society, 2013. **160**(10): p. A1701-A1710.

28. Hwang, B.J., R. Santhanam, and S.G. Hu, *Synthesis and characterization of multidoped lithium manganese oxide spinel, Li1.02Co0.1Ni0.1Mn1.8O4, for rechargeable lithium batteries.* Journal of Power Sources, 2002. **108**(1-2): p. 250-255.

29. Ohzuku, T., M. Kitagawa, and T. Hirai, *Electrochemistry of Manganese-Dioxide in Lithium Nonaqueous Cell .3. X-Ray Diffractional Study on the Reduction of Spinel-Related Manganese-Dioxide.* Journal of the Electrochemical Society, 1990. **137**(3): p. 769-775.

30. Kobayashi, S., et al., *XANES and EXAFS analysis of nano-size manganese dioxide as a positive electrode material for lithium-ion batteries.* Journal of Materials Chemistry, 2004. **14**(12): p. 1843-1848.

31. Shokoohi, F.K., J.M. Tarascon, and B.J. Wilkens, *Fabrication of Thin-Film Limn2o4 Positive electrodes for Rechargeable Microbatteries.* Applied Physics Letters, 1991. **59**(10): p. 1260-1262.

Chapter 6 : Summary- EuroLiion project

Development of EVs for the transport sector is high on the list of EU priorities for economic recovery within the framework of the Green Car Initiative. Most work to date has focused on technical development and market analyses. Important challenges will also be faced in terms of durability, safety, cost and the required charging infrastructure.

Although conventional Li-ion cells have become widespread, some have too low energy density for transport applications. Others are either too expensive or do not meet environmental or safety standards. The EU-funded project 'High energy density Li-ion cells for traction' (http://www.euroliion.eu/ (EUROLIION)) focused on developing novel Li-ion batteries that combine high energy density, low cost and enhanced safety. Benefits were obtained through a change in materials. The new cell has an innovative silicon (Si) anode (negative electrode), novel low-cost salts, and a modified iron or manganese/nickel-based cathode (positive electrode).

These electrode materials are cheaper and can store higher charge densities than the conventional electrodes. In addition, they require a higher operating voltage to increase cell energy density.

Scientists defined new formulations for synthesising nano-Si materials for the negative electrode, and different binders and additives. The produced Li-ion cells with a positive electrode that includes a combination of lithium, nickel and manganese demonstrated stable cycling. With a novel well-purified salt as an electrolyte, the nano-Si electrodes showed satisfactory capacity retention. More lithium salts were also synthesised, tested and even further purified since some were found to degrade the positive electrode.

Objectives and outcome of the EuroLiion project

This section includes the system integration activities with the following objectives:

- making the decisions for the project milestones;
- test procedure selection for performance and safety assessment;
- support the development of new material and the integration in prototype and large cells;
- specification for HEV Heavy duty trucks and EVs;

- dissemination of the results.

In the end the following objectives have been realised:

- making the decisions for the project milestones, i.e with respect to system definition:
  - the electrolyte salt was be distributed rather than the electrolyte solution
  - a negative electrode with commercial nano-Si was selected, rather than with nano-Si from TUDelft due to too much gas formation during production
  - a commercial electrolyte was selected due to better stability and compatibility towards the selected LNMO
  - for the cathode material, the TUDelft material (LNMO) was selected;
- test procedure selection for performance and safety assessment

System definition

Battery materials used in the demonstrator cells – In summary, the 1st generation cells contained Si versus $LiFePO_4$ (LFP) with an electrolyte of 1M $LiPF_6$ in EC/DMC/DEC. The 3rd generation cells contained Si vs LNMO with an electrolyte of $LiPF_6$ in EC/DMC/DEC. The 2nd generation cells were not made as we were not able to stabilize the new LiTDI salt-based electrolyte against the LNMO cathode - unfortunately, this new salt as used in the electrolyte was not compatible with our cathodes foreseen in the consortium's lithium ion cells.

In both generation cells, the Si used had a particle size of 100-150nm. For the cathode material, LFP and LNMO had particle sizes of 100nm and 5000nm, respectively. The voltage versus metallic Li and the specific capacity for those materials were 3.3V and 150mAh/g, and 4.8V and 120mAh/g, respectively.

Electrode composition – The 1st generation cells were 18650 cells, whereas the 3rd generation cells were pouch cells. A more detailed description is given at the fabrication of the cells.

The anode composition was 150nm Si (69%), CMC (7%), Graphene (11%), PAMA/SBR (~3%), and Citric acid/sels (~8%).

The cathode composition was 5µm LNMO (92%), PvDF (4%), SuperP (2%), and VGCF (2%). It is stressed that the LNMO material has been produced by EuroSupport, Uden, NL according to the recipe developed within the consortium.

Test Procedure definitions and methods

The procedure as foreseen aimed to provide the full details required to create a procedure to assess Si-based cells on performance, including abuse testing. Several items have been described, where a procedure was developed aiming to provide full details required to analyse and characterize the developed cell in terms of operational performance, efficiency, and durability (calendar- and cycle life).

Negative electrode formulation

Objectives and outcome in short

Objectives in terms of performances was mentioned earlier. However, the capacity of the new Si negative electrode cannot be less than 1500 mAh/g following 500 cycles at C/5, by the end of the project, electrodes loading being in the range of today's energy Li-ion technology. For that purpose, the objectives have been broken down into well-defined objectives:

- prepare and test commercial Si and other Si-based materials with various structures (e.g., 2D structures, amorphous Si) and compositions (e.g. Zintl's phases);
- prepare, optimize and test alternative binders to CMC;
- increase the power density through the use of electron conducting binders and doped Si;
- address the volumetric capacity issue by tuning the porosity;
- study the Si degradation mechanisms during cycling.

In the end the following objectives have been realised:

- nano-Si powders produced via the LA-CVP technique have been delivered to various partners for further processing;

- Si powder delivery from commercial suppliers rather than from TUDelft;
- a formulation for Si coating has successfully made and supplied to CEA for implementation in WP6;
- prepare and test commercial Si and other Si-based materials with various structures (e.g., 2D structures, amorphous Si) and compositions (e.g. Zintl's phases);
- preparation and optimization of Si electrode formulation with CMC as a binder;
- preparation, optimization and testing alternative binders – e.g. alginate ;
- addressing the volumetric capacity issue by tuning the porosity;
- studying the Si degradation mechanisms during cycling;
- an overview of various (reported) Si materials has been given with regard to size and morphology.

Investigation of aging mechanisms of Si electrodes

A bibliographic review has been written on the aging mechanism of Si electrodes and contains the following items:

- effect of particle size;
- Si/C Composite;
- binder effect - formulation / composition;
- Li Insertion mechanism;
- effect of cycling procedure;
- the problem of coulombic efficiency *vs* electrolyte degradation;
- the surface chemistry of Si electrode studied by XPS;
- commercial Si.

Li NMR studies have focused on understanding the difference between micron sized, 150 nm and 15 nm Si. We have completed a study of the 150 nm Si (33:33:33 CMC:C:Si) composition. The local structure formed on cycling is similar to that seen for micron Si (Key et al. *J. Am. Chem. Soc.*, 131, 9239, 2009) but the kinetics of lithiation is easier. In summary:

- $Li_{15}Si_4$ formed on discharge to 0V, indicating that it is important to use a cut-off voltage of

>50 mV. The behaviour is different from the 15 nm Si where no $Li_{15}Si_4$ is seen and the atomic/electronic structure and nature of the clusters are different.

- ^{29}Si NMR studies are on-going to obtain more structural information about the nature of the clusters. 1D NMR spectra have been collected.
- FEC/VC studies were performed and the synthesis of ^{13}C enriched electrolytes were initiated to allow for more detailed SEI studies. Preliminary syntheses with non-enriched starting materials were performed to produce EC.

Synthesis of new Si particles and their characterization

TUDelft has produced crystalline Si nano-particles (SiNP) (Figure 6.1) with laser assisted CVP.

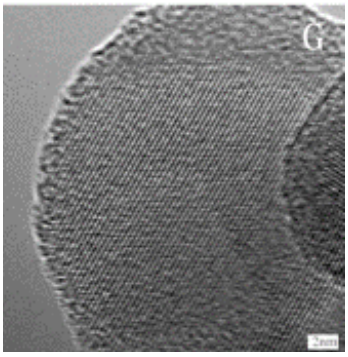

Fig. 6.1. SiNP showing the crystallinity and the oxygen surface.

Several batches of about 30 g of the above material have been delivered to partners for further analyses and processing. The production rate that has been achieved so far is about 50-100 g/day. During the research it was found that the SiNP can be collected without any air exposure avoiding any contamination of the Si surface. However, once exposed to air (moisture) it starts to react violently. It was already known that an oxygen layer on Si surfaces seems to be essential for good Si/Binder interactions, therefore the SiNPs are allowed to oxidize only at the surface by accepting a small leak in the set-up. These Si active materials are characterized in terms of morphology and composition by BET, XRD, TEM, and EDS. The particle size can be controlled by the laser power applied. The particle size is roughly 20 nm with a small size distribution as calculated by proper analysis of the BET, XRD and TEM results.

The most surprising result concerns the nature of the Si surface made at TUDelft. Despite the very high surface area of this Si (> 110 m^2/g), it contains less than 7% of Si dioxide. EDS measurements show small amounts of oxygen, of which most is coming from adsorbed CO_2 – a common phenomenon found in EDS analysis.

Electrochemical tests were performed on these casted films according to the following procedure: 1st cycle, current at C/50, voltage range of 50 mV to 0.9V, followed by consequetive cycles recorded with a current at C/10 and a voltage range of 175 mV to 0.9V. The active material was 0.75 mg in these pouch cells.

Development of new associations of Si with binders and carbons

The Si-binder system was analysed in an in-situ cell with Small Angle and Wide Angle X ray Spectroscopy (SAXS/WAXS). Modelling of the preliminary measurements shows a Si particle size of 10nm diameter (before lithium insertion) which is in good agreement with the TEM results. Furthermore, the WAXS data illustrates the feasibility of monitoring the particle crystallinity during charge and discharge. It seems, that during the Li-uptake and donation the CMC binder loses its partially crystallization.

CNRS-LRCS and CEA identified a strong reactivity of Si with water leading to hydrogen gases coming from the electrode slurry. This reaction does not allow a homogeneous and smooth casting of the Si electrode at CEA scale (100 meter of electrode need to be deposited). This reaction is due to the oxidation of Si with water according to the following reaction:

$$Si + 2H_2O \rightarrow SiO_2 + 4H_2.$$

At CNRS-LRCS, we have demonstrated that the hydrogen production is enhanced when the temperature increases and decreased at low pH value. The consequences of these measurements are some modifications of the electrode processes at CEA. In order to suppress the formation of hydrogen gases, we have produced a small, dense and protective layer of SiO_2 at the surface of the Si powders by thermal treatment of Si powder at 400°C during 2 hours. Higher temperatures produced to a too high SiO_2 layer whose consequences are very poor electrochemical properties. This thermal treatment has been implemented at CEA.

Besides, there was an interest to explore a new binder: PAA-g-PEO. The behaviour of the binder has been analysed by comparison with the state-of-the-art CMC binder. In order to optimize the electrode behaviour, various mass ratios and compositions have been tested. Despite these preliminary results, it seems that the new binder have certain potential.

Formulation of defined association of particles / binder for better cycleability

A first formulation with optimised slurry rheological properties and stability, and improved conductive additive (carbon black) distribution thanks to the use of a dispersant was released earlier. Formulation 1 (Si 66%, Citric acid 15.5%, CMC 6.8%, AcB 10.1%, PAMA 1.7%) with AM loading 2.5mg/cm² achieves at C/5: 370+/-45 cycles at 1200mAh/g_Si

(790mAh/g_electrode ⇔ 3mAh/cm²) with LP30+10%FEC+2%VC electrolyte, coulombic efficiency 98.5+/-0.5%.

A second formulation with modified conductive additive (exfoliated graphite nanoplatelets, which is a cheap graphene) was released at month 18. Formulation 2 (Si 66%, Citric acid 15.5%, CMC 6.8%, Graphene 10.1%, PAMA 1.7%) with AM loading 2.5mg/cm² achieves at C/5: 200 cycles at

1800mAh/g-Si (1200mAh/g-electrode, agreeing with 4.6mAh/cm²) with LP30+10%FEC+2%VC electrolyte, coulombic efficiency 99.85+/-0.1%.

Moreover, we made full cells with a Si electrode (Formulation 2) and a LNMO electrode, and we showed, if the Si electrode is fully lithiated/delithiated vs Li metal before the full cell assembly, a full reversible cycling for 50 cycles. In this case, the electrolyte contained only FEC as the additive.

Initially, it was noticed that during manufacture of the electrode gas (hydrogen) evolution took place resulting in an inhomogeneous coating. This however was solved by pre-oxidising the Si at 400 °C, and, hence, proper coatings were produced in the end.

Compatibility of the new electrolytes with the Si electrodes - Effect of additives

Initially, the optimized formulation has been tested on their the electrochemical performances of the Si-electrodes using conventional two electrode Swagelok cells with different liquid electrolytes:

- a 1M $LiPF_6$ solution in an EC-DMC mixture;
- a 1M $LiPF_6$ solution in an EC-DMC mixture with VC and FEC additives;
- a 1M LiTDI (salt from Warsaw) solution in an EC-DMC mixture;
- a 1M LiTDI (salt from Warsaw) solution in an EC-DMC mixture with VC and FEC additives.

In parallel, electrochemical tests were performed with the 33/33/33 composition with $LiPF_6$ EC-DMC as reference but also with different concentration of LiTDI in EC/DMC in coin cells configuration. The polarisation of Si electrodes observed with 1M LiTDI electrolyte has been reduced thanks to the optimisation of the ionic conductivity of the electrolyte.

Other parallel tests showed that the best cycling is with FSI-salt and $LiPF_6$ with VC. However, the SiOxFy compound formed on the surface of the Si particles as a function of cycling is also formed with the use of the FSI salt.

Furthermore, we studied the cycleability of Si electrodes based on the Si purchased by CEA with the following formulation Si(33%), CMC(33%) and Csp(33%) and with four different electrolytes: LP30 ($LiPF_6$ in EC/DMC), LP30 with additives (2%VC and 10% FEC), LiTDI (LiTDI in EC/DMC) and LITDI with additives (2%VC, 10% FEC). Electrochemical cycling tests were performed without any capacity restriction. We can observe that whatever the salt $LiPF_6$ or LITDI, the capacity strongly decrease when no additives are used and this capacity retention is strongly improved when VC and FEC are added in the electrolyte. When LiTDI is compared with LP30, the capacity retention are very similar. It is vital that this LiTDI is strongly purified in order to obtain good quality results. It is also important to recall that LiTDI doesn't contain any fluor atoms so the battery safety will be strongly improved since the major sources of toxic gases emitted during a battery fire is hydrofluoric acid. The conductivity of $LiPF_6$ is typically 11mS/cm, and decomposes between 65-80°C. It further hydrolyzes so as to form HF. LiTDI does not generate HF, and has typically a conductivity of 6.7 mS/cm, and is stable in water and up to 250°C. Unfortunately, above 4.6V is showed significant degradation in electrochemical cells. Nevertheless, against Si it showed to be very stable. It however, required additives to perform adequately, such as FEC. Despite the required existence of FEC, aging of the LiTDI electrolyte in contact with Si occurs. This phenomenon is still not fully clear.

Electrolyte formulation

Objectives and outcome in short

- Synthesizing and analyzing new battery electrolytes based on an imidazole salt.
- Use of only one salt in the optimized mixture of solvents.
- Ionic conductivity of the electrolyte of minimal $5mS\cdot cm^{-1}$ and lithium transference number of 0.4.
- Cycling ability and electrolyte-electrode compatibility with both electrode materials.

In the end the following objectives have been realised:

- the equipment (glove box) was installed and infrastructure built;
- synthesis of the salt in the volume able to fulfil the requirements of the Partners in WP4;
- test Optimization of the electrolyte;
- materials sent to partners;
- detailed instruction with procedure of electrolyte preparation and purification;
- optimization of the electrolyte;

- compatibility test with anode showed good performance;

- compatibility test with cathode showed poor performance;

- preparation and submission of scientific papers together with other partners of EuroLiion.

Electrolyte formulation and testing

In summary, the recommended electrolyte solution is EC/DMC (1:2) 0.31 mol/kg LiTDI. However, for better performances at lower temperatures, the suggested solution will be EC/DMC/DEC (1:1:1) 0.5 mol/kg LiTDI. The solubility in battery grade solvents like cyclic and linear carbonates (DMC, DEC, EC, PC) is very good, i.e. at least a concentration of 2M can be reached. Obviously, the salts are also very soluble in water and forms actually very stable complexes, which allows even a certain water concentration in the electrolyte used as this will then scavenged the moisture. This was further confirmed when using a 6mole% water concentration in a commercial electrolyte where no reaction was observed with a lithium metal electrode. However, it is still highly advised to keep it as dry as possible to minimize the moisture influence on other eventual parasitic reactions.

In the end, around 80 different compositions were tested. Most of the compositions reached the values of the conductivity and transference numbers required in the project, i.e. ~4-5 mS/cm and 0.5 respectively. Moreover, several discussions led to the conclusion to use stabilising agents such as FEC and VC**.** This will be done outside the context of EuroLiion.

Compatibility with negative electrode

The results have been tested along other tasks, but are anyhow summarised here as follows:

- without capacity limitations, the cycle life is strongly affected by the mechanical resiliency of the electrode;

- without FEC, TDI electrolyte shows poor performance. Adding FEC (Novolytes) improves the TDI electrolyte performance.

- when Si is cycled with capacity limitations, TDI is much worse than $LiPF_6$, but without capacity limitations, TDI is slightly worse than $LiPF_6$;

- the highest capacity (3000mAh/g over 70 cycles) was found with Si based anodes for the electrolyte EC/DMC (1:2) 0.31 mol/kg LiTDI+2% VC+10%FEC. An important improvement for LiTDI was obtained with the additives VC and FEC on the capacity retention. LiTDI+VC+FEC (Aldrich) based electrolytes offers a better capacity retention than LP30, however this additive is responsible for a significant polarisation effect. LiTDI + VC + FEC (Aldrich) based electrolytes offers a poorer capacity retention than LP30 +VC +FEC;

- without additives we obtained a reversible capacity for nano Si composite anodes of about

  900mA/h by using EC/DMC (1:2) 0.63 mol/kg LiTDI electrolyte for over 500 cycles

In addition, water treated Si electrode have been analysed as well. In summary:

- in case of LiTDI based electrolyte, a capacity was reached which was inferior to the one with $LiPF_6$ but a better efficiency and cycle life was obtained, currently over 250 cycles and still running;
- the lithiation process of the Si differs significantly from the classical system, which has been

  observed by the very strong differences in the derivatives curves cycled with LiPF6 and LITDI.
- when using LiTDI, the peak at 0.6V in the derivative curve is always absent, and since this peak is

  typically assigned to the formation of Li15Si4, is is most plausible that Li15Si4 is not formed here;

Compatibility with positive electrode

As decided, LNMO will be the cathode material for the 3rd series of prototype cells. In that respect, the LiTDI salt was tested accordingly, with the following results:

- LiTDI salt from WP4 is not working well with the LNMO cathode;
- on the other hand the electrolyte used with the first generation cells (LiPF6 EC-DEC 1:1 + 2% VC

  +10% FEC) is not working well with the cathode due to the VC additive;
- the most efficient electrolyte seems to be: LP30 (EC/DMC 1:1 + LiPF6) + 10% FEC;
- LiTDI works with electrode materials having a potential of <4.5V *vs* Li/Li^+;
- water contamination might be an important degradation source.

Behaviour in full cells

As decided earlier, LNMO would be the cathode material for the 3rd series of prototype cells. Since this LNMO was not compatible towards the LiTDI electrolyte, it was decided not to focus anymore on this subject. Nevertheless, several earlier results reported on real cells consisting of LNMO cathode and Li as anode, showed huge fading. Hence, due to this move, no results of these cells were generated.

Positive electrode formulation

Objectives and outcome in short

The main objective of WP5 will be the development of sustainable, low-cost and safe cathode material, e.g. LFS-F and LNMO.

The objectives are then defined as follows:

- surveying and evaluating the existing theoretical models with respect to electrode behaviour;
- optimization of modified LFP with regard to performance towards high-rate but safe material;
- synthesizing and characterization, with the aim to improve the performance of LFS-F along with

  the knowledge achieved from the other objectives;
- synthesizing and characterization, with the aim to improve the performance of LNMO along with the knowledge achieved from the other objectives;
- defining the positive electrode formulation of the novel viable cathode material;
- assessment and delivery of viable cathode materials;
- defining an adequate process for recycling LMNO.

In the end the following objectives have been realised:

- delivery of 4kg LNMO (produced by EuroSupport) to CEA for cathode electrode making;

- surveying and evaluating the existing theoretical models with respect to electrode behaviour;

- optimization of modified LFP with regard to performance towards high-rate but safe material;

- synthesizing and characterization, with the aim to improve the performance of LFS-F along with the knowledge achieved from the other objectives;

- defining the positive electrode formulation of the novel viable cathode materials;

- assessment and delivery of viable cathode materials;

- defining an adequate process for recycling LMNO;

- Based on survey, a new general model with respect to electrode behaviour was introduced;

- LFS-F was synthesised according to several routes. One route was found suitable for scale-up so 10 g of the material could be delivered on time;

- defining and assessment of the positive electrode formulation of the novel viable cathode material;

- synthesizing and characterization, with the aim to improve the performance of LNMO;

- LMNO with a reversible capacity of ~143mAh/g (theoretical 146.7mAh/g) and a fading of less than 1% after over 100 cycles was successfully synthesised;

- assessment and delivery of viable cathode materials;

- data sheets of the above.

Theoretical investigation of transport in insertion cathodes – impact of nano-architecturing and Composition

A new approach to evaluate charge carrier transport and transfer in insertion cathodes has been developed, based on various simple assumptions. First we divide the whole transport in a cathode into three steps. Secondly, we assume that upon increasing the C-rate, the charge cannot penetrate into the whole active particle but merely to a certain penetration depth. The topography of the moving front is optional. The sharpness of the boundary between the new and initial phase is not very important. Six cathode materials were analysed based on the above theoretical approach. The analysis has revealed the following common features of the studied materials:

- decreasing the particle size below about 200-300 nm, there remain only two main transport steps:

a) the transport of charges from their reservoirs (collector, electrolyte) to the active particles

(wiring step)

b) the transport inside the active particles (solid state transport step);

- the wiring step starts to prevail at an electrode loadings of 10-20 mg/cm^2. An esential part (usually more than 50%) of wiring is the transport of electrons from the current collector to the active mass. The total wiring resistance is between 5 to 20 Ω/cm^2 of the current collector.

This means that the maximum currents that can be sustained when wiring is the limiting step are on the order of 0.1-0.4 A (or 10-40 A/g) in 10 mg electrodes. Practical results published in the literature confirm this estimation. Additionally, due to wiring it is unreasonable to expect much higher current values. So when higher currents are measured one needs to check the results with respect to possible artefacts, e.g. wrong estimation of mass etc.;

- in most materials, the electronic conductivity seems to be better than the electronic one.

This means that optimization of electrode mass needs to be focused on providing sufficient ionic conductivity/supply – such as maintainance of porosity etc.;

- decrease of particle size is the only really effective way to improve the rate performance and also safety at higher power, e.g. prevention of excessive heat generation. However, any agglomeration needs to be prevented in order to exploit the actual benefits of decreased particle size;

- the role of surface decorations is certainly not to decrease the insertion resistance. The latter is already very small in standard nanosized materials. The role is better ascribed to either prevention of agglomeration of improvement of wetting the particles by the electrolyte.

Adjusting LFP-based materials with enhanced rate capability safety

We have addressed the issue of surface decoration from the perspective of transport enhancement. The following conclusions can be made, based on the application of the general transport scheme:

- The impedance of charge transfer through the active surface is much smaller (up to 1000 times) than the impedance due to several other transport steps. This particularly holds for nanometric active materials. Similar results are obtained, regardless if impedance is extracted from impedance spectroscopy of from galvanostatic curves. This result can be viewed as follows: decorating the active surface itself has no sense if our goal is merely to improve the transport of charge through the surface layer;

- indirectly, surface decorations can improve the overall transport if they help wet the active surface area with electrolyte. This can be realised via creating additional micro- or low-end-mesoporosity.

Minute amounts of ceramic additive have been shown to work in the case of nano-titania.

- in some reports, the role of surface decorations could have been misinterpreted, which is the case where the amount of conductive additive is very high;

- there is another, completely different role of surface decorations – the chemical or electrochemical protection against degradation of active material or degradation of other electrode

components (particularly the electrolyte). This particular role was addressed when reporting on the effect of surface decoration of LNMO (see next points);

- during degradation of LNMO due to progressive cycling the impedance of medium frequency arc increases enormously; the other impedance features exhibit moderate or negligible changes;

- the possible effect of the lithium counter electrode was ruled out in two ways – by replacing the counter electrode after certain number of cycles with a fresh one and by making a symmetrical cell without lithium (two LNMO electrodes partly charged and used as anode and cathode);

- a closer analysis of the meaning of medium frequency arc shows that its origin is the contact area between the aluminium foil and the first layer of the electrode composite attached to this foil;

Synthesis and characterization of LFS-F

Tavorite $LiFeSO_4F$ material reversibly intercalates Li+ at 3.6V and displays a sustainable reversible capacity of 140 mAh/g with good rate capability. Besides, it can be prepared at T<300°C by using either ionic liquids or polymers as reacting media or by a ceramic process. Whatever the media used, the reaction involved consists in reacting stoichiometric amounts of LiF and $MnSO_4{\cdot}H_2O$ for time spans ranging from 24 hours (liquid) to 72 hours (ceramics). Nevertheless a crucial step towards the success of these reactions resides in the use of an iron monohydrate precursor free of Fe^{+3}. Several synthesis methods were analysed, and described in more detail below.

For such purpose, the iron monohydrate precursor is made by (i) dissolving stoichiometric $FeSO_4{\cdot}7H_2O$ (Aldrich, 99%) in distilled water under nitrogen bubbling, (ii) adding a pinch of ascorbic acid to convert any Fe^{3+} salts to Fe^{2+} salts, (iii) precipitating the mixed precursor by adding ethanol, (iv) drying the recuperated solid, and finally (v) heating it either using ionic liquid or under vacuum to remove 6 H_2O.

- For ionothermal synthesis, ~1 g of precursor mixture (LiF + $FeSO_4.H_2O$) was mixed with 5 ml of EMI-TFSI inside a Teflon-lined autoclave, stirred for 20 min before slow heating to

280-295 ºC (at 5 ºC/min), and keeping it for 24 h before gradual cooling by switching off the furnace. The reaction product was recovered by washing the ionic liquid twice with ethyl acetate and drying the powder at 60 ºC.

- For solid-state synthesis, the reaction mixture was uni-axially pressed into pellets, loaded inside a Teflon-lined autoclave (in Ar filled glove-box), slowly heated to 290-300ºC (5ºC/min) and annealed for 24-50 h before slowly cooling to ambient temperature. The final product was simply ground in mortar-pestle for further study.

- For polymer synthesis, 1g of precursor mixture (LiF + $FeSO_4.H_2O$) is mixed with polymer powders (i.e. PEG (M_w: 20,000) or PEO (M_w: 250,000)) and the overall mixture is placed inside a Teflon-lined autoclave before heating the bomb at 300°C for 48 hours. For T >60°C the polymer becomes liquid and does not decompose until 320°C.

It is worth noting that the obtained powders, whatever the aforementioned methods, showed comparable electrochemical performances. In contrast, the different processes in terms of scalability differ. Although Ionic liquids can easily be recycled they are very costly. Polymers present advantages in terms of handling, but the powder recovery is cumbersome. So it results that the synthesis of $LiFeSO_4F$ using the solid-state process remains more attractive for large scale production as there are no solvents to store or waste that need to be treated during the process.

Solid state reaction:

- First, $FeSO_4$. H_2O was prepared starting from $FeSO_4$. $7H_2O$ treated with ascorbic acid to eliminate all iron (III) impurities before being heated at **180°C for 1 hour** under 1.5 bar **pressure of Ar flow**.

- Next, the obtained $FeSO_4$. H_2O was mixed with stoichiometric amounts of LiF and ball-milled under Ar using shock machine (Spex) for **15 to 20 min** to obtain a homogeneous mixture. Then, the powder mixture was pelletized in ~0.8g pellets which are placed all together (8 to 10 pellets) in an alumina boat and annealed in a tubular furnace under argon flow (0.5 bars). The furnace temperature was raised to 300°C at a rate of 10°C/min and maintained at this temperature for 48 hours. The resulting materials were single-phased with occasionally minute amounts of $FeSO_4$ powders and had electrochemical performances comparable to those obtained by either ionic liquids or polymeric-based processes. Scaling such a process to kgs batches is now just a problem of dimensioning tubes and furnaces.

Formulation of $LiFeSO_4F$:

Active materials (LiFeSO4F tavorite) are mixed by hand milling in an agate mortar with Super P carbon black in a ceramic mortar for 30 mins. Then PVDF dissolved in NMP solution is mixed with mixture of AM and Csp powder in glass bottle by magnetic stirring for 30min.

Then the slurry is casting on aluminium foil and dried. The charging capacity is quite low at present time due to a non-sufficient optimisation of the formulation. With the increase of Csp, capacity and its retention get better. The optimized formulation ratio is 75 % AM, 15 % Csp and 10 % binder.

Diffusion coefficient of $LiFeSO_4F$

The lithium diffusion coefficient in $LiFeSO_4F$ has been determined by three different techniques namely Galvanostatic Intermittent Titration Technique (GITT), electrochemical impedance spectroscopie (EIS) and Potential Relaxation Technique (PRT). A value of $10^{(-15)}$ cm^2/s was measured for the all three techniques with better precision with PRT. This value is in good agreement with the ones predicted by DFT calculations.

Synthesis and characterization of LNMO

LNMO has acceptable Li-ion and electron conductivities even in micrometer-sized particles, which infer that surface, rather than bulk, kinetics are the predominant factor in charge transfer properties. Hence, we analysed the roles of chromium in a conductive oxide coating and as a bulk dopant in LMNO. LNMO and $LiCr_{0.08}Ni_{0.042}Mn_{1.5}O_4$ were synthesised using a Carbon Combustion Method. In summary, stoichiometric quantities of Li_2CO_3, Mn_3O_4, NiO and Cr_2O_3 (for the preparation of the $LiCr_{0.08}Ni_{0.042}Mn_{1.5}O_4$) were mixed together with carbon black (Li:C molar ratio=4:1) and grinded for 30 minutes with a ball-mill machine (Fritsch P-0150). The mixture was first heated up to 950°C at 2ºC/min and kept there for 12 hours. In a second heating step, the material was allowed to cool down slowly to room temperature in 24 hours for oxygen uptake. To form the chromium oxide layer, LNMO was immersed in an aqueous solution of various concentrations of $Cr(NO_3)_3$. The powders were exposed to the solution for 2 hours. The solution was then placed in a furnace at 120°C for 2 hours to allow the water to evaporate. The remaining powder was rinsed with ethanol, dried again and it was finally annealed at 600°C for 8 hours.

The powders have a BET surface area of 0.32 m^2/g. XRD analyses showed that the powders are mainly phase pure. ICP-OES analyses gave atomic ratio of the Ni and Mn transition metals that agrees well with the intended stoichiometry. The Cr content runs from 0.07mole% to 2.4mole% of the total transition metal content. The layer thicknesses of the coating were then calculated based on the BET surface area, the ratio of the Cr vs. the other transition metals and accepting a density of 5.22 g/cm^3 as taken from Cr_2O_3. Combined SEM and EDX was carried out on the powders, and very nice octahedral crystals with a particle size of 3-5 μm were obtained. EDX analyses showed that the Cr is homogeneously distributed in the sample. It is stressed that this is the case for all samples prepared and tested.

XAS analyses, co-financed by the Netherlands Research Organisation (NWO), was carried out on the Dubble beam line (BM26B) at the ESRF, Grenoble, FR, to measure the change of valences of the various elements during operation (charge/discharge). $Cr\text{-}O_x$ coated as well as doped LNMO was analysed in-situ. The measurements showed that Cr was always +3 irrespective whether it is in the structure on the surface as well as it is independent on the state of charge of the cell. Hence, this may indicate that chromium acts as a catalyst for electrochemical processes occurring at the interface.

The EXAFS region indicates that Cr exists in an octahedral coordination for all the samples (doped / coated / cycled / pristine). Regarding the coated samples, chromium adopts a spinel-type structure of the underlying lattice rather than the typical corundum structure of Cr_2O_3. This could indicate that instead of being only a "coating", Cr is partially "penetrating" into the underlying material.

The electrochemical tests done with commercial electrolyte, showed a small amount of $LiMn_2O_4$ impurity, which is highly reversible in the charge/discharge behaviour. The obtained capacity is ~143 mAh/g (theoretical 146.7 mAh/g), and the fading is less than 1% after over 100 cycles at low rates and about 120 mAh/g at 1C.

In summary, it can be said that:

- optimised doped and coated LNMO with Cr-O was synthesised;
- particle sizes were 5 μm with a specific surface are of 0.32 m^2/g;
- the capacity is about 120 mAh/g (@1C).

In that regard the following batches were delivered to the respective partners :

- the first batch of 30 g were sent to CNRS-IMN at the beginning of 2014;
- a second batch of ~1 kg was sent to CEA mid 2014; (Figure 6.2)
- a third batch of ~4 kg produced by EuroSupport with the TUDelft recipe was sent to CEA.

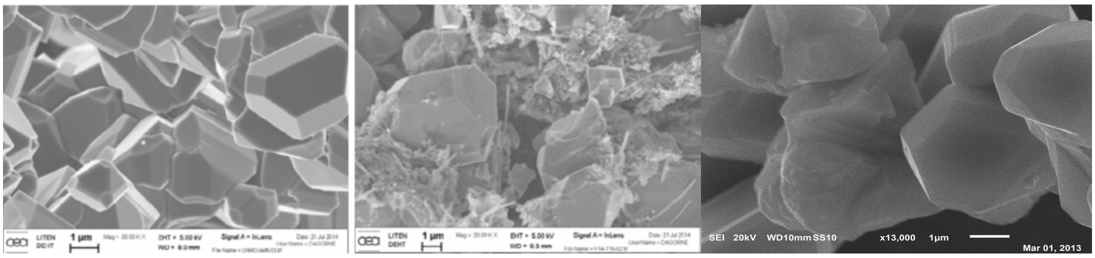

(a) (b) (c)

Fig. 6.2. SEM pictures of batch 2 (a) and batch 3 (c). and the electrode with batch 2 (b).

Optimization of electrode formulation

Different optimized electrode formulations for LNMO were identified. It could be possible to achieve a very good cycleability with these formulations at 8 to 10 mg of LNMO per cm². However, the cycleability of the same formulations but with higher loadings of ~25 mg of LNMO per cm² is still not satisfactory. Let's note that to match a 3mAh/cm² capacity at the negative electrode, 30mg of LNMO per cm² at the cathode is required.

Moreover, we made full cells with Si (Formulation 2) electrode optimised in WP3 and LNMO electrode, which formulation was optimised in WP5, and we showed that if the Si electrode is fully lithiated/delithiated versus lithium metal before the full cell assembly, the LNMO//Si cell shows a fully reversible cycling for 50 cycles. The electrolyte contained only FEC as the additive.

Integration and scaling-up

Objectives and outcome in short

The purpose here is to demonstrate, at a prototype level (representative to the application), that the cell chemistries developed in this project will have a significant gain in energy density compared to the current Li-ion technology and that it can be implemented into cylindrical cells which are thus possible candidates for electrical vehicle use. Active materials and electrolytes developed in the other tasks are integrated into full cell systems in order to manufacture cylindrical cells.

The actual manufacturing was done in 3 steps:

Step 1) Implementation of Si/C composite anode into cylindrical cell applying CEA cell chemistry for $LiFePO_4$.

Step 2) Implementation of new electrolyte into cylindrical cell applying Si/C composite anode and the CEA $LiFePO_4$ cell chemistry.

Step 3) Implementation of new cathode composite into cylindrical cell applying Si/C composite anode and the developed electrolyte.

The goal was to produce 20 working cylindrical cells per manufacturing step. Taking into account scrap rates resulting from the use of new materials, at least 40 cells per step are produced and scrap cells are disposed.

In the end the following objectives have been realised:

- several high power LFP cell have been delivered for testing;
- a formulation has been successfully optimised for use in a semi-industrial coating machine;

- coatings of the Si anode electrode based on “formulation 1 and 2”;
- manufacturing of reference 18650 cylindrical cells LFP/G;
- manufacturing of 18650 cylindrical cells LFP/Si;
- implementation of Si/C composite anode into cylindrical cell applying CEA cell chemistry for LiFePO4 (Step 1);
- implementation of new cathode composite into cylindrical cell applying Si/C (step 3).
- due to incompatibility of the electrolyte with the electrode, step 2 has not been carried out.

Important Notice

During the course of the project, the work for the fabrication of those cells has been taken over by CEA from GAIA. Therefore, for the description of the project results, only work done by CEA has been considered.

Negative electrode fabrication and testing

The work concerned the development of producing Si negative electrode according to formulations created within WP3, where the objective is to achieve an electrode with a capacity of >1500 mAh/g for 500 cycles measured at C/5.

As mentioned earlier at the system definitions, the formulations have been defined and then many trials were carried out at CEA to coat the Si material with a slot-die equipment. The use of high quantities of slurry creasted significant gas evolution that needed to be solved. Finally the pilot line using forward-roll technology was used showing the best compromise in electrode quality (adhesion and flexibility). In parallel, at CNRS-LRCS work on the Si stability in water was done showing that a thermal treatment increased the stability and avoid hydrogen gas formation.

In a next stage, “Formulation 2” was developed containing graphene as conductive additive.

During the trial, slurry rheological properties were optimized with increasing the solid content. The results obtained, show the necessity to incorporate latex to give suppleness to the electrode, as for Formulation 1. No major difficulties were observed during this trial concerning the process scale up of this formulation and good mechanical properties of the electrode were obtained, suggesting that it can be used in the winding step for cylindrical cells manufacturing..

Performances of this electrode versus $LiFePO_4$ have shown a first irreversible capacity of 20% and a Coulombic efficiency stabilized at 99.4% for the best coin cells.

Positive electrode fabrication and testing

In the first period, the positive LFP electrode was produced at CEA with the industrial coating line and a surface capacity of 3 mAh/cm². In the following period, CEA focuses on the scale-up of LNMO formulation develop by IMN with the pilot coating line. First trials with the CEA pilot line have shown that there was too much NMP and drying of the electrode was not sufficient for the high target loading of active material on electrode. A new formulation with less PVDF and less NMP was applied while keeping the same viscosity for the slurry. Hence, the new formulation became: LNMO 92% PVDF 4% SP 2% VGCF 2% .Thus it was possible to reach the target of an electrode coated at high loading with a surface capacity of 3 mAh/cm² (Figure 6.3).

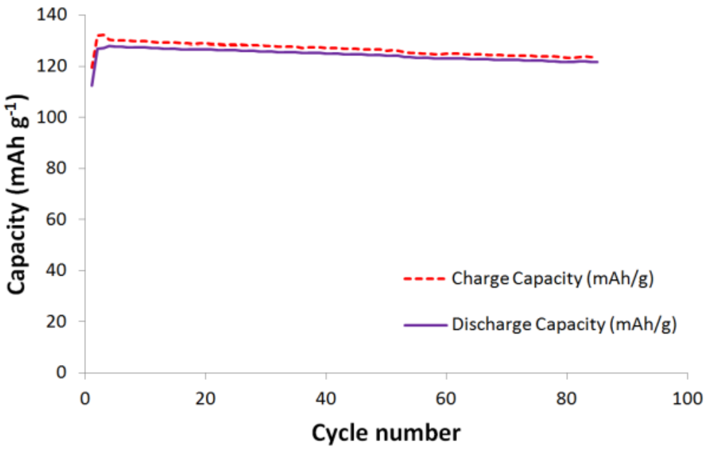

Fig. 6.3 Specific capacity versus cycle of the electrode manufactured at the pilot scale during cycling in half cells versus Li at C/5 between 3.5 and 4.9 Volts.

This electrode showed good adhesion and flexibility to consider for electrode winding and cell assembly

Cell assembling

In the first period, the cell assembly was planned with both LFP and Si “formulation1” electrodes.

The selected cells size was 18650 standard casing.

The CEA cells are assembled with following steps:

- tabs connector welding on both anode and cathode;
- positive / separator / negative electrodes winding;
- wound “jelly roll” insertion in cylindrical cases;
- tabs connector welding;
- electrolyte filling and cell crimping in an Argon filled glove box;
- cell activation.

All these steps (except the last one) operate in dry clean room environment (dew point -40°C).

Standard electrolyte showing good performance with Si was applied: LP30 88% +2% VC +10% FEC (LP30 is EC:DMC 1:1 + LiPF6 1M).

In the next step, CEA focuses on the scale-up of LNMO as cathode electrode and Si "Formulation2". The new electrolyte was also tested with both electrodes, but CEA observed that this electrolyte did not fulfil the requirement mainly at cathode side. LNMO electrode has a low reversible capacity with LiTDI electrolyte probably due to decomposition at high voltage. The corresponding voltammetry curves showed that it was not possible to reach a voltage beyond 4.6V with this electrolyte while a higher voltage is required, i.e. about 4.9V versus Li, for LNMO. It was also observed that VC additive is not stable at high voltage, and thus the best compromise for both anode and cathode cycle life was the LP30 electrolyte with FEC as additive. This electrolyte was then selected for the third generation cells. Due to the poor results of the LiTDI based electrolyte, the realization of the cells LFP//new electrolyte//Si-C were not considered anymore. Even though LP30+FEC electrolyte was identified as the best electrolyte, degassing was identified, probably due to carbonate solvent decomposition at high voltage in the vicinity of EC and DMC. This degassing was observed with 53437 soft packaging cells equipped with a lateral pouch. The swelling of this pouch occurs after the first forming cycle. This degassing should apply equally in 18650 cells and a calculation based on electrode surface ratio and free volume in 18650 cells proofed that the pressure into these cells would be close to the maximum allowable pressure of 15 bar. Then these cells can't be shipped for safety reasons and it was decided to manufacture the third generation cells with the soft 53437 packaging, including two lateral pouches: one to remove the generated gas after forming and the other one for collecting the gas during cycling. Thus, 20 cells were manufactured and send to the other partners for testing. The average discharge capacity of these cells at the first forming cycle was 450 mAh whereas the charge was 675 mAh. It correspond to 33% of irreversible capacity which is more than the 25% expected and calculated with the irreversible capacities of the electrodes measured in coin cells versus Lithium metal.

These cells correspond to an energy density of 140 Wh/kg, but then with two lateral pouches for gas collecting, which obviously increases the total weight of the cells. Remember, the first generation of LFP/Si cells showed an energy density of only 110 Wh/kg, however with another concept, but still it proofs a significant improvement of the capacity compared to existing chemistries.

Testing and benchmarking

Objectives and outcome in short

The purpose here was to develop a testing procedure for the new chemistry cells with the following objectives:

- lifecycle test of prototype cells;

- dynamic modelling of promising battery concepts;

- safety evaluation and safety tests of prototype cells;
- evaluation of new concepts from system level perspective: management of cells when integrated into system.

In the end the following objectives have been realised:

- selection of the commercially available $LiFePO_4$ (LFP) based Li-ion cell;
- definition of the test procedures for benchmarking & life cycle testing and validate;
- reporting benchmarking test results of the LFP cells;
- full vehicle simulation;
- tests for cell modelling to extract necessary model parameters;
- cycle life testing of the prototype cells;
- management development for novel battery prototype (algorithm for estimation of SOC);
- safety assessment and testing (test procedure).

Benchmarking of LiFePO4-cells and prototype cells from GAIA

Three different prototype cells, Graphite/Lithium Iron Phosphate (G/LFP), Si/Lithium Iron Phosphate (Si/LFP) and Si/Lithium Nickel Manganese Oxide (Si/LNMO) were tested and benchmarked the performance following the procedure developed within the EuroLiion consortium. It is stressed that the later prototype cells were manufactured by CEA instead of GAIA as GAIA left the consortium in the middle of the project. The tests concerned formation cycles, energy, power, capacity, efficiency and internal resistance under various operating temperatures.

At least two cells were tested in order to see the consistency of the obtained results. Little deviation from the manufacturer's specification was obtained in general.

Life cycle testing

With respect to the early stage commercial cells arriving from GAIA, the results covered life cycle testing, and the benchmarking tests of the GAIA cells was performed according to the test procedure developed here. Furthermore other commercial LFP-cell were analysed, and performance comparison between conventional LFP-cells and Li-ion batteries was done. Also, simulation and test results from dynamic load cycle efficiency test were verified. In a later stage, the life cycle test results for the prototype cells was the main outcome from this work. Here we evaluated the life cycle performance and reliability of Li-ion cells with Si as negative electrode which was manufactured and supplied by the project partner.

Three types of cells were delivered from the project partner (CEA). The cells consist of LFP and LNMO as cathode, Graphite or Si as anode material. The cycling tests with these prototype cells have been executed at three different temperatures: 0, 23 and 45 ^{o}C and two different state of charge (SOC) ranges: 0-100% and 20-80%.

The capacity fade of the LFP/Si cells over the cycle number (a) and energy throughput (b) was measured, and after running a comprehensive characterization of the cells the life cycle tests are carried out. Results indicate that both temperature and DOD have significant impact on battery aging for the cell chemistry. As expected, the irreversible capacity loss as a result of the volumetric change during charging and discharging is significant to Si cells. The capacity shows a rapid fade in the early stage of full cycling (~4% fade per cycle up to 8 cycles) and stabilizes at a rate of ~0.67% fade per full cycle at 23 °C and ~0.82% fade per cycle at 45 °C, respectively.

Possible mechanisms behind the capacity fade in Si anode batteries have been reported in recent years, which appear to be twofold. First, the expansion and contraction of the Si can cause a pulverization of the anode particle morphology, which reduces electrical contact within the material as well as with the current collector. Second, the low potential of Si lithiation (<0.5 V vs Li^+/Li) causes the electrolytic decomposition at the anode-electrolyte interface, forming a layer of solid-electrolyte interphase (SEI) over the anode surface. Due to the electronically insulating of SEI, its formation during the first few cycles is normally self-inhibiting. In the case of Si anode, however, the continuous fracturing over cycling ruptures the SEI and exposes fresh surface area, resulting in thick, substantial SEI formation. This unrestrained growth not only hinders ionic transport and electronic conductivity, but also decreases the amount of cycleable Li-ions due to the consumption of Li. Thus the total capacity is being decreased.

In addition, the life cycle tests were run with the high voltage prototype cells. For this purpose cells with LNMO as cathode material and nano-sized Si as anode material are developed here. The charge terminal voltage of the cells is set to 4.85V. High cell voltages increase the energy density of the battery. It was observed that during the formation, the capacities of all cells slightly increased. After that, a rapid capacity fading as a function of cycle number is obtained. As mentioned, the volume change of Si during cycling may lead to rapid cell degradation. The reason for this capacity fading of LNMO is not completely clear yet. The usual assumptions include, among others, excessive surface passivation, which occurs especially at high voltages.

Cell Modelling

Both VOLVO and AIT developed a battery cell model in Matlab® Simulink® which is suitable for use in full vehicle simulation. The developed model in Matlab®/Simulink® is suited to reflect the characteristics of high energy cells. Due to a delay in cell manufacturing the work for this task was carried out along commercial high energy cells (Panasonic) for first modelling activities and planned to be used for comparison later on. Once the EuroLiion cells

(Si/LFP) were manufactured it was used for extracting necessary model parameters. During parameterisation, the obtained values were not stable even though the obtained unstable values were used. It needs to be mentioned however, that unstable values from prototype cells are very common.

In a little more detail, the full model including the part for the input signal with a simple RC parallel combination, where *current Profile* can be simulated. Here then, the current depends on time as imposed in the model. It further required *Rs(Soc, T), Rp1(Soc, T, i)* and *Cp1(Soc, T, i)* as the values to mimic the RC parallel combination which are thus dependent on the SOC, the temperature and the current of the cell.

The developed model in Matlab®/Simulink® was suited to reflect the characteristics of high energy cells. By introducing an object oriented C code to Simulink the simulation speed was high and the risk of the solver facing close loop problems was minimized. An interface still guarantees full flexibility of the model.

Tests for Cell Modelling

According to the initial plan, VOLVO performed extensive testing at cell level to extract necessary model parameters. The model was developed based on both high energy Panasonic and EuroLiion Si/LFP cells. Heavy duty Plug-in hybrid electric vehicle (PHEV) dynamic cycle was used to validate the model. **Error! Reference source not found.**simulation scheme of the PHEV cycle was used in that respect. The model then was created based on an equivalent electric circuit model, and worked under Matlab®/Simulink®.

The model can predict the cell behaviour quite well. The simulated voltage response has a similar ohmic and dynamic voltage response as the measured signal over time. The only difference that can be noted is a small offset in voltage profile between simulation and measurement. This offset of about 0.01V can be the result of deviation in cell parameters, small temperature difference, and measurement errors e.g. from current, voltage or SOC estimation.

For EuroLiion Si/LFP two RC circuits were used to develop the model. The first result from the simulation shows that the impedance of the cell is significantly underestimated in the model of the Si based cell. However, after careful investigation an adjustment of factor 4 on Equivalent Series Resistance (ESR) was performed. After adjustment in ESR value the simulation showed good dynamic response for Si/LFP cell.

Management developments for novel battery prototype

A comprehensive literature review was carried out to investigate algorithms for estimation of the internal battery states and performance. It concentrated on various methods for state prediction of batteries (SOX). While special focus was put on state of charge (SOC) prediction also state of health (SOH), voltage and power prediction and other strategies were investigated. Actually, it became clear that a reproducible method for evaluation of such methods was missing. This is why an approach for simulative validation of such algorithms was developed - a publication in an IEEE or related journal is under preparation.

With this information in mind, different SOC algorithms were selected for evaluation with the new EuroLiion test cells. The selection was done balancing needs for computational power, practicability and accuracy. The final strategies for evaluation then were:

- coloumb counting (easy parameterization, low accuracy, low computational power);
- enhanced coloumb counting (trade-off between accuracy, parameterization and computational power);
- extended Kalman Filter (high accuracy, complex parameterization and highest demands on computational power)

All methods were implemented in the developed Matlab®/Simulink® simulation environment. They were connected with the battery model developed in EuroLiion and parametrised with the cell data of the developed EuroLiion Si/LFP cell. This allows access to the internal states of the model in this case SOC. The measurements for the SOC estimators where distorted like it would be found in real world application. This allows for a direct comparison of the performance of each estimator in comparison to the real value.

It shows the response of the different estimators based on the distorted signals compared to the simulated SOC. While with constant charge and discharge pulses the coulomb counting drifts of because of not considering the coulombic efficiency of the cell and not resetting its states from time to time the enhanced coulomb counting is more accurate. After an initial learning phase the Extended Kalman Filter follows the real SOC closely. So this filter is also suited for the modern LNMO/Si technology developed in EuroLiion.

Safety Assessment & Testing

All the tests were performed according to the developed “Safety Test Procedure”. As additional cells were available for testing one further test was added. In the end, the tests conducted were:

- overcharge;
- short Circuit;
- thermal Stability;
- internal Short Circuit (additional).

Covering a broad spectrum of possible hazards to the cell as it is tested for electrical, thermal and mechanical abusive conditions. The entire test results, classification and interpretation were published via posters at various locations.

The results of the Si/LNMO cells gained through the internal short circuit test, showed that the voltage drops immediately, indicating a full short circuit. The temperature then in this case goes to 500°C and the cells starts to burn. As this is one of the most destructive tests available this is not a bad result for cells still in prototype stadium.

A classification according to EUCAR hazard levels – level 1-5, with 5 being the worst – of the responses of the EuroLiion LMNO/Si cells to the safety tests is gathered below. The external short circuit tests show level 2, the overcharge shows 2-3, thermal stability as well as the internal short circuit up to level 5.

However, in general it can be stated that the response of cell ranges from good to acceptable. For a prototype cell this is satisfying behaviour. The results might be positively compromised by the high internal resistance (lower short circuit currents), the high ratio of surface to volume (helps on heat dissipation) and the additional bag for gas (keeps cell pressure low). Homogeneous design, controlled production and fully balanced cell design in series production could positively affect the cell though.

The progress and materials have been presented at the EUCAR Conference (see Figure 6.4 below)

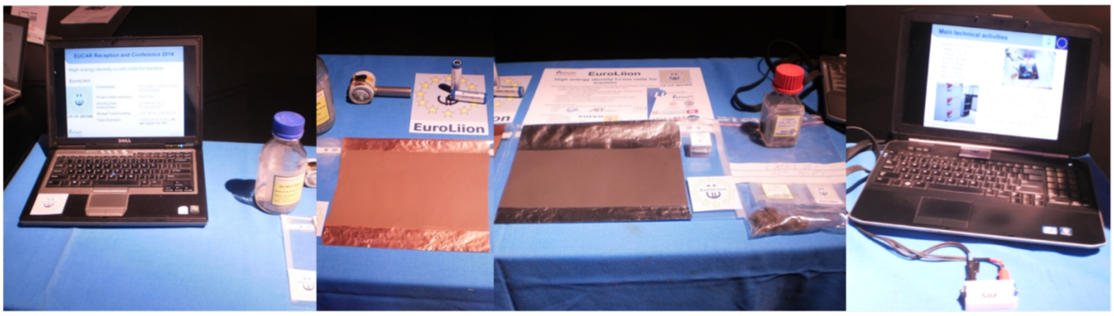

Fig. 6.4 Impression of the EUCAR Reception and Conference held in November 2014, where EuroLiion displayed their products.

This project took 4 years and the work of many people among European labs and companies. This was the timeline for the EuroLiion project (Figure 6.5)

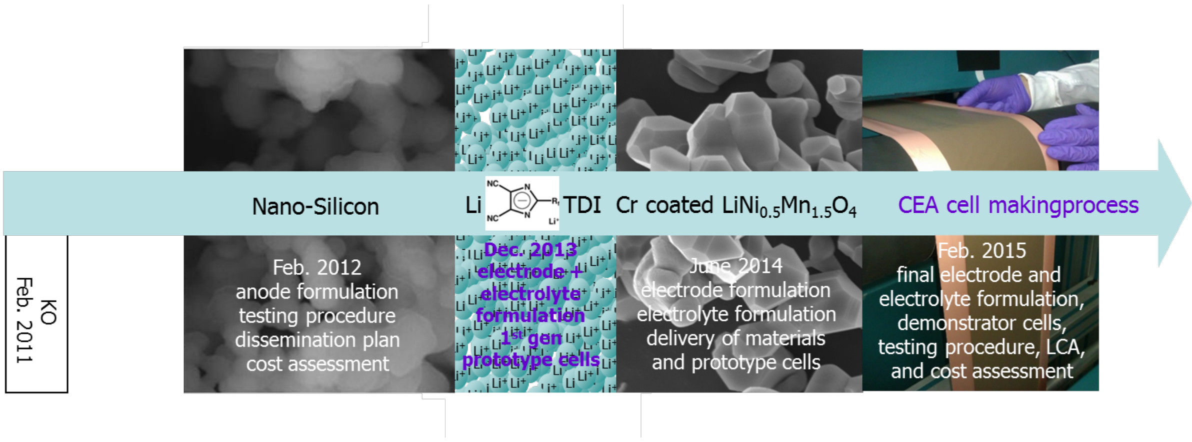

Fig. 6.5 Timeline and final product of the EuroLiion project.

Summary

Mankind has started taking the global warming problem into consideration, and has been doing so for decades. The relevance of the problem is slowly reaching everyone's mind, which has resulted in fast growth in important related research topics, among which energy materials.

One of the most important challenges has to do both with transportation and the production of polluting gases. In the last 3 decades, lithium ion batteries have grown to be a key technology, and are without doubt one of the most promising energy carriers for transportation and grid energy storage.

Despite the technology being well established, the performance of lithium ion batteries still could (and should) be improved on a number of points, such as energy density, lifespan, efficiency and safety. These are mainly materials challenges. This thesis looks at the positive electrode material as a way of obtaining a higher energy density in lithium ion batteries.

This thesis was written within the EuroLiion project, which has the goal to develop a new Li-ion cell for traction purposes, such as a car pulling up, with the following characteristics:

High energy density of at least 200 Wh/kg

Low cost, i.e. a maximum of 150 Euro/kWh

Chapter 1 provides a history of batteries, introduces some generalities and basic knowledge about batteries. In the end, it presents an overview of the EuroLiion project.

Chapter 2 gives an overview of the known technologies in terms of lithium nickel manganese oxide (LNMO), as well as an extensive list of the coatings and dopings that can be applied to this material in order to improve it. From this research and its results, in terms of particle size and its effect on performance, the effects of the different coatings, etc…, the positive electrode material for the whole project is chosen.

Chapter 3 describes the production of different variations of the material, and an evaluation of their behaviour. The results of an in-situ X-Ray absorption Spectroscopy study are presented. The effect of the oxidation state of the chromium doping on the LNMO, while the battery is cycled, is studied. SEM and EDX pictures of the material and its doping are also shown.

In chapter 4, in order to measure the enhancement due to the chromium doping, while having a topographic picture of the interface between the positive electrode and the electrolyte, an AFM analysis is presented. A new way is introduced to monitor 'in vivo' the ion and electronic transport between the positive electrode and the electrolyte.

Chapter 5 is a direct continuation of chapter 4. Indeed, due to lack of results to explain the enhancement of the material by the chromium doping, more structural measurements and surface characterizations, such as SEM, EDX, XAS, and XPS, are presented and explained.

The correlation between the lithium content and the nickel content at different states of charge is also explained.

Finally, at this stage of the project, the material has been improved and the reasons and scientific explanations of why this material is better are known. Development is now finalized and the material is in production by a Dutch company and sold to the contributors of the EuroLiion project for testing in prototypes. Chapter 6 explains the whereabouts of the whole project, including external work on the other parts of the project, such as electrolyte, anode, packaging and economic details.

In conclusion, during these 4 years of research, I synthetized, developed and tested a material that gathers all the desired performances. When my material has been chosen to be implemented and used by the EuroLiion partners, I also had a technical and scientific support for the industrial scale production of the material, which was well very rewarding and allowed me to gain some knowledge and be in close cooperation with the industry. To create a more powerful and efficient battery, the other elements need to be improved, in order for all parts of the cell to work in harmony and deliver the best performances possible.

Samenvatting

De mensheid begint het probleem van klimaatverandering in ogenschouw te nemen, en doet dit nu al decennia. De ernst van het probleem langzaamaan bij iedereen door begint te dringen, wat heeft geleid tot een snelle groei van onderzoek in belangrijke aan klimaatverandering gerelateerde onderwerpen, waaronder materialen voor energie.

Een van de belangrijkste uitdagingen heeft zowel met transport als de productie van verontreinigende gassen te maken. Gedurende de laatste 3 decennia zijn lithium-ion-batterijen uitgegroeid tot een belangrijke technologie, en zijn zonder twijfel een van de meest veelbelovende energiedragers voor transport en energieopslag.

Hoewel de technologie gevestigd is, kan (en moet) de prestatie van lithium-ion-batterijen nog verbeterd worden op een aantal punten, waaronder energiedichtheid, levensduur, efficiëntie en veiligheid. Dit zijn hoofdzakelijk materiaaluitdagingen. Dit proefschrift kijkt naar het materiaal voor de positieve elektrode om een hogere energiedichtheid in lithium-ion-batterijen te bewerkstelligen.

Dit proefschrift is geschreven binnen het EuroLiion project, welk tot doel heeft voor tractiedoeleinden, bijvoorbeeld een auto die optrekt, een nieuwe Li-ion cel te ontwikkelen met de volgende kenmerken:

Hoge energiedichtheid van ten minste 200 Wh/kg

Lage kosten, d.w.z. maximaal 150 Euro/kWh

Hoofdstuk 1 geeft een geschiedenis van batterijen weer, en introduceert wat algemeenheden en basiskennis rondom batterijen. Tenslotte presenteert het een overzicht van het EuroLiion project.

Hoofdstuk 2 geeft een overzicht van de bekende technologieën in context van lithium-nikkel-mangaan-oxide (LNMO), evenals een uitgebreide lijst van de deklagen en doteringen die op dit materiaal kunnen worden toegepast om het te verbeteren. Uit dit onderzoek, en resultaten in de zin van deeltjesgrootte en het effect daarvan op prestatie, het effect van de verschillende deklagen, enz., is er een materiaal voor de positieve elektrode gekozen voor het hele project.

Hoofdstuk 3 beschrijft de productie van verschillende variaties op het materiaal, en een evaluatie van hun gedrag. De resultaten van een in-situ röntgenabsorptie spectroscopie onderzoek (X-ray Absorption Spectroscopy) worden gepresenteerd. Het effect van het oxidatiegetal van de chroomdotering op het LNMO, tijdens het herhaald op- en ontladen van de batterij, is bestudeerd. SEM en EDX plaatjes van het materiaal en haar doteringen worden ook getoond.

In hoofdstuk 4 toont, om de verbetering als gevolg van chroomdotering te meten, samen met een topografisch beeld van het grensvlak tussen de positieve electrode en het elektrolyt, een AFM analyse. Tevens wordt een nieuwe wijze geintroduceerd om ‘in vivo’ het ionen- en elektronentransport tussen positieve electrode en elektrolyt te volgen.

Hoofdstuk 5 is een direct vervolg op hoofdstuk 4. Inderdaad, vanwege het gebrek aan resultaten die de verbetering van het materiaal als gevolg van chroomdotering kunnen verklaren, worden meer structurele metingen en oppervlaktekarakteriseringen, zoals SEM, EDX, XAS en XPS gepresenteerd en verklaard. De correlatie tussen het lithiumgehalte en het nickelgehalte in verschillende stadia van (ont)lading wordt ook verklaard.

Ten slotte is, in dit stadium van het project, het materiaal verbeterd en zijn de redenen en wetenschappelijke verklaringen waarom dit materiaal beter is bekend. Ontwikkeling is afgerond, en het materiaal is door een Nederlands bedrijf in productie genomen, en wordt verkocht aan de deelnemers aan het EuroLiionproject voor testen in prototypes. Hoofdstuk 6 licht de toestand van het project toe, inclusief extern werk aan de andere delen van het project, zoals het elektrolyt, de anode, verpakking, en economische bijzonderheden.

In conclusie is er een materiaal voor de positieve elektrode van lithiumionbatterijen gemaakt, dat alle gewenste eigenschappen en prestaties combineert, en voldoet aan de door autofabrikanten gestelde vereisten. Het materiaal voor de positieve elektrode is echter slechts een deel van de puzzel. Om een krachtiger en meer efficiente batterij te maken moeten de andere elementen verbeterd worden, opdat alle delen van de cel in harmonie werken en de best mogelijke prestaties leveren. Voor meer hierover verwijs ik de lezer door naar de andere proefschriften binnen het EuroLiion project.

Acknowledgements

The time has come…

After a master thesis and those 4 years of PhD, it is finally over.

Nothing would have been possible without all of you.

First of all Erik, I can't even describe how grateful I am to have had such a supervisor, both from a scientific and human point of view. You were always here to advise me and answer any question I had. You worked hard to transform me into a scientist and I know it has been hard….

Ekkes, it was also a privilege to have you as my promoter. You were also here when I needed advice and guidance.

Frans, the saviour ! I don't think this thesis would be ever finished without all the work you have done in the last year of my PhD. I can't even start to tell you how grateful I am. Thank you for everything, including the nice (not so) scientific talks.

Now the dream team of 1.013… Corrado, your love for Gerard Depardieu almost made me write this in French but I decided to keep it in English, otherwise you're going to start cursing and scare the people around you when you read that !

Thank you for the amazing time when I arrived in the office, and for all the good mood and nice time we still continue to have. I know you are mad because France has it all : best wine, best food, best landscapes and also the Mont-Blanc, but relax, you are welcome to visit my country whenever you want ! I'm probably going to get killed by someone, for this sentence… ! Thanks for accepting to be my paranimph !

Jan, my old (in age) Dutch friend ! Thank you for sharing the nice moments in the office and also to try to explain me how your wonderful laser setup works. I'm not sure you succeeded but hey ! you tried ! Nothing bad happened to it anyway. Oh wait… Thanks for being my paranimph.

David, thanks for bringing your good mood every day, even after the accident, you were always optimistic. Now it's just a bad memory. Enjoy on your heavenly island !

Mario ! I think I've never met anyone talking so much and that's something ! Thank you for the endless and numerous talks about life but also sometimes science. I realized during our last meeting in Sweden that the Dala horse would always be with us . All Hail the Dala Horse, whatever his colour is !

Julien, thanks for having shared with me the role of the poor French students in our office. We remained strong and stood up against all those Italians. What a bright victory ! I wish you all the best together with Sasha !

Esteban, when I arrived, I thought I was the most intolerant person on this planet. Thank you for proving me wrong !! Hahaha. Seriously thank you for being such a nice guy and teaching me about your beautiful colombian country with so much passion. You know I loved it there and I will come back one day soon, so prepare the Guaro ! (and your beautiful blue shorts)

Miguel, thanks for all the nice open talks in but also out of the office, mainly about food or to try to get Sheila to prepare the coffee ! Now that you found a job in Netherlands, I know we will keep in touch !

Sheila, even if you never prepared coffee, I enjoyed very much this time with you. Your « optimism » has always impressed me and we had lots of fun complaining about…well…everything. I hope you will get the position of your dreams after the EMBA.

Pierre, you just arrived but it has been nice to know you. Sorry for talking all the time with Miguel and Sheila and I wish you all the best for your PhD.

Thank you also to all people in the staff, especially Ben, Marcel and Duco. Thanks for helping me with the experiments and for always answering my questions.

Kostis, you were not part of the office but I consider you as part of the dream team anyway. Thanks for all the wonderful moments and dinners full of greek food. All the best for the end of your PhD and I hope you will stick around !

I would also like to thank all the friends and wonderful people I met here in Netherlands but also abroad, some of you were working with me : Tobias, Anne, Marco, it was really nice to share some time with you. All the best for your company, post-doc and PhD, respectively.

Some of you were part of my life in Delft and we became friends. International friends : Carolina, Naty, Manu, Zenaide, Julian, Lucho, Juan Camilo, Damian : thanks for the good times, concerts, dinners, drinks, parties. It was truly awesome !

Stefi, thanks for being such a nice and kind person and sharing the apartment during the time I hosted you. You taught me to work more and I taught you to work less ! I think that was a good deal ! Good luck in Italy with your new job.

Maaike, Jolien, Danielle, Carlijn, thanks for being such nice flatmates during my 2 first years in Delft. You helped me getting better in dutch and taught me a lot of dutch culture. Dank jullie wel en ik wens jullie het best voor de toekomst !

Tot snel !

Alex et Jordi : les deux raclures. Merci pour toutes ces conversations hautes en couleur, nos débats éclairés sur l'ethnologie et l'anthropologie. Nos prises de conscience sur ce monde qui va mal, nos soirées chocs ainsi que nos soirées chique, cass et QPUC, depuis toutes ces années. Quand je pense qu'on a tous les 3 fini docteurs, je me dis que ce monde va vraiment de mal en pis. Ça me fout le seum et du coup, en fait, ça me mets les nerfs en biseau alors je vous laisse, je vais couper des bûchettes ! Bouboule vous salue, il a du pain sur la planche dans ma rue… Oloyonisse.

Bouboule, toi qui m'accompagne depuis ces années sur les routes européennes, c'est aussi un peu grâce à toi si j'ai pu terminer ma thèse. De par ton caractère bien trempé, hérité des fjords et des lacs ancestraux, tu as su me guider sur la voie de la science et me débarrasser des (nombreux) obstacles qui se dressaient (ou non) sur mon chemin. Tu m'as couté une blinde en viande rouge, mais ça en valait la peine. J'espère que tu continueras d'aider les plus démunis comme tu as l'habitude de le faire depuis tout ce temps… GRAOR

Tout ce labeur harassant n'aurait jamais pu être terminé sans l'aide de l'entreprise Makla Bouhlel "Bentchicou" qui a su mettre au point cette onctueuse pate au parfum subtil qui procure à son porteur force et détermination. Merci, vous êtes « chique » .

Steph (bon courage pour le petit coin… , je suis persuadé que ça va envoyer du très lourd), Alicia (j'espère que d'ici au jour de ma soutenance, tu auras trouvé un nouveau taff petit chinoise !), merci de m'avoir procuré la french-mood pendant ces années, il semblerait que je sois le seul à avoir supporté le plat pays. Tant pis, vous êtes les bienvenues ici pour une soirée Kaamelott-fromages et saucisson. Et un jour prochain qui sait, je rentrerai au bercail…

A bientôt les meufs !

Finally, last but not least, my family :

Papa et Maman : merci de m'avoir soutenu pendant toutes ces années d'études et de vagabondages. J'ai découvert de nombreux monts et de nombreux vaux, grâce à vous et je vous dois une fière chandelle (du pied). Je ne serais jamais arrivé jusque là sans vous.

Emilie, Cyril, Sébastien, Virginie, Illa, Mathis, Victor, Hortense et Paul. Désolé de ne pas avoir été plus présent mais c'était pour la bonne cause. Merci de m'avoir soutenu depuis que je suis parti de notre belle région cisséenne. À bientôt pour une partie de Fais pas l'con ou du gros lutin ! Mes amitiés à Josiane, la pauvre…

Alessia, proviamo le mie capacità con l'italiano! Grazie per essere parte della mia vita, ormai già da un po' di tempo, e spero per molto di più! É semplicemente stupendo. Mi hai dimostrato cosa significano lavoro e perseveranza e sei motivo di ispirazione (anche se tu non lo sai). Non cambiare nulla, come già ti ho detto, sei davvero una persona straordinaria.

Ti amo profondamente. Ditto...

Voilà, this is over ! Thank you all once again. It has been a pleasure, although I'm glad the PhD writing is over. A new episode begins…

> « *After that, my guess is that you will never hear from him again. The greatest trick the devil ever pulled was convincing the world he did not exist. And like that... he is gone* »